2017

Development of Novel Catalysts for Air Pollution Control

Chao Wang
University of South Carolina

DEVELOPMENT OF NOVEL CATALYSTS FOR AIR POLLUTION CONTROL

by

Chao Wang

Bachelor of Science
Fudan University, 2012

Submitted in Partial Fulfillment of the Requirements

For the Degree of Doctor of Philosophy in

Chemical Engineering

College of Engineering and Computing

University of South Carolina

2017

Accepted by:

Jochen Lauterbach, Major Professor

Christopher T. Williams, Committee Member

Bihter Padak, Committee Member

Thomas Vogt, Committee Member

John W. Weidner, Committee Member

Cheryl L. Addy, Vice Provost and Dean of the Graduate School

Dedication

I would like to dedicate this work to my parents Youliang Wang and Fang Li, for their enlightened education and guidance in my life.

Acknowledgements

First, I would like to thank my advisor Professor Jochen Lauterbach for his solid support and constructive training in my PhD study. Jochen provided very free research space for me to do whatever I wanted to, which cultivated my independent research skills a lot. My critical thinking was greatly improved by his training as well. In addition, I would like to thank Jochen for providing me so many valuable opportunities to develop my research, which include attending multiple national and international conferences, collaborating with national labs, scholarship/grant recommendations and application of industry trainings. In all, I appreciate his guide in my PhD research and he changed the way I look at science.

Second, I would like to acknowledge Research Assistant Professor Erdem Sasmaz and Cun Wen for their valuable advice on my research. Discussions with them helped me built up a more careful and responsible attitude on science.

I would like to thank Dr. Oleg Alexeevfor his assistance and teaching for XAS experiment and data analysis. I also thank Dr. Andrew Binder, Dr. Todd Toops, and Dr. Michael J. Lance from Oak Ridge National Lab for their help on reaction tests and catalysts characterization. I would like to acknowledge my PhD committee Dr. Christopher T. Williams, Dr. Bihter Padak and Dr. Thomas Vogt, for providing me constructive suggestion.

At last, thanks to my dear lab mates and friends at Columbia, Aixa Del Valle, Zhiyong Wang, Emily Freeman, Katie McCullough, Sungtak Kim, Shahriar Salim, Kai Mayeda, Kate Mingle, Calvin Tomas, Elisabeth Barrow, Juan Jimenez, Shuguo Ma, Yunya Zhang, Weijian Diao, Yue Dai, Donald Allen Caughman, Yating Mao, Qiuli Liu, Xin Li, Xiaoming Chen, Ye Lin, Libin Lei, Fahad Almalki, you all made my journey in U.S. wonderful and unforgettable.

Abstract

The development of economy strongly related with increased consumption of fossil fuels, which causes severe air pollution issue. With more and more strict environmental regulations implemented all over the world, robust and efficient emission control technologies need to be innovated and applied to overcome the pollution challenge. This dissertation focuses on utilizing heterogeneous catalysis to eliminate carbon monoxide (CO), hydrocarbons (CH_x) and nitric oxides (NO_x) emissions produced from fossil fuel combustion.

The first type of catalyst is Pd supported on Mn-Ce solid solution. It achieves 100% CO conversion at room temperature. The high activity is attributed to superior lattice oxygen transfer interaction between Pd and support, which is discovered by multiple in situ and ex situ characterizations. When tested under practical simulated diesel exhaust condition, including extra water, CH_x and NO_x, the CO light-off temperature increased to 170^{o}C due to competitive adsorption of CH_x and NO_x. The comparison of structure characterization before and after hydrothermal aging shows that the Pd is attempting to aggregate and solid solution support is tending to segregate. However, such minor change is not significant enough to change catalysts activity. Doping additional Sn into MC support can improve sulfur resistance of catalysts for low temperature CO oxidation.

The second type of catalyst is Pd supported on shape and surface facet controlled Fe and Mn-Fe nanorods. Mn can be successfully doped into Fe nanorod and form solid solution. The Pd/Mn-Fe catalyst shows over 90% CO conversion at 50^{o}C which is much higher than the inactive Pd/Fe catalyst. The Pd structure and reactivity change on doped oxide surface with controlled facet will be elucidated. The goal of this study is to provide new fundamental insight on metal-support interaction and active sites design approach.

The third type is SSZ-13 zeolite based catalyst, which has small pore structure and excellent hydrothermal stability. By ion exchange method, metal cations can be introduced into the zeolite pores and function as active sites. The active sites can be used in the ammonia selective catalytic reduction (NH_3-SCR) of NO_x, which is a major NO_x reduction technology in heavy duty trucks and coal power plants. Cu-SSZ-13 zeolite catalysts show the best NO conversion (over 95%) from 150-450^{o}C when compared with Fe and Ce based SSZ-13. Moreover, in the presence of SO_2 and H_2O, which usually can poison SCR catalysts, Cu-SSZ-13 still keeps a relatively high sulfur resistance at temperatures between 250-450^{o}C.

Table of Contents

List of Figures

Chapter 1

Introduction

1.1 Environmental catalysis

Environmental catalysis refers to catalytic technologies for reducing emissions of environmentally unacceptable compounds [1]. It includes a broad range of catalytic technologies. The first typical type of technology is directly converting pollutions to harmless product. This category includes mobile emission control, NO_x reduction from stationary sources (e.g. power plants), sulfur compounds and VOC (volatile organic compound) conversion, conversion of ozone, formaldehyde and other organic indoor pollutants, photocatalytic antibacterial air purification, liquid and solid waste treatment (polymers and other solid waste), and greenhouse gas abatement or conversion. The second type of environmental catalysis is improving chemical reaction process and reduces the production of pollution from the process. This category contains the application of catalysis for eco-compatible refinery, chemical catalytic processes, and new catalytic routes to valuable products without forming undesirable pollutants. Energy-efficient catalytic technologies are the third type. It includes catalytic combustion, catalysis in fuel cells, catalytic devices for using renewable energy sources like solar energy or biomass. Finally, the reduction of the environmental impact in the use or disposal of catalysts should also be cited as part of the objectives of environmental catalysis.

Among various environmental catalysis applications, this dissertation focuses on researching two specific directions for air pollution control. The investigation of new catalysts for low temperature diesel engine exhaust control was first explored. Next screening for sulfur resistant catalysts for NOx reduction in coal power plants was investigated.

1.2 Diesel engine exhaust emission control

The emissions from a diesel engine are composed of solids, liquids and gases. The combined solids and liquids are called total particulate matter (PM) and are composed of soot, sulfates and soluble organic fractions (SOFs). Gaseous hydrocarbons (HC), carbon monoxide, nitrogen oxides, and sulfur dioxide make up the gas phase emissions. Several strategies have been developed in order to reduce the quantity of pollutants emitted to the atmosphere. The diesel oxidation catalysts (DOC) are used to oxidize CO and HC to CO_2 and water before release to the atmosphere. Another potential role of the DOC is to oxidize NO to NO_2 for the passive regeneration of the diesel particulate filter (DPF). This is located downstream of the DOC in the engine exhaust. DOC can also be used to enhance NO_x reduction in the selective catalytic reduction (SCR) process. The limiting factor for the DOC efficiency is its light off temperature (the temperature below which oxidation is kinetically limited), which can reduce its efficiency, especially during urban operating conditions [2]. Up to 80% of CO and hydrocarbon emission can emit during the automobile cold start phase [3-5].

Many categories of catalysts were developed for low temperature oxidation of CO. Cobalt oxide (Co_3O_4) shows very high CO oxidation activity at and below ambient temperatures [6]. Different CO oxidation light-off temperatures (T_{50}) for Co_3O_4 have

been reported. Cunningham et al. [7] found a T_{50} of −54◦C for pure Co_3O_4 and Thormahlen et al. [8] reported a T_{50} of −63◦C for Co_3O_4 supported on Al_2O_3. It was only the pre-oxidized cobalt oxide catalyst that showed activity at these low temperatures. Upon adding Pt or Pd to a Co_3O_4/Al_2O_3 catalyst, Meng et al. [9] found that the temperature required for full conversion in CO oxidation could be decreased by -213^{o}C.

However, in the complex diesel exhaust gas conditions, the low-temperature activity of Co_3O_4 is inhibited by the presence of water [7, 10], hydrocarbons, and NO [10]. Moreover, even without these inhibitors, a slow decrease in activity was observed during steady-state CO oxidation at low temperature due to accumulation of carbonates on the catalyst surface [7]. Like Co_3O_4 catalysts, the discovery of gold catalyst for low temperature CO oxidation [11] made by Haruta and colleagues motivated a considerable amount of research on the activity of gold-based catalysts. Gold catalysts supported on transition metal oxides exhibited high CO oxidation activities at very low temperatures below the freezing point (0 ° C) when the gold particles are smaller than about 10 nm [12, 13]. Specifically, small gold particles (2-4 nm in diameter) have an activity at 273 K that is more than 2 orders of magnitude larger than larger gold particles (20-40 nm in diameter) regardless of the support being reducible or irreducible oxide [14]. Even though gold catalysts preform good CO oxidation activity at low temperature its applications are limited. This is due to catalyst deactivation and low stability under reaction conditions which is caused by accumulation of carbonates on the surface and the agglomeration of Au particles [15,16].

In practical automobile CO and hydrocarbon oxidation, the current DOC typically consists of platinum group metals (PGMs) (Pt, Pd, Rh) as an active phase that are placed

on high surface area supports and oxygen storage materials [17-19]. Among them, Pd catalysts drew much attention due to the low cost, fast light-off performance, high oxidation capability, and sintering resistance compared to Pt and Rh catalysts [20-24]. Despite the high performance of Pd catalysts, Pd has poor CO oxidation activity at low exhaust temperatures and deactivates by the presence of sulfur compounds in the exhaust gas [25-26]. For instance, Pd based DOCs can emit up to 80% of CO at temperatures below 200^{o}C during the cold-start stage of a vehicle [20,27-28]. For diesel and efficient lean-burn internal combustion engines, the average exhaust temperature is low, which ultimately affects the CO oxidation performance of the catalyst [17, 29-30]. The low CO oxidation activity of DOCs at low exhaust temperatures is typically explained with the blocking of active sites by HCs [30-31]. Thus, novel catalysts that can maintain a high oxidation performance at low exhaust temperatures while resisting inhibition by HCs are desired.

CeO_2 is a widely used component in DOCs due to the Ce^{3+}/Ce^{4+} redox cycle. CeO_2 can store and release oxygen, depending on the exhaust gas composition. This ability is known as oxygen storage capacity (OSC), and improves oxidation of CO and HCs during lean and rich cycles [32]. Ceria promoted Pd catalysts exhibit high catalytic activity for CO oxidation at low-temperatures (100^{o}C-200^{o}C) due to the OSC and strong-metal support interaction (SMSI) [33-35]. In addition, CeO_2 promotes noble metal dispersion [36] and increases the activity for water-gas shift and steam reforming reactions [37-38]. Despite the high performance of CeO_2, it has low thermal stability and tends to deactivate at temperatures above 800^{o}C [39]. The incorporation of a secondary metal into the ceria lattice can improve the OSC and prevent its sintering [39-41].

The development of automobile catalysts meanwhile facilitates the fundamental reaction mechanism study. For CO oxidation, the most cited mechanism over metal or supported metal are the Eley-Rideal(E-R), Langmuir-Hinshelwood(L-H), and Mars-van Krevelen(MvK) mechanisms. The E-R mechanism is based on two reaction steps in which one reactant (e.g. O_2) is first adsorbed to the surface and the second reactant directly reacts with it in the gas phase without an adsorption step. For example, Manuel et al. proposed an E-R reaction mechanism in which CO(g) would react on a Rh^{x+} site surrounded by two O vacancies partially filled with oxygen species[42]. On the other hand, the L-H mechanism includes the adsorption of both CO and O_2 on the catalyst surface. For example, it is widely accepted that the reaction of CO oxidation over unsupported Pt proceeds according to an L-H mechanism, in which the determining steps occur in the adsorbed phase. CO is not dissociated whereas O_2 is generally dissociated above 170 K[42]. The adsorbed CO then reacts with O to produce CO_2. Such mechanism is also suitable to be employed in alumina- or silica-supported catalysts, which are considered as inert supports. It is important to note that in L-H mechanism, CO with -1 kinetic order has a strong inhibiting effect on metal sites, whereas the reaction is first order with respect to oxygen on all the studied metals[42].

In MvK mechanism, CO reacts with lattice oxygen directly at the surface of metal oxide catalysts leaving an oxygen vacancy. The vacancy then can be replenished by gas phase oxygen or by mobile bulk oxygen. For instance, ceria allows the metals to work in transient conditions when the oxygen pressure in gas phase decreases much below the stoichiometry[43, 44]. Yu Yao investigated the impact of ceria on the kinetics of CO oxidation reaction [45]. Contrary to alumina-supported catalysts, the kinetic order with

respect to oxygen decreases and is close to zero when ceria is added to the support. Still more remarkable, the kinetic orders with respect to CO become positive, whereas they were negative over metal/Al_2O_3 catalysts. This finding was interpreted as the result of a cooperative effect between metals and ceria (dual-site mechanism). Carbon monoxide would be adsorbed on metal sites whereas oxygen could be adsorbed and activated on ceria sites in close vicinity of metal particles. The kinetic orders with respect to CO and O_2 are both between 0 and 1.

1.3 NO_x emission control from stationary source

The major source of nitric oxides (NO_x) emission is combustion of fuels in engines and power plants. NO_x emission and SO_x emissions are components of acid rain. Furthermore, NO_x and hydrocarbons can react in atmosphere and form photochemical ozone (smog). NO_x is formed in the combustion process by combination of the N_2 and O_2 in the air.

NH_3-SCR reaction is a widely used technology for the reduction of NO_x emissions in stationary sources (e.g. gas-, oil-, and coal-power plants) and mobile sources (e.g., diesel engines). It was discovered that NH_3 can react selectively with NO_x, producing N_2 and H_2O. When sulfur is present in the flue gas, the oxidation from SO_2 to SO_3 results in formation of H_2SO_4 on reaction with H_2O, which can cause corrosion of equipment. The reaction of NH_3 and SO_3 results in formation of $(NH_4)_2SO_3$ and NH_4HSO_4, which can deposits on SCR catalysts and cause the deactivation of catalysts.

Nowadays, the commercial catalysts used for SCR units in industry are mainly TiO_2-supported V_2O_5, promoted with WO_3, with operation temperature window at 350–450◦C [46-51]. This type of catalyst has also been used for HD diesel vehicles in Europe

as well. However, with higher reaction temperature 550^{o}C, the catalyst loses selectivity leading to NH_3 oxidation. In addition, the active anatase structure of TiO_2 with a surface area of 80-120 m^2/g irreversibly converts to rutile with a surface area of less than 10 m^2/g, which can deactivate the catalyst. Addition of WO_3 and MoO_3 can improve the redox properties and activity. Although vanadium catalysts have been introduced into the market for power plants and diesel vehicles, some problems still need to be solved, such as rapid catalyst activity decrease above 550 ◦C due to the high activity for oxidation of SO_2 to SO_3, and the toxicity of the vanadium species to the environment [51–53].

Many studies have shown that zeolites are promising catalysts for coal combustion flue gas conditions due to their wide working temperature from 200^{o}C to 600^{o}C[54-60]. Zeolites comprises of tetrahedra units (TO_4) through corner sharing to form a three dimensional microporous framework. Framework TO_4 generally refers to $[SiO_4]^{4-}$ and $[AlO_4]^{5-}$. Isomorphous substitution of Si^{4+} with Al^{3+} renders the zeolite framework negatively charged. This charge is neutralized by exchangeable cations, such as Cu^{2+}, Na^{+}, and K^{+} located in the channels or cages of the structure. Cations will try to maximize their coordination number through interacting with O ions from the zeolite. The O ions around the tetrahedral Al^{3+} are preferential anchor sites for Cu^{2+} cations due to the electron neutralization [51, 54]. Compare to V-Ti based catalysts, commercially available zeolites can keep good activity at 600^{o}C without oxidizing NH_3 to NO_x. While in a high water concentration stream from coal power plant or automobile sources, zeolite tend to deactivate by a process called dealumination, where Al^{3+} in the zeolite framework migrates out of the structure. This leads to irreversible change and, in the extreme case, collapse of crystalline structure.

Aqueous ion exchange is the most commonly used method for preparing zeolites with transition metal ions located at exchange sites. For instance, Cu ion-exchanged zeolite contains aqueous Cu in the pores and cavities of the zeolite. Upon high-temperature treatment, water is removed and the Cu cations coordinate to the surface oxygen of the exchange sites. Cu active sites formation depends on the Si to Al ratio and Cu loading in the zeolite framework [51]. For example, in Cu-SSZ-13 with Chabazite structure, isolated Cu^{2+} in coordinated in a 6-member ring is generally considered as active site for selective catalytic reduction of NO by NH_3 (NH_3-SCR). Complexes of Cu^{2+} can also be ion-exchanged in the cages and channels of zeolites and can also be synthesized in situ by ligand adsorption. The coordination chemistry of Cu^{2+} with extra-framework ligands is different from the coordination chemistry in aqueous solution. This is due to the geometric constraints in the cages. Even if the complex is similar with regard to its ligands, encapsulation in zeolite cages and pores may also impose additional constraints in the complex, inducing significant changes in bond lengths and angles. Such variations could substantially influence their reactivity in activating molecules [54].

Different ion exchanged zeolites were reported to be active for NH_3-SCR reaction, such as Fe [54,55], Cu[56,57], Mn [58], and Ce [59,60]. Among such a wide family of catalysts, iron and copper zeolites are particularly active in NH_3-SCR and have been extensively studied. Yang et al reported a Fe-ZSM-5 catalysts, with surprisingly high NO conversions in a broad temperature window (375-600 ℃) under a high gas hourly space velocity (GHSV) of 4.6×10^5 1/h. However, at high temperatures, in the presence of water vapor (steam), the catalyst deactivates and exhibits greatly diminished SCR activity. This is due to dealumination of the zeolite framework. At elevated

temperatures, the aluminum in the framework becomes unstable and detaches from the tetrahedral framework positions [61–66]. Previous work from our group indicates that Cu-SSZ-13 zeolite catalyst exhibits higher hydrothermal stability and NO_x conversion than other Cu loaded zeolite catalysts, such as ZSM-5, in an ideal flue gas condition (NO, NH_3, O_2 and N_2) [67]. Moreover, Cu-SSZ-13 has found as a NH_3-SCR game changing catalyst due to its high catalytic activity, N_2 selectivity compared to other ion-exchanged SSZ-13 catalyst [68, 69]. Active sites and reaction mechanisms on Cu-SSZ-13 have been reported in many recent papers [70-73].

Co-cations, i.e. alkali, alkaline-earth elements and rare earth metal, can direct the Cu species and change the location of Cu species, which can further change the Cu site structure and activity. The coordination chemistry of Cu^{2+} in zeolites is well established [74]. Cu^{2+} preferentially coordinates in 6 membered rings with 1, 2 or 3 Al tetrahedra. It coordinates preferentially with the oxygen atoms of the Al-tetrahedra, which are more basic than those of the Si-tetrahedra. Some research has been performed with Ni on FAU zeolite, where the Na^+ co-cations are competing and hindering the migration of the metal to the 6-MR channels from the super cages during thermal treatment [75]. In Cu-SSZ-13 zeolite, on the other hand, a recent study shows that Na^+ cannot change the location of Cu^{2+} in 6-MR, but only weaken the interaction between Cu and SSZ-13 framework, while other larger alkali metals, such as K^+ and Cs^+, can limit the number of Cu^{2+} ions able to reside at such sites [76].

Chapter 2

Experimental and Techniques

2.1 Catalyst preparation

2.1.1Precipitation

Precipitation method is one of the most widely used catalyst preparation methods in industry. A common procedure for precipitation method is mixing an aqueous metal salt solution with an aqueous alkali or ammonium carbonate. This results in the precipitation of an insoluble metal hydroxide or metal carbonate, which is followed by filtration, washing, drying and calcination. In the calcination step at high temperature, these insoluble sediments can be converted to metal oxides. The metal precursors and precipitant are generally chosen because of their high water solubility and easy removal of unwanted elements at high temperature (e.g. NO_3^-, Cl^-).

The final particle size and shape of catalysts can be controlled by a variety of factors, such as solution pH, metal precursor/precipitant type, temperature and stirring rate, surfactant e.g. PVP. Some advantages of the precipitation methods make it the most widely and simply used methods. First, it generally provides a relatively uniform particle size and shape distribution. In addition, pore size and distribution of catalysts can be well controlled.

If two or more metal compounds are present, they may precipitate at different rates or in sequence, which will cause final phase separation of the catalysts. However, if two metal or more metal compounds can precipitate simultaneously and could finally form uniform crystal structure, such solid might have special chemical properties in catalytic reactions due to its unique structure and components. The solid is unusually called solid solution. More detailed synthesis steps are explained in the experimental section of chapter 3 and 4.

2.1.2 Wet impregnation method

A carrier or support is contacted with aqueous solution of one or more metal precursors. The water present from solution must be removed from the support through drying in order to release the metal precursor. When most of the moisture is removed by evaporation of liquid water, the result is that a substantial fraction of dissolved precursor is deposited on the surface or/and pores of the support. The mixture is then dried and calcined at high temperature to crystalize or stabilize the catalyst and removal unwanted elements. In this step, the metal precursor decomposed to metal oxide and gas. For example, $Pd(NO_3)_2$ precursor can decompose to PdO and NO_2 at 550^oC.

This method is preferred in preparing supported noble metal catalysts. Because it can spread out the metal in a finely divided a form without washing and filtering compared to precipitation method that may cause the loss of precious metal. The noble metal is unusually used 1wt% or less. This could greatly reduce the consumption of expensive ingredient meanwhile maintain the active components on the surface or in the pores of support. More detailed synthesis steps are explained in the experimental section of chapter 3 and 5.

2.1.3 Zeolite synthesis

A general route for zeolite synthesis is the hydrothermal synthesis method that converts a mixture of silicon and aluminum compounds, alkali metal cation (optional), organic molecules and water through supersaturated solution into a microporous crystalline aluminosilicate. Colloidal silica, waterglass, pyrogenic silica or silicon alkoxides are common sources of silicon. Gibbsite, pseudo-boehmite, aluminate salts, aluminum alkoxides are unusually used as aluminum source. Cationic and neutral organic molecules are added as structure-directing agents or so called templates to construct Si/Al framework.

The presence of OH ions solubilizes the gel and de-polimerizes the precursors into silica and alumina, directing them around the cation of the structure-directing agent (organic template). This step is known as primary nucleation and is driven by micro-processes such as the pH of the solution and macro-processes such as stirring of the gel. After the primary nucleation, the primary structural units form polyhedra and join to form the zeolite crystal, produced mostly by the driving force caused by the stirring of the solution. This process is known as secondary nucleation. Once the polyhedral is formed, it is combined with other polyhedral and multiplied; performing the crystallization process. For this process, higher temperatures are required to promote the formation of larger crystals.

By definition, the primary nucleation is governed by the driving force caused by the super saturation of the solution. In other words, if the solution is too diluted in water, no driving force exists to incorporate atoms into the zeolite framework. The primary nucleation can be both a homogeneous and heterogeneous process. It is a homogeneous

process when the nucleation is driven by the solution components itself (e.g. silicon and aluminum precursors, organic template). On the other hand, it is a heterogeneous process when it is driven by a material that will not become part of the framework. An example for this process is the use of mineralizers such as fluorine sources or the addition of seeds. The crystallization step is carried out in a Teflon-lined autoclave reactor under autogenous pressures and temperatures above 140˚C. The antogenous pressure is produced by the vapor generated by the gel inside the Teflon autoclave when it is heated. Various parameters can affect the formation and growth of zeolites, such as molar composition, pH, temperature and time, precursor specious and templates. More detailed synthesis steps are explained in the experimental section of chapter 6.

2.2 Characterization

2.2.1 X-ray powder diffraction (XRD)

X-ray powder diffraction (XRD) is a quick analytical technique primarily used for phase identification of a crystalline material and can give information on unit cell dimensions. X-ray diffraction is a bulk technique. XRD is based on constructive interference of monochromatic X-rays and a crystalline sample. The X-ray is generated by a cathode ray tube. The interaction of the incident rays with the sample produces constructive interference when conditions fulfill Bragg's Law ($n\lambda=2d\sin\theta$). This law connects the wavelength of electromagnetic radiation to the diffraction angle and the lattice spacing in a crystalline sample. Because of the random orientation of the powdered material all possible diffraction directions of the lattice can be obtained. Conversion of the diffraction peaks to d-spacings results in identification of the mineral because each

mineral has a set of unique d-spacings, which can be by compared with standard reference patterns.

The mean crystallite size of a catalyst can be determined from the broadening of a diffraction peak, measured at one-half the height, which is called full half maximum width. The line broadening is inversely proportional to the crystallite size and can be used to provide an approximation of particle size with same crystal structure. The numerical particle size calculation can be calculated by Scherrer Equation:

$$\tau = \frac{K\lambda}{\beta \cos\theta}$$

Where τ is the mean size of the ordered (crystalline) domains, which may be smaller or equal to the grain size; K is a dimensionless shape factor, with a typical value of about 0.9, but varies with the actual shape of the crystallite; λ is the X-ray wavelength; β is the line broadening at half the maximum intensity (FWHM); θ is the Bragg angle (in degrees). It is important to note that the lattice strain, the instrumental broadening and other factors that can cause peak width change are simplified and neglected. To determine the absolute particle size of a catalyst, electron microscopy imaging should be utilized as compensate technique.

2.2.2 Electron Microscopy

Catalysts morphology, composition, surface structure and particle size are factors that can affect reaction activity. Electron microscopy allows for imaging the surface to a resolution of at least the nanometer scale. Two main electron microscopy techniques were used in this dissertation are scanning electron microscopy (SEM) and scanning transmission electron microscopy (STEM).

SEM is used to obtain image by rastering a beam of high-energy electrons across a sample surface of varying topography. The most commonly used imaging mode employs secondary electrons that are emitted when the sample is excited by the electron beam. These electrons have low energy and ensure that the signal comes from the surface region of the specimen. The number of emitted electrons greatly depends on the angle of the sample surface with respect to the electron beam and the detector, which construct differences in brightness and therefore reveal the sample topography. Another imaging mode is based on backscattered electrons, which has higher energy. This mode is sensitive to the image intensity depends on the composition of sample, which can provide good atomic number contrast. SEM imaging allows for viewing of a large area of sample and it is very useful for identification of particle morphology.

Species identification is accomplished by collecting the characteristic X-rays emitted from the sample, in a technique known as Energy Dispersive X-ray Spectroscopy (EDS). Electron excitation causes ionization within the sample leading to X-Ray emission which can be analyzed by solid state energy dispersive detector. Before imaging, powder catalyst samples were placed on carbon tape adhered on an aluminum stub without conductive coatings. SEM images were obtained using a Zeiss Ultraplus Thermal Field Emission Scanning Electron Microscope.

While SEM provides a topographical image of a sample surface using backscattered and secondary electrons, STEM uses a focused beam of high-energy electrons to form a small spot that is raster-scanned over a thin sample to image the entire depth by detecting scattered or transmitted electrons. One useful imaging mode in STEM is high angle annular dark field. The intensity distribution of electrons scattered at high

angles follows approximately a $Z^{1.85}$ dependence corresponding to the Reutherford scattering cross-section. Due to the incoherent scattering the HAADF-STEM images refers to as Z-contrast images and are very useful to study catalysts containing small metal particles. However, when the Z of the support is higher than metal particle, there is no good contrast and thus cannot distinguish the small particle from support. In this case, spectroscopic imaging utilizing the inelastic scattered electrons for EDS can be exploited to generate elemental maps.

2.2.3 X-Ray Photoelectron Spectroscopy (XPS)

X-Ray Photoelectron Spectroscopy (XPS) is a surface sensitive technique to analyze catalysts surface elemental composition and elemental oxidation states. The physical principle is based on the photoelectric effect, which was first discovered by Albert Einstein in 1905. Photons of a specific energy are used to excite the electronic states of atoms below the surface of the sample. Electrons ejected from the surface are energy filtered via a hemispherical analyzer before the intensity for a defined energy is recorded by a detector. Since core level electrons in solid-state atoms are quantized, the resulting energy spectra exhibit resonance peaks characteristic of the electronic structure for atoms at the sample surface. While the X-ray may penetrate deep into the sample, the escape depth of the ejected electrons is limited to less than10nm for energies around 1400 eV. The photoemission process, obeys the following energy conservation rule:

$$h\nu = E_b + E_k$$

Where $h\nu$ is the photon energy, E_b is the electron binding energy, and E_k is the kinetic energy of the photoelectron. Conventional sources typically exploit the Kα radiation emitted by an Mg or Al anode to produce photons at a fixed energy of 1256 and 1486 eV,

respectively. The chemical environment in which the core electron is found prior to the photoemission event (the type of bonding, the oxidation state, the possible presence of adsorbates) results in distinctive BE shift.

2.2.4 X-ray absorption spectroscopy (XAS)

Synchrotron-based x-ray absorption spectroscopy (XAS) has proven to be a versatile structural probe for studying the local environments of atom in catalysts. It is a bulk characterization method and gives averaged results.

When a beam of X-ray photons passes through a material, the incident intensity will be decreased due to the adsorption of the material being irradiated. For a path length dx of the radiation through the material, the decrease dI is given by:

$$dI=-u(E)I\,dx$$

where the linear absorption coefficient u(E) is a function of the photon energy. Integral form of the equation is called Lambert's law:

$$I_t=I_0e^{-u(E)x}$$

When the energy of the incoming photons is large enough to excite an electron from a deeper core level to a vacant excited state, a sharp rise in the adsorption intensity appears. This sharp rise is denoted as absorption edge.

An X-ray absorption spectrum is typically divided into two energy regions: the X-ray Absorption Near-Edge Structure (XANES) region, which extends from a few eV below an element's absorption edge to about 50 eV above the edge, and the Extended X-ray Absorption Fine Structure or EXAFS region, which extends from about 50 eV to as much as 1000 eV above the edge. The EXAFS region can be used to resolve structural information including the average bond distance between neighbored atoms, coordination

number of a selected atom species, while the XANES region can be used to indicate oxidation states of the selected element.

2.2.5 Diffuse reflectance infrared Fourier transform spectroscopy (DRIFTs)

DRIFTs is a technique for analyzing surface catalytic reaction, adsorbate, adsorption sites and reaction intermediate. It offers the advantages of easy sample preparation. The electromagnetic radiation reflected by roughened surfaces is collected and analyzed in IR region, which is termed as diffuse reflectance infrared Fourier transform spectroscopy (DRIFTS). IR beam incident onto a solid sample surface can have specular reflection, diffuse reflection, and partly penetrates into the sample. The beam penetrated the sample can be absorbed within the particles or be diffracted at grain boundaries, giving rise to diffusely scattered light in all directions. In diffuse reflectance spectroscopy, there is no linear relation between the reflected light intensity (band intensity) and concentration, in contrast to traditional transmission spectroscopy in which the band intensity is directly proportional to concentration.

2.2.6 Temperature programmed reduction (TPR)

TPR is widely used to determine catalysts reducibility, which is greatly correlated with catalysts activity in redox reactions. The basic chemistry is utilizing H_2 to reduce lattice oxygen of catalysts and forming H_2O. The A typical process of TPR is flowing H_2 in an inert gas with fixed flow rate over a catalysts in furnace. Then the catalyst is heated up with a constant temperature ramping rate. The outlet gas passing catalysts is detected by a mass spectrometer, from which we could tell the H_2 consumption peak at certain temperature. A H_2 concentration calibration is employed to quantify the H_2 consumption peak. The higher the H_2 consumed, the richer lattice oxygen can be involved in the redox

reaction. The lower temperature the peak occurs, the more likely the catalysts can work at lower temperature.

2.2.7 Atomic adsorption spectroscopy (AAS)

Atomic absorption spectroscopy (AAS) is used to determine the elemental composition of catalyst samples. Here, AAS is used to quantify the amount of Pd loading present in prepared catalysts. It is known that ground state atoms strongly absorb light at a characteristic wavelength and that the amount of light absorbed at low atomic concentrations is linearly related to the concentration of the element. In AAS, samples are atomized and exposed to the path of a light source emitting at the characteristic wavelength of the material. To calculate the concentration of an unknown sample, the absorbance at the characteristic wavelength is measured and compared with a calibration curve prepared using standards of known concentrations.

For each analysis, the calibration samples were diluted to five different concentrations, which cover the expected concentration of the metal of interest. An example procedure for Pd samples is described as follows. Standard solutions of 0, 1, 2, 4, and 6 ppm Pd were prepared by diluting appropriate fractions of a stock solution of 1 mg/mL Pd in 10% HCl (Acros Organics). In the diluting procedure, 10 vol% HCl and 0.5% $LaCl_3$ were added to the samples for better sensitivity and accuracy. The Pd-containing samples and the five standard solutions were nebulized into an air/acetylene flame. A Pd hollow cathode lamp (Hamamatsu Photonics K.K.) was used as a light source. An example of AAS calibration curve is shown in figure 2.1, which gives the absorbance as a function of Pd concentration. The calibration curve indicates good agreement with a

linear fit over the 0-6 ppm range. This calibration was applied to the synthesized Pd catalyst samples in order to measure the actual Pd weight loadings on those samples.

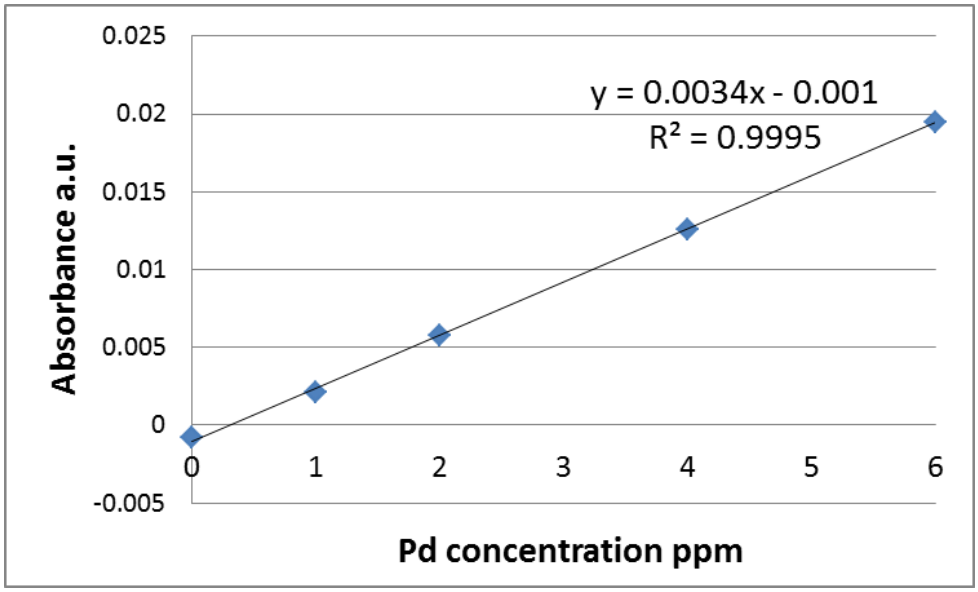

Figure 2.1 Pd concentration calibration curve measured from AAS.

2.3 Reactor and catalyst evaluation

2.3.1 Reactor design

A schematic diagram of the reactor system is shown in figure 2.2. The design consists of two tube furnaces with temperature controllers, H_2O injection system, carrier gas, mass flow controller. 1/2" stainless steel tube coated with inert silicon coating (Silcoalloy 1000) or 3/8" quartz tube is used to load the powder catalyst sample. Swagelok Teflon front and back ferrules are used to seal the reactor. The maximum temperature limit for these ferrules is ca. 250^{o}C. Since they are more than 3 inches far away from the heating part of the reactor, the real temperature of is much lower than the reactor temperature. After multiple reaction test with temperature range from 500-800^{o}C, the Teflon ferrules will be aged and lose the sealing. Leak check by using leak detector or

soap is necessary for each reaction test. If there is a leak, then the old ferrules should be changed. The reactor operated at near ambient pressure over a temperature range from 25-800 ℃. Industrial grade flue gases including 1%NH_3/N_2, 1%NO/N_2, 2%SO_2/N_2, O_2, CO, 2%C_3H_6/He and balanced N_2 or Ar that simulate coal and automobile emission conditions are each connected to mass flow controllers (Brooks 5850E). H_2O is combined with the carrier gas feed into a heated evaporator. The product stream was sent directly to a mass spectrometer (MS, Hiden HAL IV RC) for analysis. One reactor is used for catalysts reaction test, while the other is a blank one used for gas concentration calibration during the reaction. The reason for this design is because catalyst in a single reactor can covert reactant during temperature ramp and the MS reading of outlet gas concentration is unknown. In the blank reactor, there is no reaction occur. So the known concentration of a gas passing the blank reactor will not change between inlet and outlet, which is representative for real gas concentration and can be used for calibration.

Flow rate ratio of these two reactors w adjusted by a needle valve before the blank reactor. The flow rate is measured by a Sensidyne 800266-1 Gilibrator. Each flow rate is measured at least 3 times in steady state to make sure the reading is repeatable and accurate. The total flow is maintained at 800 sccm. The amount and volume of both catalysts and quartz wool could change in different tests, so the needle valve needs to be adjusted in each reaction test to achieve the targeted flow rate.

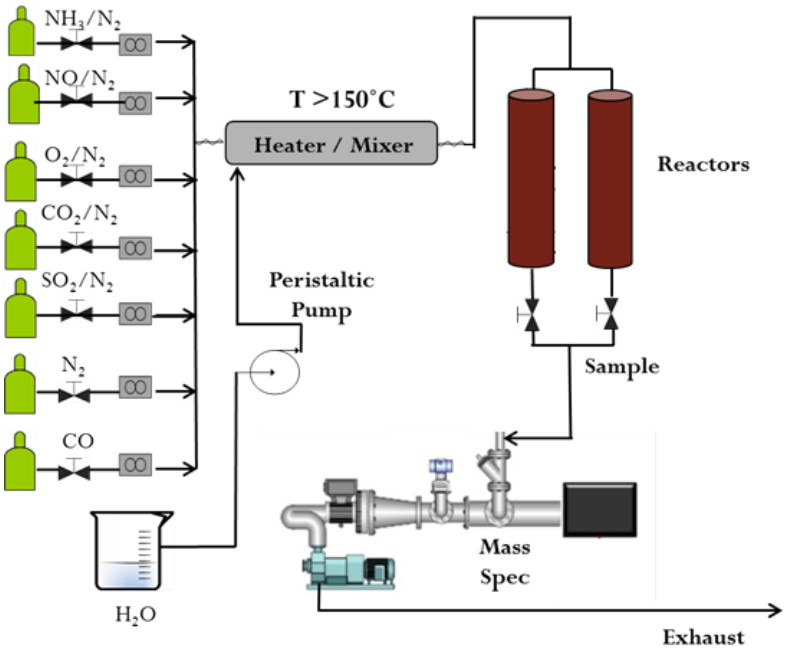

Figure 2.2 Illustration of reactor system.

2.3.2 Temperature control

The thermocouple setup is shown in figure 2.3 K-type thermocouple 1 (Omega Engineering, Inc., KMQ316SS-032U-12) was fitted into catalyst bed for reactor temperature monitoring. An additional thermocouple 2 is fitted into furnace for the purpose of interfacing with the temperature proportional integral derivative controller (PID controller, Omega Engineering, Inc., part number CN760000). The thermocouple 1 is placed into the catalyst bed to evaluate the impact of exothermic or endothermic catalytic reactions. The catalysts reaction temperature is reported by using the catalysts bed temperature. Since the furnace is not openable, the catalysts actual location in it is not visible. The length between the catalysts bed and the top of quartz tube is measure before loading the reactor. Then the length of thermocouple is marked as the same length so that it can reach the catalysts bed.

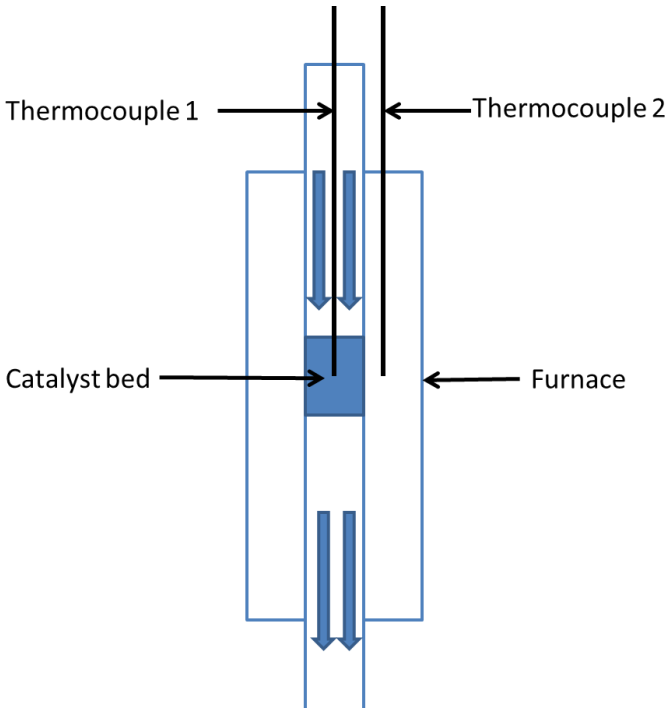

Figure 2.3 Thermocouple setup.

The process of temperature control is based on following steps: read the temperature using a K-type thermocouple (Omega), set the desired temperature, and control via a PID controller using LabView software. The reactor furnace is a high temperature ceramic radiant heater, supplied by Omega Engineering (CRFC-112/120-C-A). These furnaces are insulated with ceramic fiber and can go up to 900˚C (requiring a maximum of 5 Amps). A K-type thermocouple transmits signal to the chassis from National Instruments (NI CDAQ-9174), which sends an input signal to the PID controller in the PC. Once the temperature is set in the PC, the PC sends an output-triggering signal (ON-OFF command) to the 4-channel relay module (NI-9481), placed in the second slot of the NI chassis. The solid-state relay (Omega Engineering – SSRL240AC25) requires a

range of 90-280 V for operation and a circuit prior the SSR was added to obtain the needed power and voltage (120 V).

The final section of the temperature control system is the loop that allows the powering of the furnaces. Each furnace requires a 500 W (4.16 Amp, 120 V) for long furnaces. A variac autotransformer allows to step-up or step-down the voltage needed by the furnace. In the case of this temperature control system, the variacs are set at around 50%-70% of 120 V. For cases when the furnace's loop is overpowered, a 5 Amp fuse would work as a safety device, shutting down the circuit to prevent the breakdown of the furnace or the solid-state relay. During a reaction, the temperatures of blank reactor and the reactor with catalyst are set the same to maintain the similar flow distribution.

2.3.3 Mass spectrometer

A quadruple mass Spectrometry (Hiden Analytical (HAL 201-RC), operated with the MasSoft software) is used to analyze the outlet gas from reactors. The gas molecules entering the ultra-high vacuum(UHV) chamber are ionized via electron ionization to be converted majorly into positive charges. Then, the ionized molecules are accelerated from the ion source through a set of 4 rods with a hyperbolic electric field.

A UHV chamber for the mass spectrometry was built-in-house using vacuum components obtained from Kurt J. Lesker and/or Duniway Company. The chamber includes one 4-way reducing cross (C-0275) with 2 ¾" conflat flanges at two ends of 4 ¼"conflate flanges. At one end, the cross has a 45˚ elbow (L45-0275) and a 979 Series Pressure Transducer (Kurt J. Lesker) used to monitor the pressure of the chamber. The transducer is capable of obtaining pressure measurements in a wide range of conditions (atm–10^{-10} torr). The second end of the standard cross has the mass spectrometer from

Hyden Analytical, while the third end has a LVM Series Leak Valve (Kurt J. Lesker), which provides molecular gas flow into the chamber (leak rate: $3.0*10^{-5}$ torr/s). Generally, the achievable leak rate for leak valves are as small as $1*10^{-10}$ torr /s and they are bake-able up to T = 450˚C. The last end of the 4-way standard cross has a conical reducer nipple (Kurt J. Lesker: CRN600X450) and a turbo molecular pump (TurboVac 151, SN: 20900101555). The turbo molecular pump has a similar appearance to a turbine compressor in jet engines; i.e. it uses rotating blades mounted on a shaft to direct gas molecules into the vacuum chamber in the molecular flow regime.

In order to start the turbo molecular pump, the chamber needs to be at rough vacuum conditions first; therefore, a 2-stage rotary vane mechanical pump (Varian SD-451) was attached to the turbo pump exhaust to initially pull gas from the chamber and achieve the rough vacuum conditions. The pulled gas from the chamber goes into the roughing pump's low-pressure stage, then to its high-pressure stage, compresses it and then sends it to the exhaust at atmospheric pressure. It should be noted that oil is used in the internals of the roughing pump to lubricate the pump's mechanical components (e.g. bearings, seals, rotor and vanes). Any failure in the roughing pump's operation (e.g. not enough oil, oil leaks, power outage etc.) will cause malfunction of the turbo molecular pump and eventually damage it. Also, a valve was added to the mechanical pump (rough pump) to prevent back-diffusion of oil vapors to the vacuum chamber in cases when the turbo is turned off.

In order to achieve UHV conditions it is also necessary to bake-out the chamber. The baking procedure will remove any contaminants in the UHV chamber (e.g. water and minimum traces of hydrocarbons). Typically, the chamber is baked at temperatures

around 110-130˚C, while the elbow around the pressure transducer is baked at lower temperatures (ca. 80˚C) due to the transducer's temperature limitations. The ultimate pressure achieved with this turbo pump is $8*10^{-10}$ torr. (The maximum baking temperature during operation at conflat flange of turbo pump is 55˚C).

The mass/charge (m/z) ratio of the ions is detected either with the Faraday or SEM detectors in the 100 amu mass range. Maximum operable pressure of the Faraday detector is $1*10^{-4}$ torr. The disadvantage of this detector is the low sensitivity and delay time in the amplification system, which would explain why the signals vs. time appear noisy compared with the signals acquired with SEM detector. On the contrary, maximum operable pressure of the SEM detector is $5*10^{-6}$ torr and can give higher sensitivity than the Faraday. Both of detectors are used in the experiments depending on the concentration range of the gases.

The reference mass to charge ratios that needs to be monitored were obtained from the NIST chemistry web book. The detectors used for each gas component depend on the concentration that needed to be analyzed. For trace level(ppm) concentrations, the SEM was selected due to its higher sensitivity, accuracy and lower noise level. Carrier gases like Ar and N_2 were analyzed by Faraday detector. When the MS operation pressure is within $3*10^{-7}$ torr, all gasses will be detected by SEM.

The volumetric flow of the gas sample going to MS was reduced from 100 sccm to 20 sccm using a 50 μm orifice provided by Swagelok. Reducing the volumetric flow to 20 sccm allows a steady pressure in the UHV chamber, which is convenient when monitoring gas concentrations in steady conditions. However, the gas volume between

the orifice and leak valve is still very high compared to the volumetric flow that goes into the MS when we open the leak valve. This is the so called "dead volume", which can cause longer response time in the MS. In order to shorten the response time, a vacuum was created between the orifice and the leak valve using a roughing pump (Varian-SD-40) to improve the flow rate in such "dead volume", as shown in figure 2.4. With this design, the MS can catch the composition change in seconds and enables characterizations like H_2-TPR and CO-O_2 pulse reaction.

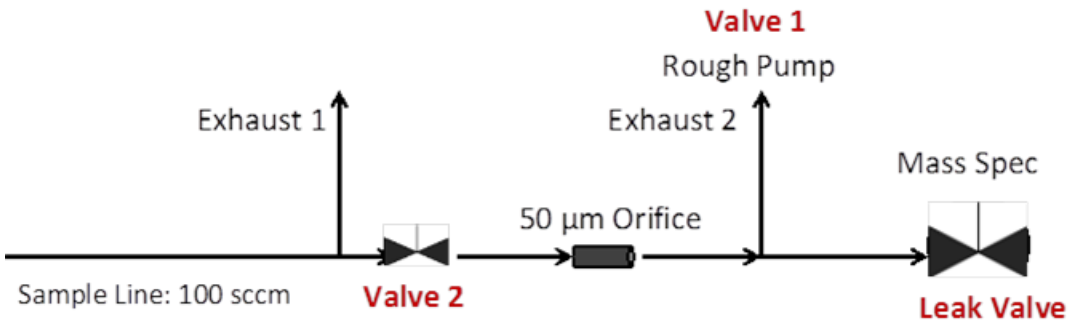

Figure 2.4 Mass Spectrometer sample line set schematic.

The operation sequence of this vacuum system is critically important. When gas flows are introduced into the system, valve 1 and 2 should be opened first, and then the leak valve can be opened slowly. After the reaction and calibration tests, the leak valve should be closed first, and then valve 1 and 2 can be closed. The reason is that the pressure in the MS is in 10^{-6} to 10^{-10} torr, which is much lower than the roughing pump (10^{-1} to 10^{-2} torr). If valve 2 is closed while valve 1 and the leak valve are open, the pressure difference can easily suck pump oil from the roughing pump to the MS chamber. This can cause contamination, which is a disaster for the high vacuum system and may need months to clean up the chamber.

For a typical reaction test, a MID mode in the MS is used to monitor the pressure change of each gas component as a function of time. The MS is turned on for 30 min, then Ar or N_2 inert gas flow is started and the leak valve is opened until the chamber pressure reaches $3*10^{-7}$ torr. Then the other gas flows and the temperature ramp are started. After the temperature and MS signal reach steady state, the reaction data is taken for analysis. Gas concentration calibration is done after each temperature ramp.

In the CO oxidation reaction, the m/z ratio for each gas is selected as follows: CO=28, O_2=32, Ar=40, H_2O=18, CO_2=44. It is important to note that CO_2 has ca. 10% fraction of m/z=28, which is overlapped with the m/z of CO. Hence, to calculate the CO conversion, such CO_2 contribution is subtracted from the CO signal. In the NH_3-SCR reaction, the m/z ratio of each gas is selected as follows: NO=30, NH_3=17, H_2O=18, O_2=32, N_2=28, CO_2=44, SO_2=64. The NO conversion is calculated by the formula: $(NO_{inlet}-NO_{outlet})/NO_{inlet}$, where NO inlet and NO outlet represent the concentration of NO inlet and outlet of the reactor, respectively.

2.3.4 Gas concentration calibration

MS is sensitive to a wide variety of gas concentrations. Prior to the reaction experiments, the mass spectrometer was calibrated at different concentrations to obtain a calibration curve for each respective gas component of interest. The concentration of the gas components were determined by back-calculating the calibration trend-line equation, shown in figure 2.5. The calibration experiments demonstrated a mass spec response time of 10 min every time a different concentration is selected. It would take more than around 20 seconds to receive response from the mass flow controllers because of the length of

the lines. Figure 2.5 shows the raw spectra and the calibration curve of CO in the range of 0% to 10% diluted in Ar. The concentration of CO is linear to the MS signal intensity (CO pressure).

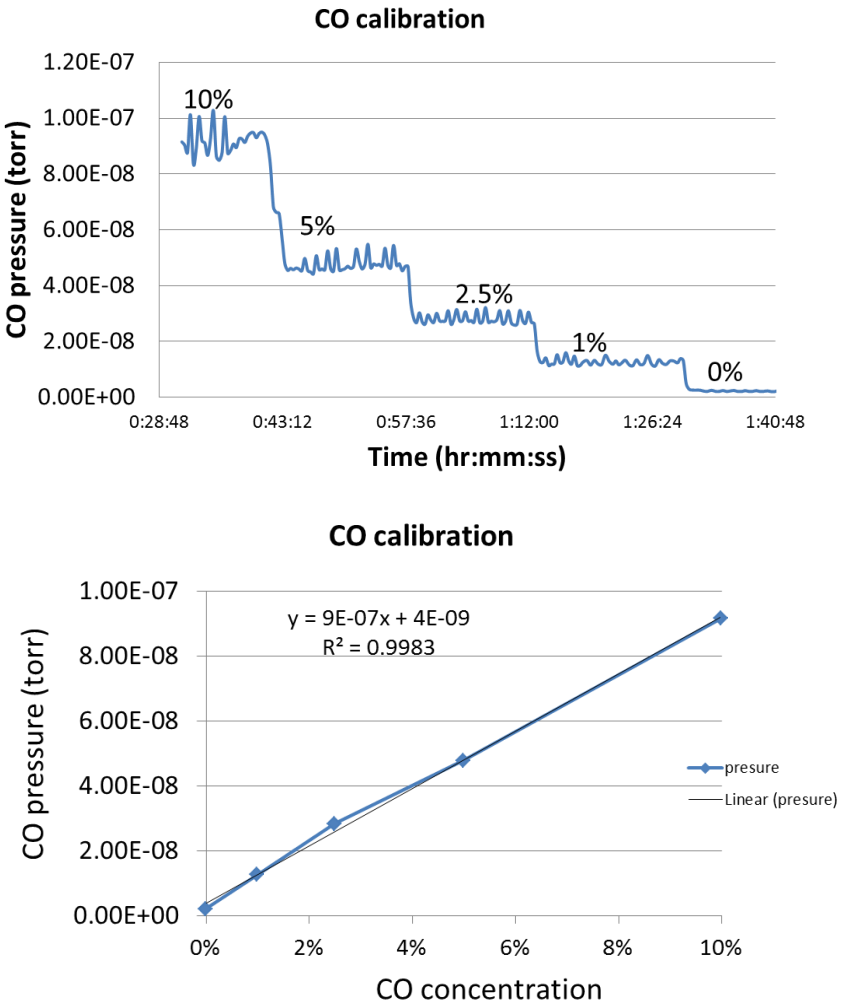

Figure 2.5 CO concentration calibration on the MS.

C_3H_6 has a much lower concentration than CO in diesel oxidation reactions, which is in the ppm level. The C_3H_6 calibration was carried out to make sure it is detectable by the MS, shown in figure 2.6. The calibration curve shows good linear relationship between concertation and the MS intensity. It is important to note that in this

case, the C_3H_6 pressure is normalized by the Ar pressure, which is the carrier gas. This is because the Ar pressure may fluctuate during the test and can lead to C_3H_6 pressure or signal fluctuation in the MS. Through normalization, the pressure fluctuation effect can be greatly reduced and the data quality was improved.

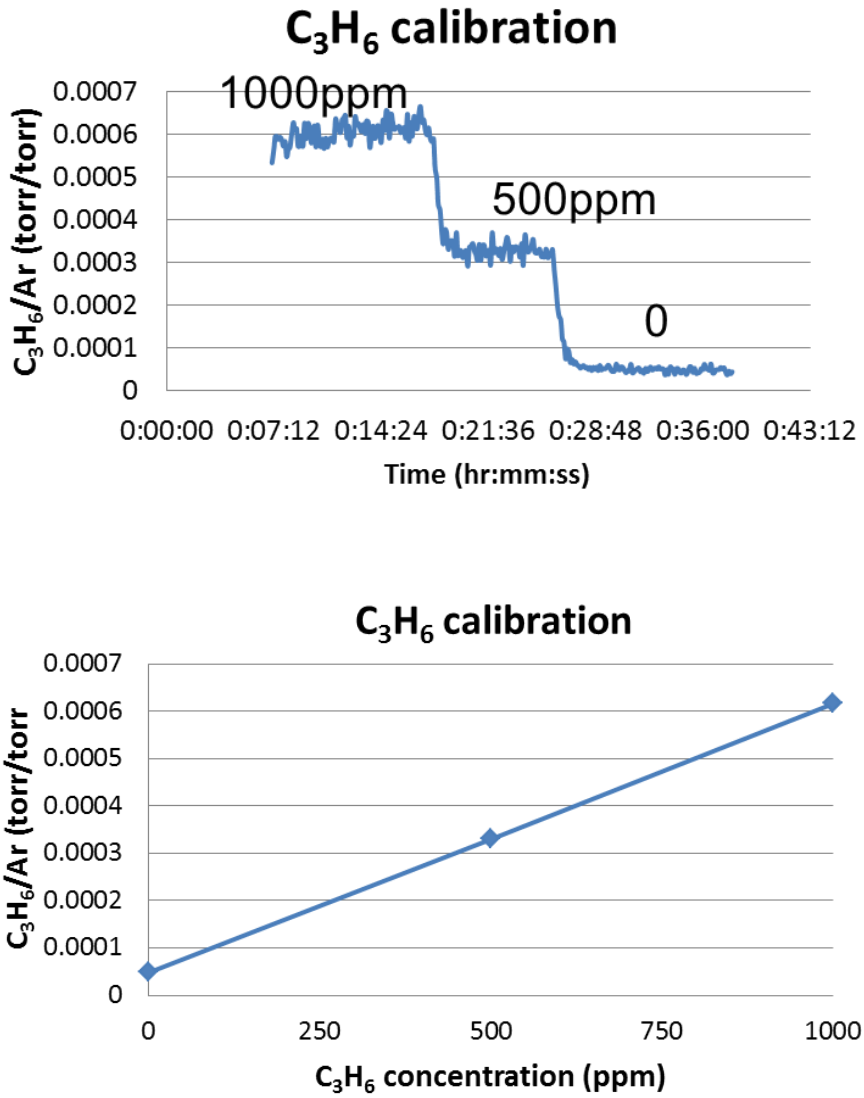

Figure 2.6 C_3H_6 concentration calibration on the MS.

2.3.5 Benchmark catalyst tests

The commercial 0.5% Pt/Al_2O_3 catalyst (Alfa Aesar) was used as a benchmark sample to validate traction and analysis systems. The catalyst was tested for CO oxidation under 150, 250, 350, and 450^oC for one hour at each temperature and the reactivity corresponds to steady state activity. A gas mixture of 2.0% CO (99.999% CO, Airgas), 5% O_2 (99.9999% O_2, Airgas) and balance Ar (99.9999% Ar, Airgas) was fed to the reactor via mass flow controllers. 200 mg of catalyst supported with quartz wool, was placed in the reactor for each run and no pretreatment was performed before the reaction. The corresponding gas hourly space velocity (GHSV) is 40,000 h^{-1}. CO conversion is calculated by the formula: $(CO_{inlet}-CO_{outlet})/CO_{inlet}$, where CO inlet and CO outlet represent the concentration of CO inlet and outlet of the reactor, respectively. Calibration of the CO concentration was carried out by switching to the blank reactor with known inlet concentrations, which generates 4 calibration curves at each temperature. One of the disadvantages of using mass spectrometry as analytical technique is the occurrence of spectral skewing. By definition, spectral skewing is the term used to describe how the relative intensities of mass spectral peaks vary due to the change in concentration of the analyte in the ion source. In addition, the intensity of signal in the MS can gradually decrease as running time increases. Hence, multiple calibrations could improve the data accuracy. The CO concentration was achieved by using the calibration function and averaged CO pressure during the reaction at each temperature.

In figure 2.7, the benchmark Pt/Al_2O_3 catalyst shows almost 0% CO conversion at 150^oC and over 95% conversion from 250^oC to 450^oC. The ramp up and ramp down curves match each other well, indicating good temperature control quality and

consistency. The conversion curves fit quite well with many reported Pt/Al_2O_3 catalysts. These tests validate the function and accuracy of the reactor and the MS. Most of the catalytic reaction experiments in this dissertation are based on this reactor system.

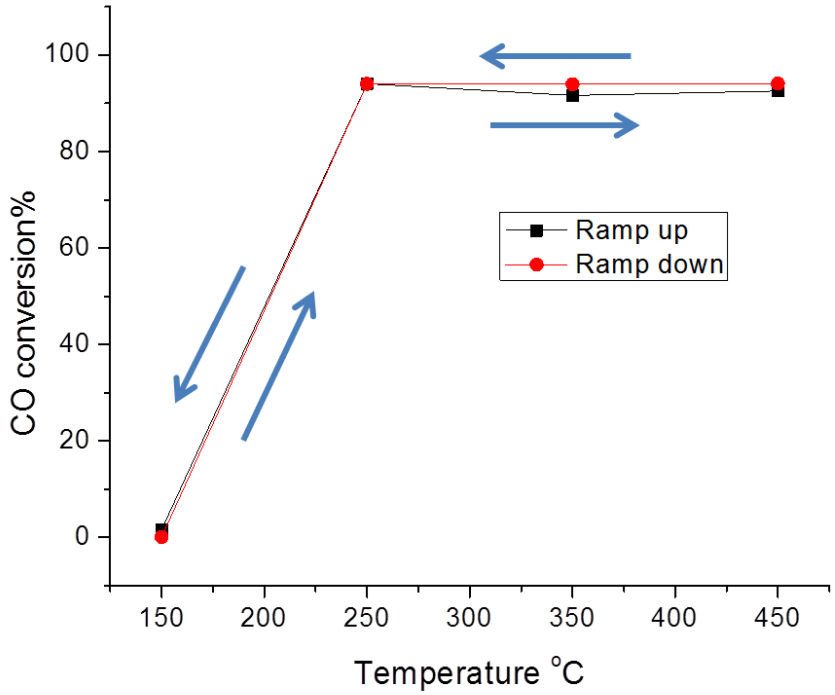

Figure 2.7 CO oxidation activity of benchmark 0.5% Pt/Al_2O_3 catalyst. CO/O_2 ratio of 2:5 and GHSV = 40,000 h^{-1}

Chapter 3

Superior oxygen transfer ability of Pd/MnO_x-CeO_2 for enhanced low temperature CO oxidation activity

3.1 Introduction

Carbon monoxide is a toxic pollutant and produced due to the incomplete combustion of carbon-containing fuels [77-78]. The majority of CO emissions come from mobile sources and catalytic oxidation of CO is the most widely used control technology to remediate CO emissions [78]. Even though the current commercialized platinum group metal (PGM) catalysts can reduce most of the CO content at temperatures above 200^{o}C, up to 80% of CO is still emitted during the cold-start stage of a vehicle due to the low operating temperature of the catalyst [78-80].

CeO_2 is a widely used component in mobile emission control catalysts due to the Ce^{3+}/ Ce^{4+} redox cycle [81-93]. CeO_2 can utilize lattice oxygen reversibly for CO oxidation depending on the exhaust gas composition, improve the dispersion of noble metals and enhance catalyst stability at high temperatures [81]. All these promoting effects shift the light-off temperature for CO oxidation to lower operating temperatures and provide a stable catalyst structure [82-93]. Addition of a PGM on CeO_2 as an active phase can create adsorption sites for CO and promote CO oxidation [88,92]. Among the PGMs, Pd based CeO_2 catalysts are shown to have fast light-off performance, high

oxidation capability, and better sintering resistance [93]. Recently, the effect of synthesis methods, incorporation of a different metal oxide into CeO_2, and the structural change of pure CeO_2 support have all been investigated to promote the low temperature activity (LTA) of the Pd/CeO_2-based catalysts for CO oxidation at reaction temperatures below 150 ℃ [94]. Generally, LTA can be determined by T_{90}, which denotes the temperature at which 90% CO conversion occurs. For instance, Meng *et al.* [95] reported a $PdO/Ce_{1-x}Pd_xO_{2-\delta}$ catalyst prepared by solution-combustion method, which showed a T_{90} of 130^{o}C. This catalyst exhibited a CO oxidation rate 100 times higher than PdO_x (x=1,2) species on pure CeO_2 at 130^{o}C and its increased activity was mainly attributed to a synergetic effect between the PdO_x species and the $Ce_{1-x}Pd_xO_{2-\delta}$ solid solution. In addition, another $Ce_{1-x}Pd_xO_{2-\delta}$ solid solution catalyst prepared via a plasma-arc method showed a lower T_{90} of 75^{o}C due to its high specific surface area and high defects concentration on the catalyst [96]. On the other hand, highly ordered mesoporous CeO_2 supported Pd catalyst showed excellent LTA for CO oxidation. For example, Jin *et al.* [97] reported that Pd supported on mesoporous CeO_2 synthesized by a KIT-6 silica hard template method showed a T_{90} of 90^{o}C. After H_2 reduction at 150^{o}C for 1 h, the T_{90} decreased to 50^{o}C. Moreover, Pd supported on mesoporous Co_3O_4-CeO_2 prepared by a surfactant-template method resulted in a T_{90} of 75^{o}C without performing a H_2 pretreatment [98]. A T_{90} of room temperature was also reported over Pd/CeO_2-TiO_2 catalysts, synthesized by sol-gel precipitation and subsequent application of supercritical fluid drying [99]. However, the LTA over Pd/CeO_2-TiO_2 did not remain stable at room temperature and the CO conversion dropped down to 20% in 2 h.

The low CO oxidation activity of the Pd/CeO_2 catalyst can be attributed to the existence of small PdO nanoparticles and Pd^{2+} ions in the form of a $Ce_{1-x}Pd_xO_{2-\delta}$ solid solution. Both of these Pd species can be obtained via conventional synthesis techniques, such as wet impregnation, co-precipitation, and solution combustion [87, 91, 95, 100, 101]. Pd^{2+} ions substituted into the CeO_2 framework by solution combustion show better CO oxidation activity at temperatures below 120^oC if compared to the Pt, and Rh metal ions [83]. However, up to 94% of Pd content in the solution combustion synthesis remains in the bulk and may have a little contribution to CO oxidation [91,95]. On the other hand, conventional wet impregnation can concentrate most of the Pd species on the CeO_2 surface, while still maintaining a high CO oxidation activity at low temperatures [94].

In addition to the synthesis methods, the OSC of CeO_2 could be enhanced by substituting Ce^{4+} with other cations, such as Y^{4+}, Zr^{4+}, La^{3+}, Sm^{3+}, Sn^{4+}, and Mn^{3+}, while still maintaining its cubic fluorite structure [102-107]. Among these metal oxides MnO_x has taken particular attention due to the unique catalytic redox performance of CeO_2-MnO_x and formation of large amounts of surface oxygen species on the Mn doped ceria. [108] For instance, Luo *et al* synthesized a series of Pd-doped mixed oxides CeO_2-MO_x (M = Mn, Fe, Co, Ni, Cu) by a surfactant-assisted co-precipitation method followed by a 2-day hydrothermal treatment, in which Pd-MnO_x-CeO_2 showed the best CO conversion with a T_{90} of 50^oC [108].

In this work, we present Pd supported on ceria based catalysts active for room temperature CO oxidation. Mn ions were incorporated into the CeO_2 support through a simple co-precipitation method. The catalysts were tested from room temperature to

450°C. The low temperature CO oxidation activity of Pd doped MC solid solution catalysts is investigated by means of in-situ X-ray absorption spectroscopy (XAS) and X-ray photoelectron spectroscopy (XPS). Dynamic reduction behavior of Pd^{2+} species in the presence of CO at low temperatures is characterized by in-situ diffuse reflectance infrared Fourier transform spectroscopy (DRIFTs). H_2 temperature-programmed reduction (TPR) and CO/O_2 transient pulse experiments are conducted to evaluate the lattice oxygen reducibility of Pd/CeO_2 and Pd/MC.

3.2 Experimental

3.2.1. Catalysts synthesis

The MC supports were prepared by an ultrasonic assisted co-precipitation method, where $Mn(NO_3)_2$, and $Ce(NO_3)_3$, with a mole ratio of 1:1, were used as the catalyst precursors and $(NH_4)_2CO_3$ (1 mol L^{-1}) as a precipitator. The paste obtained from co-precipitation was treated by ultrasound for 2 h, followed by subsequent filtration. The samples were then washed with deionized water, dried in stagnant air overnight at 105 ℃, and calcined in stagnant air at 500 ℃ for 6 h. Pd/MC with 1 wt% Pd loading was synthesized by impregnation. The MC support was immersed in aqueous $Pd(NO_3)_2$ solution and dried at room temperature while stirring. Then the solid was calcined in stagnant air at 550°C for 3 h. Similarly, Pd/CeO_2 was synthesized using the precipitation and impregnation method. The $Ce(NO_3)_3$ precursor was only mixed with the $(NH_4)_2CO_3$ (1 mol L^{-1}) precipitator and synthesized following the aforementioned procedure described for Pd/MC. The actual Pd loadings of Pd/MC and Pd/CeO_2 were measured by atomic absorption spectroscopy, and found to be 1.1±0.05 wt% and 1.0±0.05 wt %, respectively. Additionally, 5 wt% and 0.5 wt% Pd/CeO_2, and 5 wt% Pd/MC samples

were synthesized as a reference sample to compare Pd speciation. The Pd loading on 5 wt% samples were measured to be 5.1±0.05 wt% and 4.4±0.05 wt% on Pd/MC and Pd/CeO_2, respectively. The actual Pd loading on 0.5 wt% Pd/CeO_2 was 0.49±0.05 wt%.

3.2.2. Catalytic testing

CO oxidation experiments were conducted in a plug flow rector under atmospheric pressure. A gas mixture of 2.0% CO (99.999% CO, Airgas), 5% O_2 (99.9999% O_2, Airgas) and balance Ar (99.9999% Ar, Airgas) was fed to the reactor via mass flow controllers (Brooks 5850E). 200 mg of catalyst supported with quartz wool was placed in the reactor for each run and no pretreatment was performed before the reaction. The catalyst temperature was recorded using a thermocouple placed inside the catalyst bed. The gas hourly space velocity (GHSV) for all experiments was 40,000 h^{-1}. The amount of CO before and after the reaction was measured using a differentially pumped mass spectrometer (MS, Hiden HAL IV RC). CO conversion was reported at steady state at each temperature and calculated by using the following formula: $(CO_{inlet}-CO_{outlet})/CO_{inlet}$, where CO_{inlet} and CO_{outlet} represent the concentration of CO inlet and outlet of the reactor, respectively. The conversion error is calculated to be less than ±5% after repetitive tests.

The turnover frequency (TOF) of the Pd catalysts was calculated by using the following equation:

$$TOF = \frac{F * X}{n(Pd)}$$

where F is the flow rate of CO in mol s^{-1}, X is the CO conversion at 50°C, and n(Pd) is the mole of Pd in the catalyst.

3.2.3. Catalyst characterization

Powder X-ray diffraction (XRD) data for fresh samples were collected on a RigakuMiniflex II desktop diffractometer using a Cu Kα source with D/teX Ultra 250 silicon strip detector. XPS was carried out on a Kratos AXIS Ultra DLD XPS system equipped with a hemispherical energy analyzer. A monochromatic Al Kα X-ray source (1486.6 eV) was operated at 15 kV and 120 W. All spectra were calibrated to the adventitious carbon at 284.8 eV (C1s). The high-resolution elemental mapping and imaging of particles were collected using a FEI Talos F200X scanning transmission electron microscope (STEM).

XAS was collected at X-ray beamline 4-1 at the Stanford Synchrotron Radiation Lightsource (SSRL), Menlo Park, CA. The storage ring electron energy was 3 GeV with a current of 500 mA. Pd K-edge spectra were collected in the transmission mode with a Si (220) double-crystal monochromator that was detuned by 30% to minimize effects of higher harmonics in the X-ray beam. A Pd foil reference compound was placed between the I_1 and I_2 ion chambers to serve as a continuous energy calibration standard. A reference sample (PdO, 50 mg, Sigma-Aldrich) was mixed with boron nitride (BN, Sigma-Aldrich) (150 mg) to give an appropriate absorbance at the edge energy, whereas other samples (200 mg) were used without mixing with BN. Samples were than hand pressed inside the sample holder and loaded into the reaction cell, which was then evacuated down to 10^{-5} Torr [109]. PdO were cooled down using a liquid N_2 cryostat and

the Pd K-edge XAS of the sample was collected. Both Pd/CeO_2 and Pd/MC samples were first exposed to He at room temperature (ca. 25^oC) for 1.5 h. Subsequently, 1% CO and 0.7% O_2 balanced with He was introduced into the cell. The in-situ reaction was conducted at the reaction cell temperatures of room temperature (RT), 50^oC and 100^oC. Pd K-edge XAS of the samples was collected at each condition. The X-ray absorption near edge structure (XANES) analysis of the samples was performed using the Athena software [110].

Time resolved DRIFTs experiments were performed on a Bruker Equinox 55 spectrometer equipped with a deuterated triglycine sulfate (DTGS) detector. CO adsorption was performed over the Pd/CeO_2 and Pd/MC samples at 50^oC and atmospheric pressure. 2% CO balanced with Ar was injected to the reaction cell at a total flow rate of 50 sccm for 10min. The sample spectra were collected during CO adsorption with an accumulation of 32 scans at a resolution of 4 cm^{-1}. Background spectra were collected in Ar without the presence of CO.

The reduction properties of the catalysts were characterized through H_2-TPR experiments. 200 mg of a catalyst supported with quartz wool was placed in a quartz tube and no additional pretreatment was performed. A reduction gas of 10% H_2 balanced with Ar was introduced with a flow rate of 50 ml min^{-1}. The sample was heated up to 800^oC with a rate of 10^oC min^{-1}. H_2 consumption was monitored by a differentially pumped MS and calculated by integrating the peak area.

CO/O_2 transient pulse experiments were conducted in the aforementioned plug flow rector used for CO oxidation experiments. 200 mg of the 1wt % Pd/CeO_2 and Pd/MC catalysts were placed in the reactor and tested under the flow rate of 100 sccm.

Initially, the catalysts were pretreated with 5% O_2 for 30 min at 50^{o}C. Subsequently, the catalyst was purged with pure Ar for 30 min. Following the pretreatment, 2% CO balanced with Ar and 5% O_2 balanced with Ar were each cycled to the reactor every 10 min. Between each pulse, pure Ar was introduced to purge the residual gas for 10 min. The CO_2 (m/e=44), O_2 (m/e=32), CO (m/e=28), and Ar (m/e = 40) signals were monitored by the differentially pumped MS.

3.3 Results and discussion

3.3.1. Catalysts structure characterization

XRD was carried out to analyze the crystal structure of the samples. As shown in figure 3.1, the observed diffraction patterns in all samples can be attributed to the (111), (200), (220), (311) and (222) lattice planes of the cubic fluorite structure of CeO_2, indicating that Mn and Ce form a solid solution without appreciable phase separation. The change in the lattice parameter of CeO_2 after Mn addition and the physical properties (particle size, surface area, pore size) of Pd/CeO_2 and Pd/MC have been discussed in detail and published elsewhere [25]. The 1 wt% Pd/CeO_2 and Pd/MC catalysts do not show any diffraction peaks corresponding to Pd metal (40.2^o) or PdO (34^o, 42^o) [25,100]. The lack of Pd diffraction peaks can be due to the small amount of Pd loading or formation of highly dispersed small Pd nanoparticles [95,100]. Indeed, increasing Pd loading to 5 wt% on MC leads to the formation of a weak diffraction peak at 42^o, corresponding to crystalline PdO [100]. In the case of 5 wt% Pd/CeO_2, an even weaker diffraction peak at 42^o is observed. The broader full width at half maximum of the PdO peak for the Pd/CeO_2 sample indicates that smaller PdO nanoparticles might be forming on Pd/CeO_2 in comparison to Pd/MC.

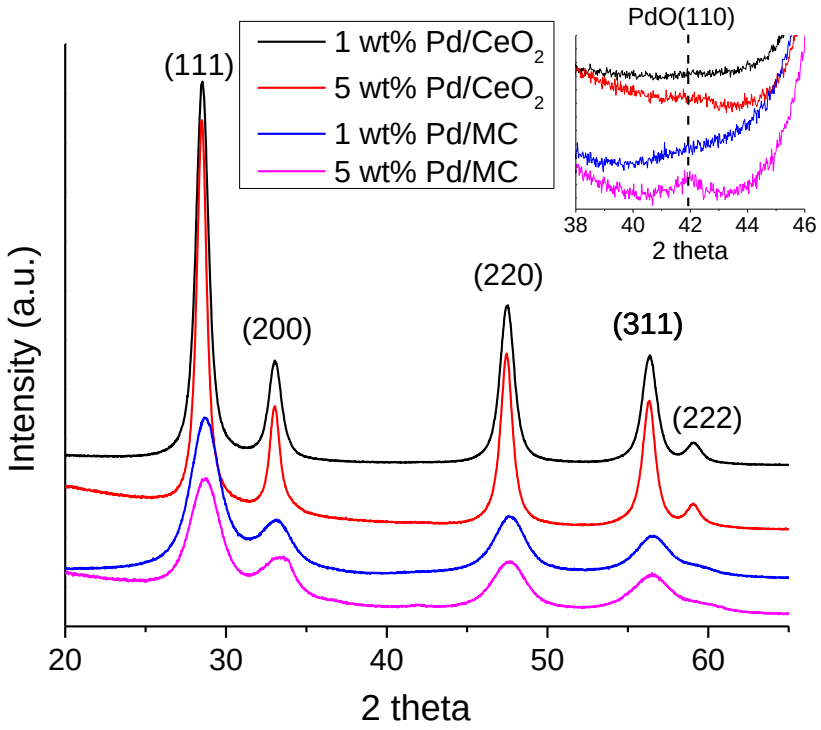

Figure. 3.1 XRD of the calcined 1 wt% and 5 wt% Pd catalysts.

To "find" Pd, several characterization methods were attempt to show Pd size and structure. Pd dispersion of Pd/MC and Pd/CeO_2 was tested with 150°C and 250°C H_2 pretreatment. With 150°C, Pd size of Pd/CeO_2 and Pd/MC are 1.7 and 4.5nm, respectively. With a followed 250°C H_2 reduction, Pd size of Pd/CeO_2 and Pd/MC grow to 2.7 and 7.4 nm, respectively. The XRD of reduced Pd catalysts after chemisorption is shown in figure 3.2. And metallic Pd (111) peak shows up. This indicates Pd dispersion can change with H_2 reduction and such chemisorption method is not accurate to characterize the initial Pd dispersion.

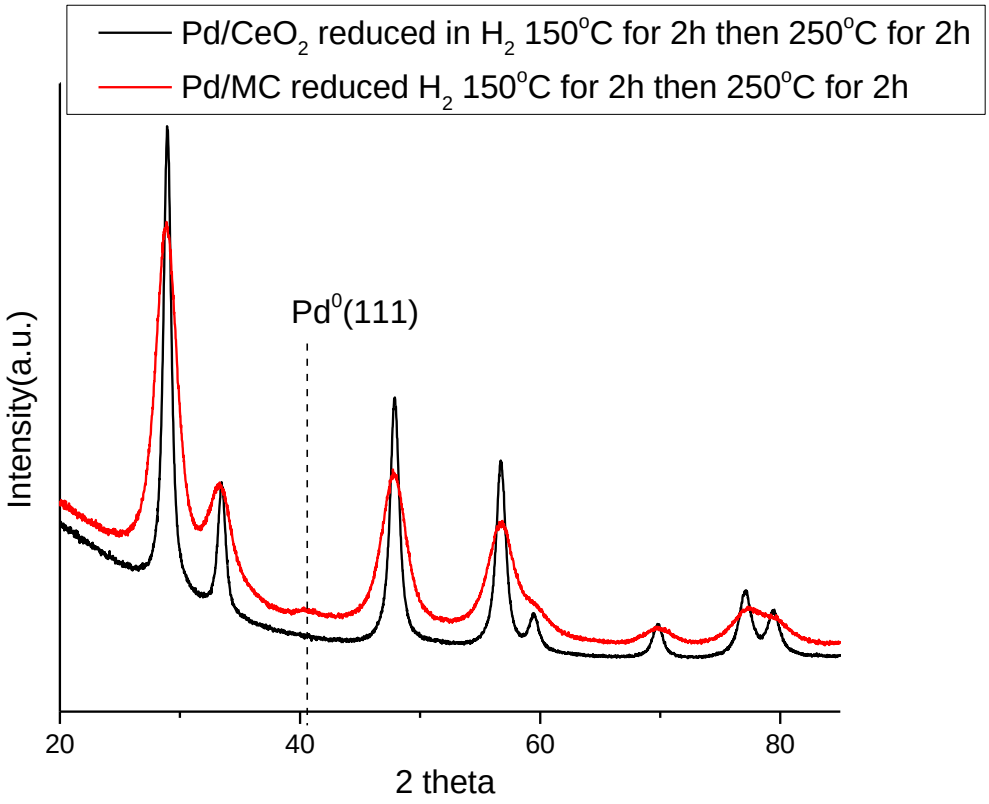

Figure 3.2 XRD analysis of reduced Pd/CeO_2 and Pd/MC

High resolution STEM was also attempted to identify Pd structure, shown in figure 3.3. Since Pd has lower Z number than Ce, some references reported that the darker area of the catalysts in STEM image should be Pd particles [95].The left image of Pd/CeO_2 shows bright and large CeO_2 crystal structure. Two interplanar spacings of 0.38 nm and 0.31 nm attribute to the (110) and (111) planes of CeO_2, respectively. The right image of Pd/CeO_2 shows a darker area at the edge of particle, which has an interplanar spacing of 0.19 nm. PdO (200) was reported to have a lattice spacing of 0.195nm, which is similar to this number. However, CeO_2 (220) has a lattice spacing of 0.19nm as well. Hence, it is very hard to confirm that the darker area is PdO particle due to the

overlapped PdO and CeO_2 interplanar spacing. The left STEM image of Pd/MC shows crystallite size around 3 nm, which is much smaller than CeO_2. Such observation is consistent with crystallite size calculated by XRD patterns of MC and CeO_2, which will be explained in Chapter 4. The right image of Pd/MC again shows a small darker particle with an interplanar spacing of 0.31 nm at the edge. This spacing can either attribute to CeO2(111) or PdO(100) plane, which is again hard to make a judgment of Pd structure. Thus, calculation of lattice distance is not a sufficient way to distinguish PdO from CeO_2 structure.

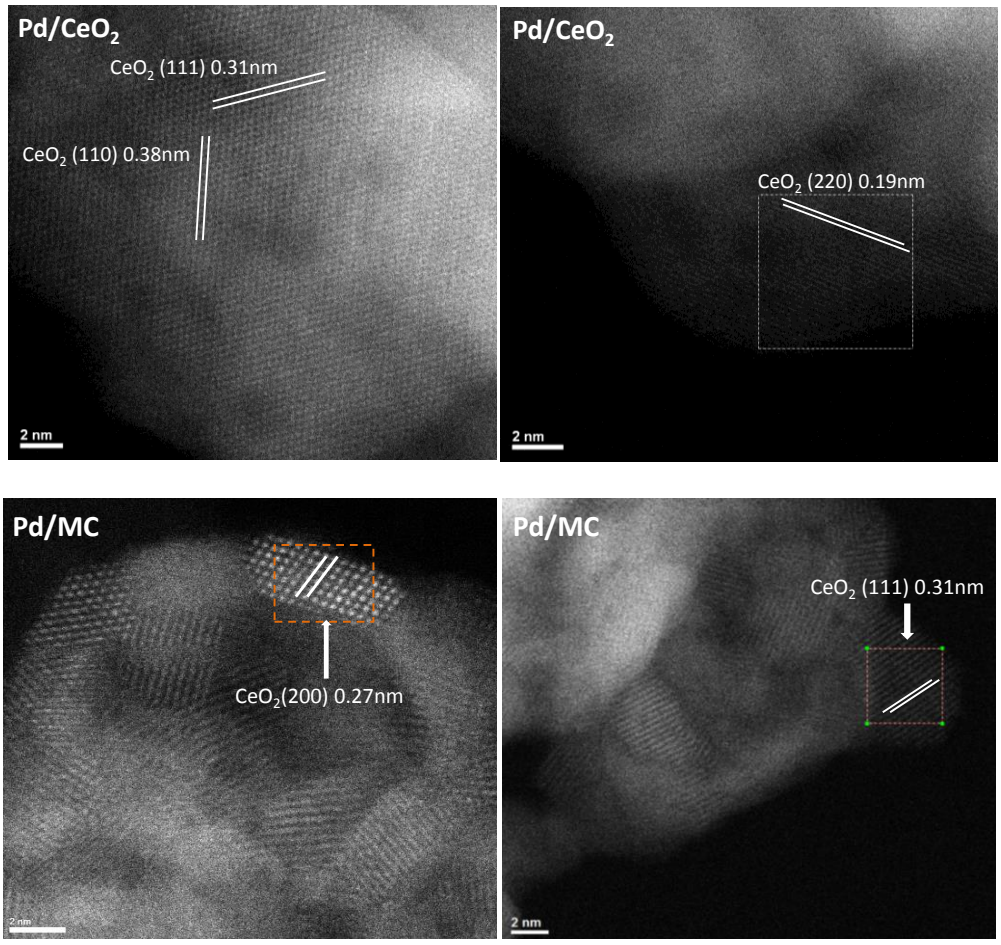

Figure 3.3 STEM images of fresh 1wt% Pd/CeO_2 and Pd/MC

As introduced in experimental section, the morphology and elemental distribution of Ce, Mn, and Pd in the 1wt% Pd/MC catalyst can be determined by STEM-EDX, as shown in figure 3.4. The freshly calcined sample comprises nanoparticles with spherical or elliptical shapes and sizes in the range of 20 and 40 nm. The high-resolution elemental mapping of the Pd/MC sample is able to distinguish different elements and indicates that all Ce and Mn are uniformly distributed within the sample structure, confirming the formation of a Mn-Ce solid solution. Pd mapping clearly shows that Pd is highly dispersed on the MC support, in consistent with XRD results.

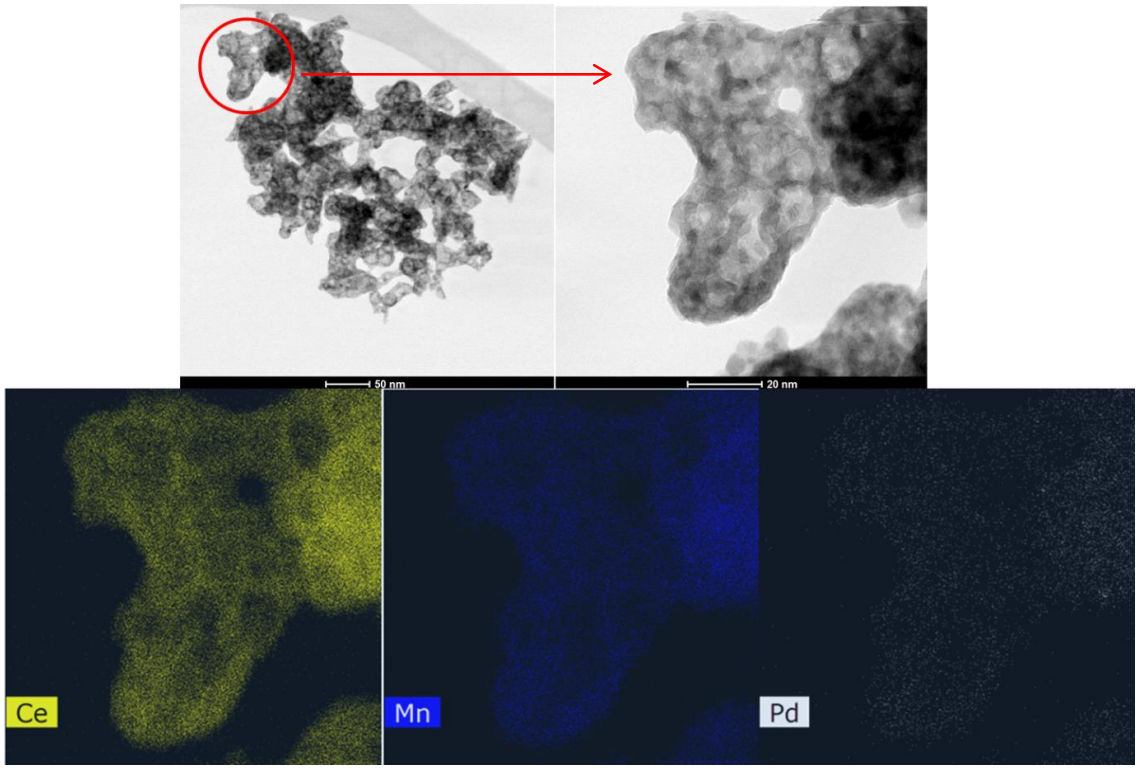

Figure 3.4 STEM images and high-resolution elemental mapping of the calcined 1 wt% Pd/MC. The STEM mapping was conducted by Dr. Michael J. Lance.

XPS was conducted to investigate Pd oxidation state and speciation on the CeO_2 and MC supports. As shown in figure 3.5, the $3d_{5/2}$ peak of the PdO reference sample locates at 336.6±0.2 eV with a full width half maximum (FWHM) of 1.16 eV, which is consistent with the literature [83]. The Pd $3d_{5/2}$ peak of 1 wt% Pd-CeO_2 can be deconvoluted into two peaks at 337.7±0.2 and 336.5±0.2 eV with a FWHM of 1.46 eV and 1.16 eV, respectively. In the case of 1 wt% Pd/MC, only a high binding energy peak is detected at 337.7 eV with a FWHM of 1.46 eV. The lower binding energy peak at 336.5±0.2 eV is similar to the PdO reference sample and can be attributed to the crystalline PdO phase, while the higher binding energy peak might be due to the formation of highly dispersed Pd^{2+} species or $Pd_xCe_{1-x}O_{2-\delta}$ interaction phase [86, 87, 111-112]. The crystalline PdO phase observed on 1 wt% Pd/CeO_2 accounts for 21% of the total Pd amount. As shown in figure 3.5, increasing Pd loading to 5 wt% on CeO_2 and MC does not affect Pd speciation. The 5 wt% Pd samples show similar Pd 3d core level spectra as the 1 wt% Pd samples. With the increased Pd loading, the MC support can still maintain all Pd species at a high Pd $3d_{5/2}$ binding energy of 337.7±0.2 eV. The 1.1 eV binding energy shift compared to the PdO reference sample could be due to the particle size influence on metal binding energy that arises from final-state screening effects. As the particle size decreases, the d-electrons are more localized and become less effective to screen the hole created by the photoemission. This effect leads to a decrease in relaxation energy of the final state and thereby increases the apparent binding energy [113-115]. As the Pd loading is decreased to 0.5 wt% on CeO_2, the Pd 3d binding energy for crystalline PdO phase disappears and only a high binding energy peak at 337.7±0.2 eV, corresponding to highly dispersed PdO nanoparticles, is observed. These results indicate

that highly dispersed PdO nanoparticles form first on the CeO_2 surface with the addition of small Pd loadings (0.5 wt%). The crystalline PdO phase forms at Pd loadings in between 0.5 wt% and 1 wt%, and its relative amount remains stable above Pd loadings of 1 wt%.

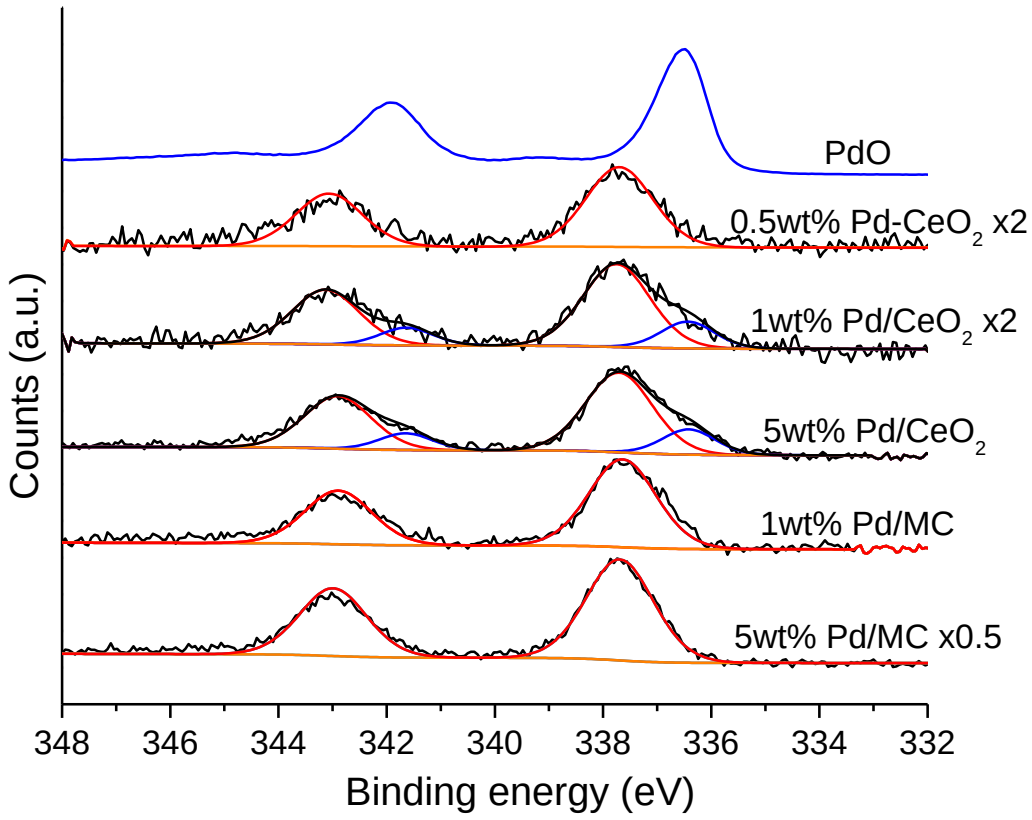

Figure 3.5 Pd 3d core-level XPS of the calcined Pd catalyst.

The oxidation state of Pd is further investigated through XAS experiments. Figure 3.6 shows the Pd K-edge XANES spectra of the 1 wt% Pd/CeO_2 and Pd/MC samples in the presence of He at room temperature. Both Pd foil and PdO were characterized as a reference sample. As shown in figure 3.6, the absorption edge of the PdO is measured to

be 24353 eV, which is consistent with the value in the literature [79]. In comparison to the XAS of the PdO reference sample, the Pd K-edge of Pd/CeO_2 and Pd/MC samples shifts to higher absorption energies by 0.6±0.2eV and 0.9±0.2eV, respectively. Such shifts are likely due to the chemical interaction of Pd^{2+} species with the support [116]. In any case, the absorption energy of the Pd K-edge for both Pd/CeO_2 and Pd/MC samples is above that of the Pd foil and shows similar features to the one of PdO. These results indicate that Pd is likely in the form of Pd^{2+} and no metallic palladium (Pd^0) exists in the freshly calcined samples. This is also in agreement with the XPS analysis, in which the Pd $3d_{5/2}$ binding energy at 335.3 eV corresponding to Pd^0 is not pronounced on the freshly calcined samples.

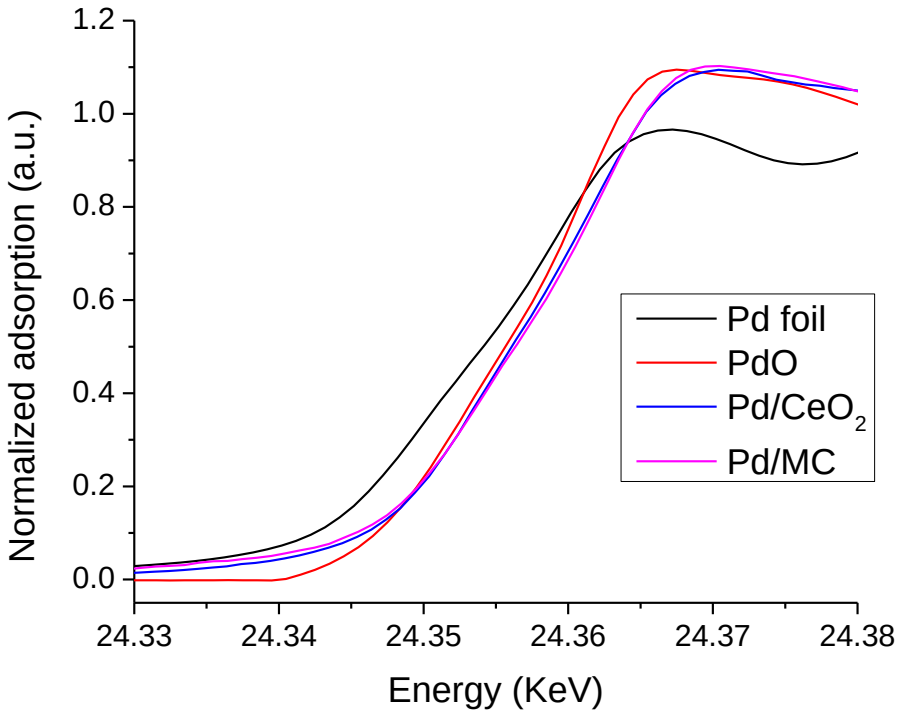

Figure 3.6 Pd K-edge XANES spectra of 1 wt% Pd/CeO_2 and 1 wt% Pd/MC recorded in He flow at room temperature. PdO and Pd foil are shown as a reference.

3.3.2. CO oxidation activity

Figure 3.7 shows the catalytic activity of the CeO_2, MC, 1wt% Pd/CeO_2 and 1 wt% Pd/MC samples for CO oxidation. The CeO_2 support has almost no catalytic activity for CO oxidation under 250^oC. After incorporation of Mn into the CeO_2 lattice, the T_{90} (temperature at which 90% CO conversion occurs) of the MC support decreases from 400^oC to 150^oC. The promotional effect of Mn addition for CO oxidation is likely due to a redox cycle between Ce^{3+}/Ce^{4+} and $Mn^{4+}/Mn^{3+}/Mn^{2+}$ ions, which increases the lattice oxygen mobility and redox property [117-118]. The improved oxygen mobility and redox property of the MC support could be associated with the decreased formation energy of oxygen vacancies [117]. It is proposed that the incorporation of Mn^{x+} ions into the CeO_2 (111) can decrease the single oxygen vacancy formation energy by inducing an unfilled Mn_{3d}-O_{2p} gap state between the O 2*p* valance band and the Ce 4*f* conduction band [118]. After impregnation of 1 wt% Pd, the Pd/CeO_2 catalyst shows almost 100% CO conversion at 100^oC, but decreases to ca. 40% at 50^oC. In the case of Pd/MC, almost 100% of the CO is already converted at 50^oC and such high conversion is maintained with increasing temperature.

The TOFs of Pd/CeO_2 and Pd/MC can be calculated assuming that either all of the Pd content or highly dispersed Pd species are active for CO oxidation [91]. If all the Pd content on the support is active, the TOFs of Pd/CeO_2 and Pd/MC are found to be 0.032 s^{-1} and 0.072 s^{-1} at 50^oC, respectively. Although the highly dispersed Pd species are considered as an active site, the TOF of Pd/CeO_2 slightly increases to 0.04 s^{-1}. These results indicate that CO conversion of Pd/CeO_2 and Pd/MC is not linearly correlated with the amount of highly dispersed PdO nanoparticles present on the surface, suggesting that

the dispersion of PdO nanoparticles is not the only factor that controls the catalytic activity at low temperatures.

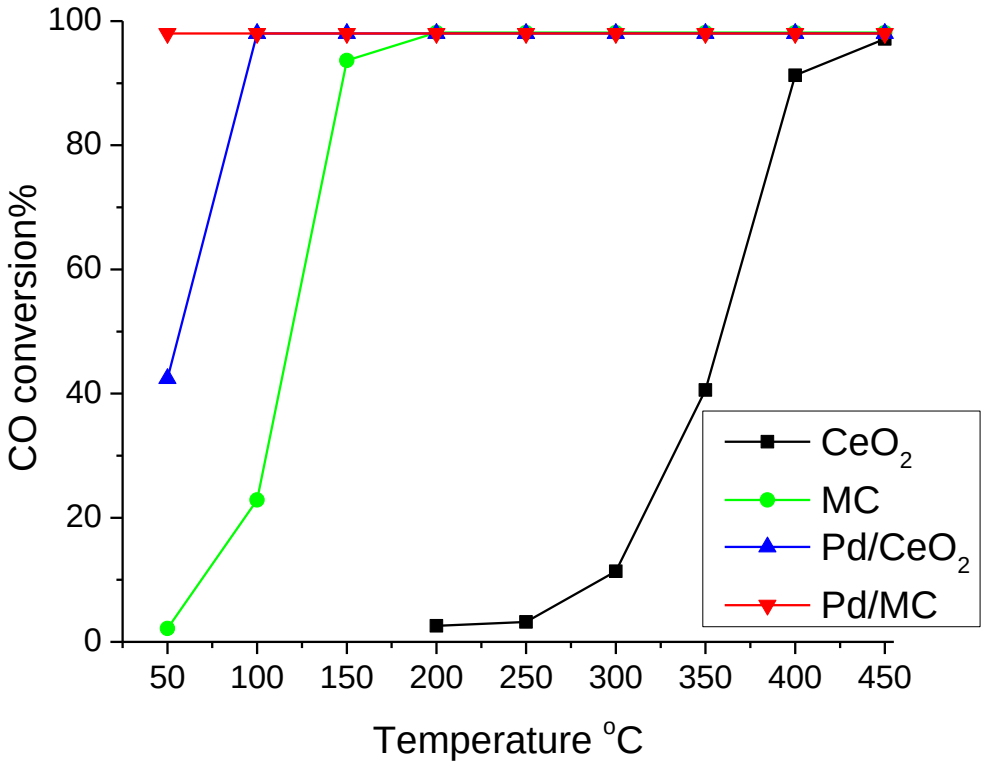

Figure 3.7 CO oxidation activity of CeO_2, MC and 1wt% Pd supported catalysts: CO/O_2 ratio of 2:5 and GHSV = 40,000 h^{-1}

CO oxidation is generally accepted to follow the Mars-Van Krevelen mechanism on the Pd-Ce based catalysts [119]. Active supports, e.g. CeO_2 and MC can participate the reaction by providing reactive lattice oxygen for CO oxidation [83]. Therefore, the high CO oxidation activity observed over Pd/MC could similarly be related with the lower oxygen vacancy formation energy [117-118]. To further understand the high

activity observed over Pd/MC at low temperatures, a series of *in-situ* and *ex-situ* characterization experiments were conducted.

3.3.3. In-situ XAS experiments

In-situ XAS experiments were conducted over the 1 wt% Pd/CeO_2 and Pd/MC samples to determine the change in Pd oxidation state during CO oxidation. For these experiments, a higher CO/O_2 ratio (1:0.7) was employed compared to the reactor tests (figure 3.7). This higher CO/O_2 ratio is not expected to impact the CO conversion mechanism in the presence of excess oxygen, as the reaction order is reported to be positive and nearly zero with respect to CO and O_2 on Pd/CeO_2, respectively [119]. The reactions with CO/O_2 ration (1:0.7) were tested and shown in figure 3.8**.** The CO conversion of Pd/CeO_2 and Pd/MC are similar under both high and low CO/O_2 ratio reaction conditions. This also suggests that Pd/MC may be able to work in other lean O_2 applications.

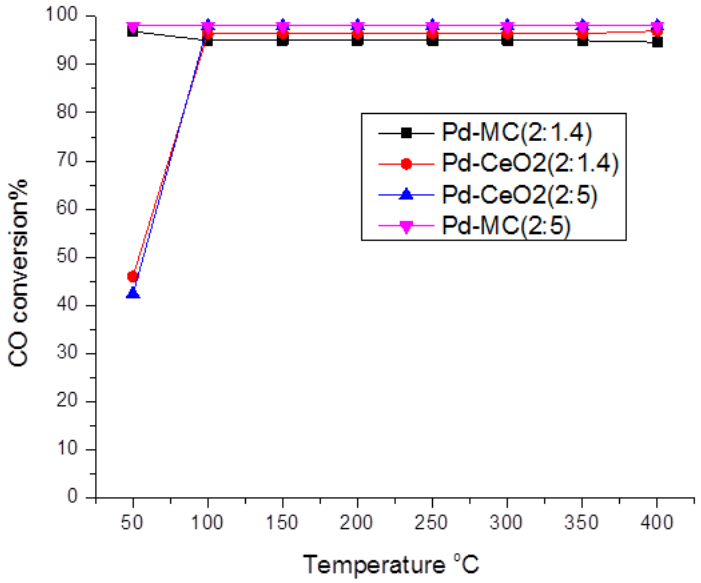

Figure 3.8 CO oxidation activities of Pd catalysts under high and low CO/O_2 ratio.

A linear combination fitting is employed to the XANES spectra of Pd/CeO_2 and Pd/MC via Pd foil and PdO reference samples to determine the change in the Pd oxidation state [120]. . As shown in figure 3.9 and table 3.1, upon injection of CO and O_2 at RT, a new feature appears at 24390 eV, corresponding to Pd^0 in the Pd/CeO_2 spectra. The quantification of Pd^0 formations on Pd/CeO_2 reveals that approximately 30±5% of Pd^{2+} is reduced to Pd^0 at 50°C. In comparison, there is only slight change of the XANES spectra of Pd/MC upon CO oxidation and up to 8±5% of Pd^{2+} is reduced to Pd^0. This indicates that the MC support can maintain almost all the Pd content in the oxidized state during CO oxidation.

The Pd K-edge EXAFS spectra of Pd/CeO_2 and Pd/MnO_x-CeO_2 samples were analyzed to determine the change in the local Pd structure during CO oxidation. A PdO bulk structure model is used to fit the data, as shown in figure 3.10. Upon CO and O_2 injection, the FT of k^3-weighted of Pd K-edge EXAFS spectra of Pd/CeO_2 shows new features at around 2.5 Å (phase uncorrected). These new features are visible at all temperatures and correspond to metallic Pd^0 (Pd-Pd shell)due to the reduction of PdO during CO oxidation, while Pd/MC does not show significant change. This is consistent with XANES results.

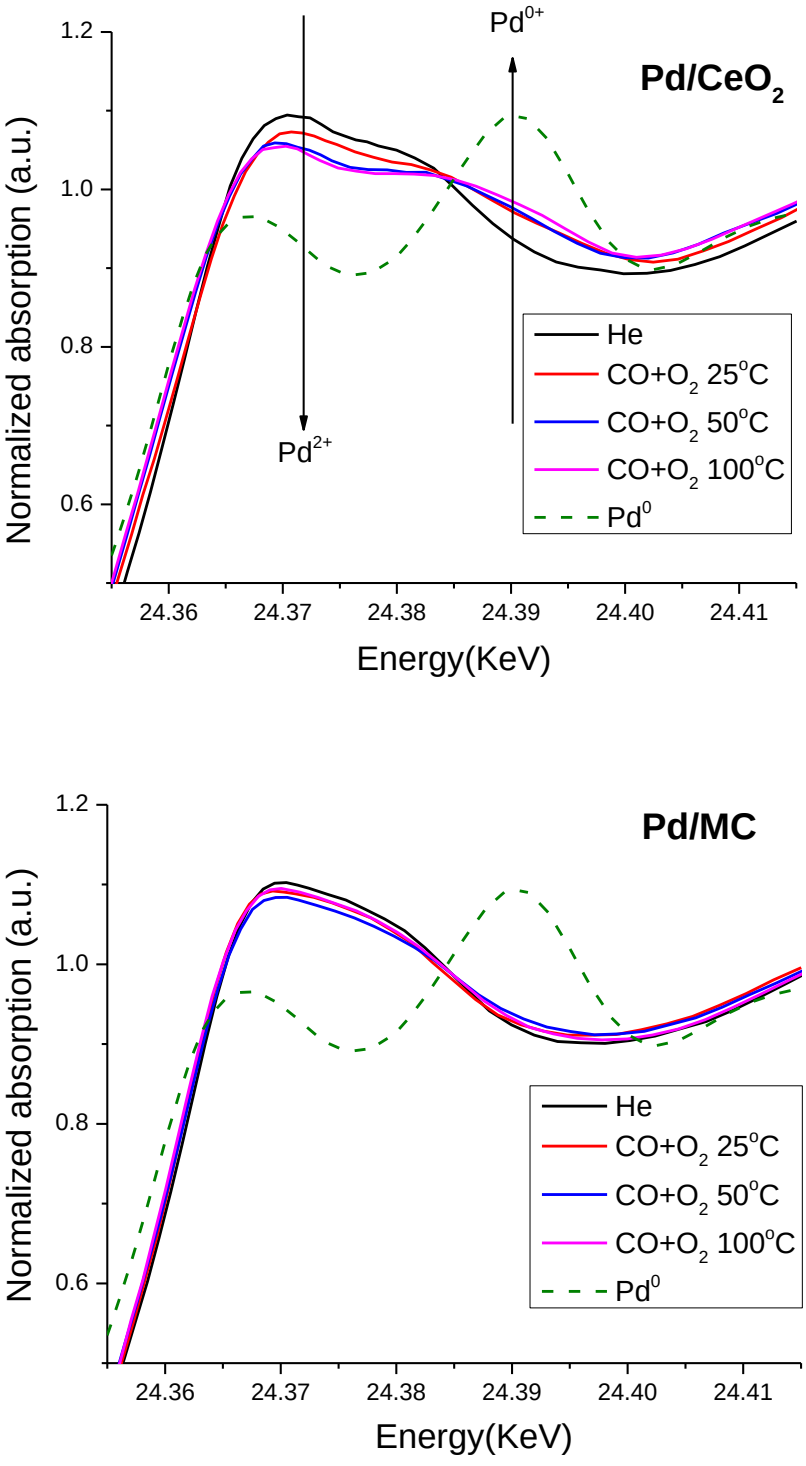

Figure 3.9 Pd K-edge XANES spectra of 1 wt% Pd supported catalysts during CO oxidation.

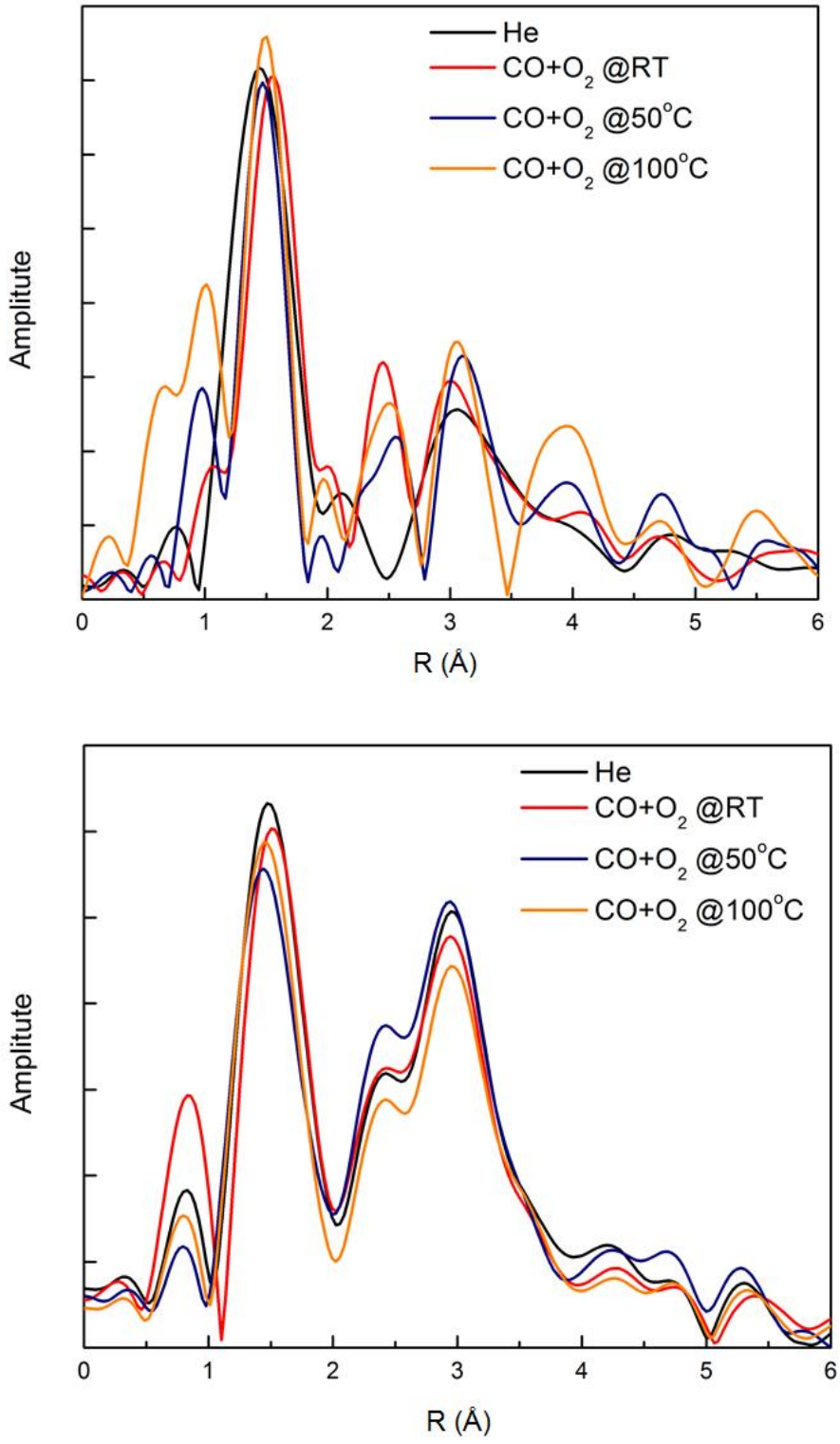

Figure 3.10 The FT of k^3-weighted of Pd K-edge EXAFS spectra of Pd/CeO_2 (top) and Pd/MC (bottom) during CO oxidation. The EXAFS data is analyzed by Dr. Erdem Sasmaz.

To identify different Pd^{2+} species formed on the catalyst surface after the in-situ XAS experiments, the catalysts were re-characterized via XPS. As shown in figure 3.11, Pd/MC shows only one single Pd $3d_{5/2}$ peak at 337.7 eV with the same FWHM that was observed on the freshly calcined sample, shown in figure 3.5 In agreement with the XANES analysis, the Pd^{2+} phase is maintained after CO oxidation on the MC support. In the case of Pd/CeO_2, an additional Pd $3d_{5/2}$ peak forms at 335.3 eV, corresponding to Pd^0 [90]. Quantification of the Pd 3d peaks of the Pd/CeO_2 spectrum reveals that 22% of the oxidized Pd amount is reduced to Pd^0 after CO oxidation. The amount of both oxidized Pd phases on CeO_2, i.e. highly dispersed PdO nanoparticles and crystalline PdO, decreases to 66% and 12% after CO oxidation, respectively. The amount of Pd^0 calculated by XPS is lower than the one estimated by in-situ XAS. This difference might be because of the re-oxidation of Pd^0 after air exposure or surface sensitivity of XPS [119].

Table 3.1 In situ XANES analysis of the Pd catalysts during He treatment and CO oxidation[a]

Catalysts	Pd oxidation state	Percentage of Pd^{2+} or Pd^0 at different conditions (%)			
		He	$CO+O_2$ 25°C	$CO+O_2$ 50°C	$CO+O_2$ 100°C
Pd/CeO_2	Pd^{2+} (±5%)	100	72	68	62
	Pd^0 (±5%)	0	28	32	38
Pd/MC	Pd^{2+} (±5%)	100	95	92	93
	Pd^0 (±5%)	0	5	8	7

a. The XANES spectra were fitted as a linear combination of the Pd foil spectra and the spectra of PdO reference.

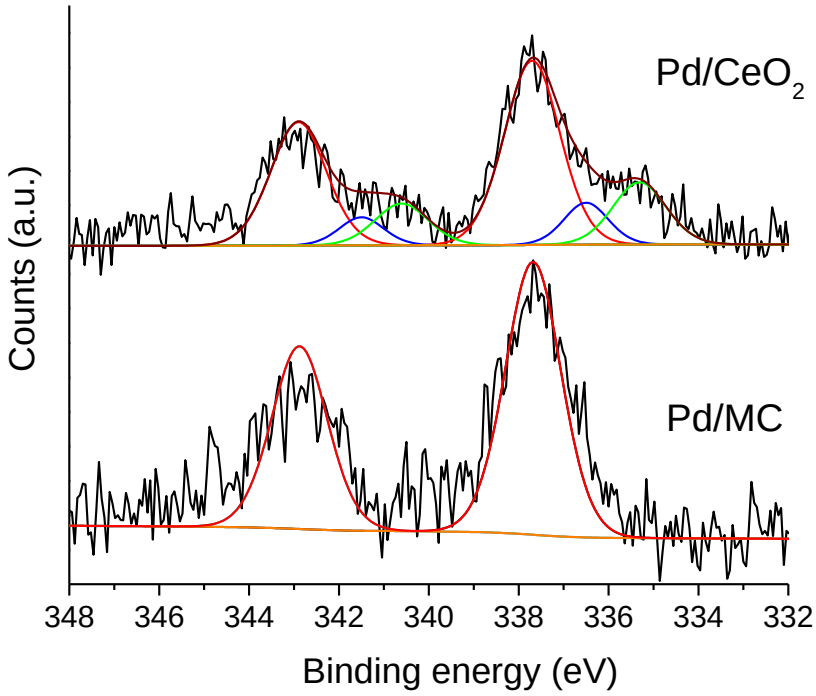

Figure 3.11 Pd 3d core-level XPS of 1wt% Pd supported catalysts after in-situ XAS experiment.

3.3.4. In-situ DRIFTs experiments

In-situ DRIFTs experiments were performed at 50°C to evaluate the Pd adsorption sites during CO exposure over Pd/CeO_2 and Pd/MC. The IR spectra were collected as a function of time to determine the reducibility of the oxidized Pd sites on the supports. As shown in figure 3.12, Pd/CeO_2 shows a band at 2088 cm^{-1} after 30 s of CO exposure, which is assigned to CO adsorbed on an atop site of Pd^0 [42]. At the same time, a weak broad band appears between 1980–1800 cm^{-1}, corresponding to chemisorbed CO on Pd^0 bridge (1980–1860 cm^{-1}) and threefold hollow sites (1920–1800 cm^{-1}) [42]. CO adsorbed on Pd^{n+} sites in the range of 2150-2100 cm^{-1} is not observed during these experiments, which could be due to the fast reduction of Pd^{2+} at high CO concentrations ,

shown in chapter 4. The integrated peak area of the IR bands for atop, bridge-hollow sites as well as gas phase CO_2 for both catalysts is plotted as a function of CO exposure time, as shown in figure 3.12c and 3.12d. Unlike Pd/CeO_2, Pd/MC shows significant gas phase CO_2 band in the first 30 s of CO exposure, meanwhile no bands for CO adsorbed on Pd^0 sites could be detected. After 60 s of CO exposure, a band for CO adsorbed on atop Pd^0 sites at 2092 cm^{-1} begins to grow on the Pd/MC sample, while a broad band at 1980-1800 cm^{-1}, corresponding to bridge and hollow sites appears only after 120 s of CO exposure. As the reaction continues, the intensity of all these sites grows appreciably. In addition to the CO bands, carbonate species form on the surface of both catalysts in the spectra range between 1650 and 1150 cm^{-1} during the first 30 s of CO exposure (see figure 3.13), indicating that surface oxygen species might be responsible for the formation of carbonate species [121].

The DRIFTs experiments reveal that oxidized Pd on CeO_2 can be reduced immediately in the first 30 s of CO exposure, forming Pd^0 sites. In the case of Pd/MC, Pd^{2+} species do not get reduced during CO adsorption immediately. Since there is no gas phase O_2 fed to the DRIFTs cell, Pd^0 is likely get re-oxidized by the lattice oxygen from the supports, which is in agreement with the re-oxidation behavior observed on the Pt/CeO_2 catalysts [122]. However, this re-oxidation on MC might be fast enough that the CO-Pd^0 band could not be detected until the first 60 s of CO exposure, while there is still CO_2 production during this time.

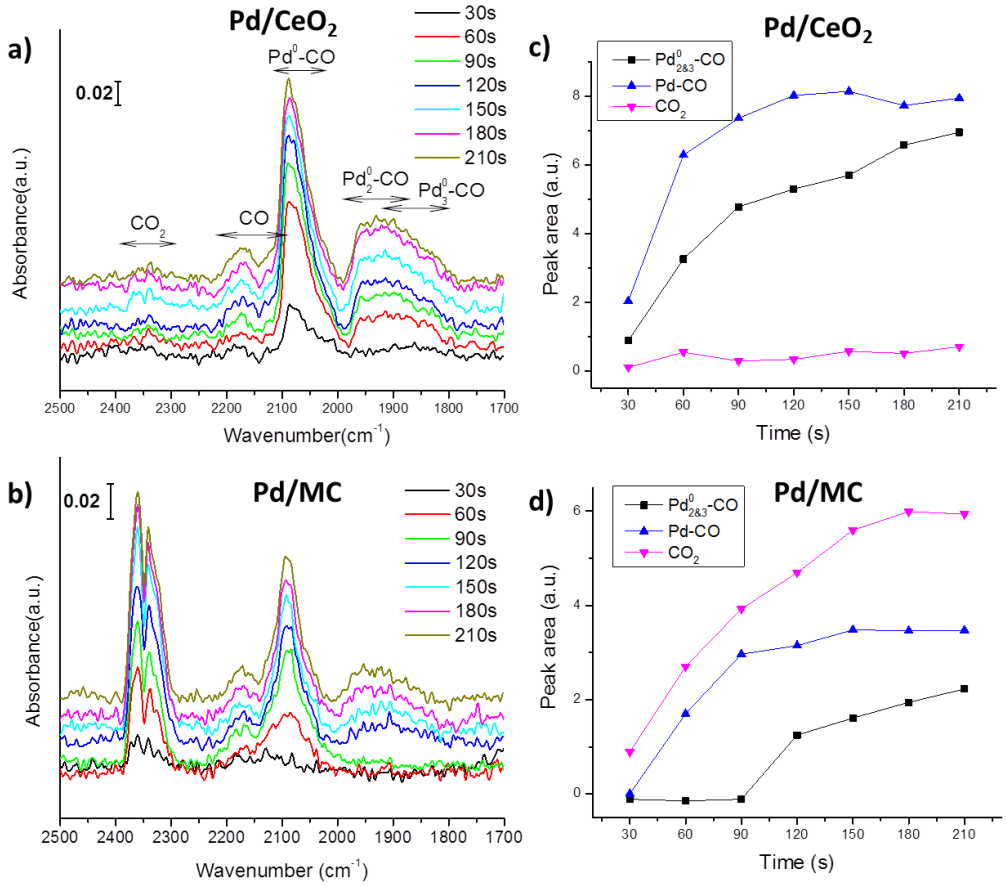

Figure 3.12 a,b) Baseline corrected in-situ DRIFT spectra of CO chemisorption over Pd catalysts. c,d) Peak area integral of CO adsorption sites and CO_2. Gas phase CO band was subtracted from atop Pd^0-CO sites.

Appearance of the bands for the adsorbed CO on bridge and hollow sites after 120 s implies that MC can suppress the formation of adjacent metallic Pd-Pd sites. The higher re-oxidation capability of MC again can be attributed to the decreased formation energy of oxygen vacancies [117-118]. In addition, many studies reported that a charge transfer exists between PGM and CeO_2 [123-125], which could be coupled with oxygen transfer for low temperature CO oxidation activity. During the charge transfer, Pd^0 can transfer

electrons to Ce^{4+}, forming oxidized Pd and Ce^{3+} with oxygen vacancy, which can facilitate the release of lattice oxygen [123-125].

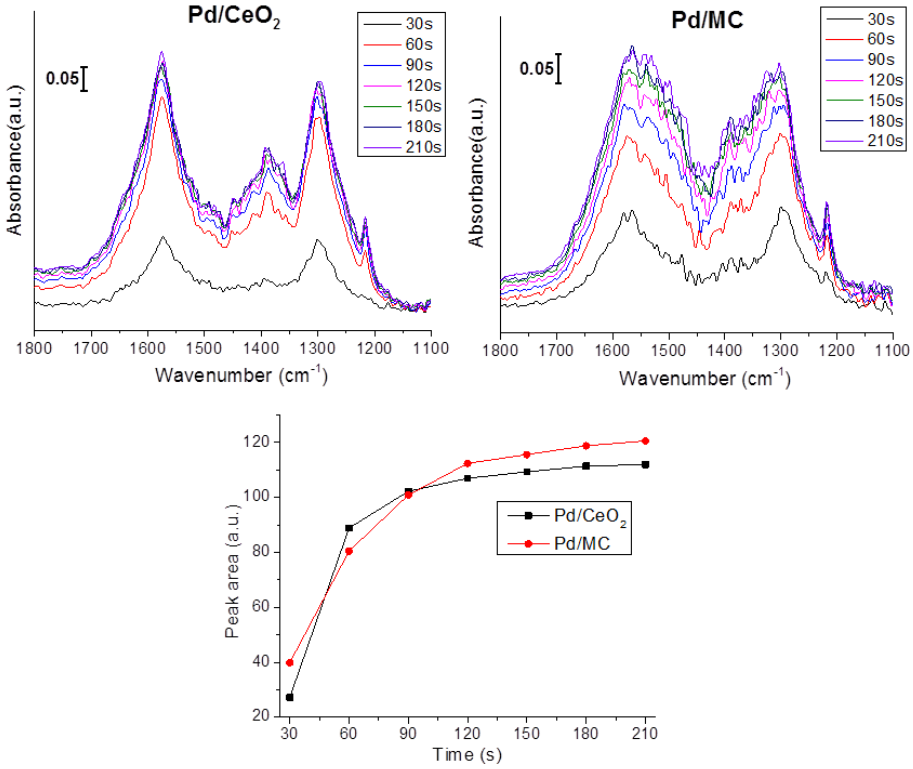

Figure 3.13 a,b)Baseline corrected in-situ DRIFT spectra of CO chemisorption over Pd catalysts. c) Peak area integral of peaks range from 1800 to 1100cm^{-1}.

3.3.5. Reducibility of lattice oxygen

Reducibility of the lattice oxygen is investigated through H_2-TPR and CO/O_2 transient experiments. As shown in figure 3.14, the CeO_2 support exhibits two weak reduction peaks at around 500^oC and 800^oC, which can be attributed to the reduction of surface and bulk oxygen species, respectively [126]. The reduction profile of MC also shows two reduction peaks at lower temperatures than CeO_2. The first reduction peak of

MC at around 250 ℃ corresponds to the reduction of Mn^{4+} to Mn^{2+}/Mn^{3+}, while the second peak at 370 ℃ can be attributed to the reduction of Mn^{2+}/Mn^{3+} to Mn^{2+} and surface oxygen of CeO_2 [127]. The downshift in the reduction temperature after Mn doping might be due to the facile redox cycle and enhanced oxygen mobility [127]. It is also possible that dissolution of MnO_x-CeO_2 solid solution during H_2 reduction can affect the TPR profile. At lower reduction temperatures, e.g. 250 ℃, the reduced Mn^{3+} may not necessarily separate from the CeO_2 fluorite structure, as reported after multiple H_2-O_2 redox cycles [128]. However, it is possible that further reduction of Mn^{3+} to Mn^{2+} at 370 ℃ might lead to a distortion in the fluorite lattice and eventually a phase separation. With the addition of Pd, 1wt% Pd/CeO_2 shows a reduction peak at 140^{o}C, which can be ascribed to the reduction of PdO to Pd^0 [100]. The amount of H_2 consumed at 140^{o}C is calculated to be $2.1*10^{-5}$ mol. This value is close to the amount of Pd ($1.9*10^{-5}$ mol), calculated using the actual metal loading reported in section 2.1. The similarities in between the amount of H_2 consumed and the Pd content in the CeO_2 was also reported in the literature and is consistent with this work [129]. Based on the XPS and XAS results, we can also assume that all the Pd in the sample is oxidized to PdO. In the case of Pd/MC, the reduction peaks of the MC support observed at 250 ℃ and 370 ℃ disappear and a single reduction peak at 140^{o}C with a total H_2 consumption of $4.1*10^{-4}$ mol is observed. This value is approximately 20 times bigger than the actual Pd amount on MC and close to the measured H_2 consumption of the MC support ($4.3*10^{-4}$ mol). The similar amounts of H_2 consumed over Pd/MC and MC indicate that the bulk lattice oxygen of MC can be extracted and reacted at lower temperatures in the presence of Pd. The disappearance of the high temperature reduction peaks on the Pd/MC sample can be

attributed to lattice oxygen reduction by H_2 spillover or oxygen reverse spillover from the support [79-81, 130], which is also pronounced in the XAS and DRIFTs experiments. As shown in figure 3.11, the lack of CO-Pd^0 bands during the first 30 s of CO exposure reveals that the Pd^{2+} can be reduced by CO and then re-oxidized by the lattice oxygen from the MC support. Such oxygen reverse spillover contributes to the stabilization of Pd^{2+} during CO oxidation, as shown in figure 3.9.

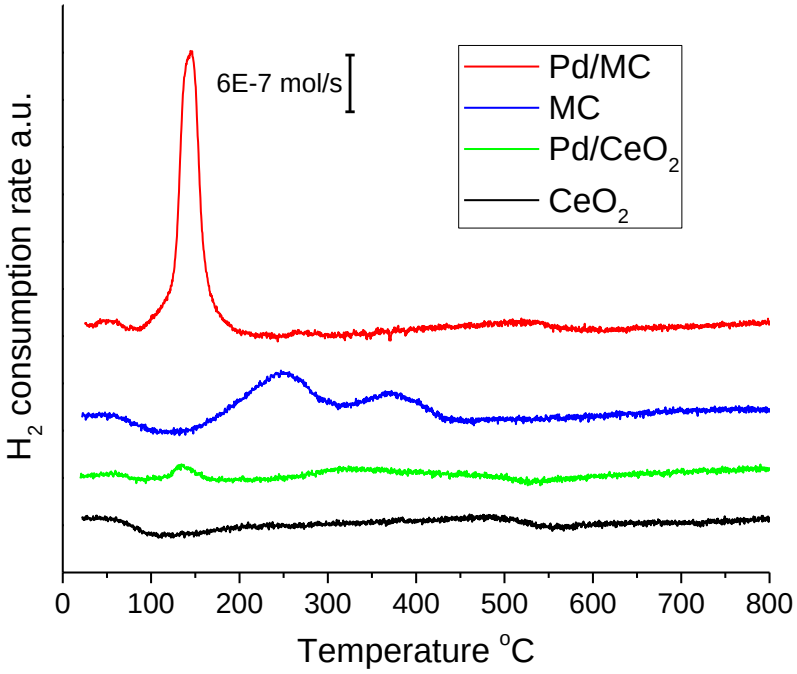

Figure 3.14 H_2-TPR profiles of the CeO_2, MC, and 1 wt% Pd catalysts.

In addition to the H_2-TPR experiments, CO/O_2 transient pulse experiments were carried out at 50°C to evaluate the oxygen transfer of the Pd deposited CeO_2 and MC supports. As shown in figure 3.15, CO_2 is immediately produced on Pd/CeO_2 and Pd/MC upon exposure to CO only, which is consistent with the DRIFTs experiments. The initial CO pulse produces $1.5*10^{-4}$ mol of CO_2 on Pd/MC, which is much higher than the amount of Pd^{2+} (ca. $2.0*10^{-5}$ mol) on the catalyst, indicating that the lattice oxygen from.

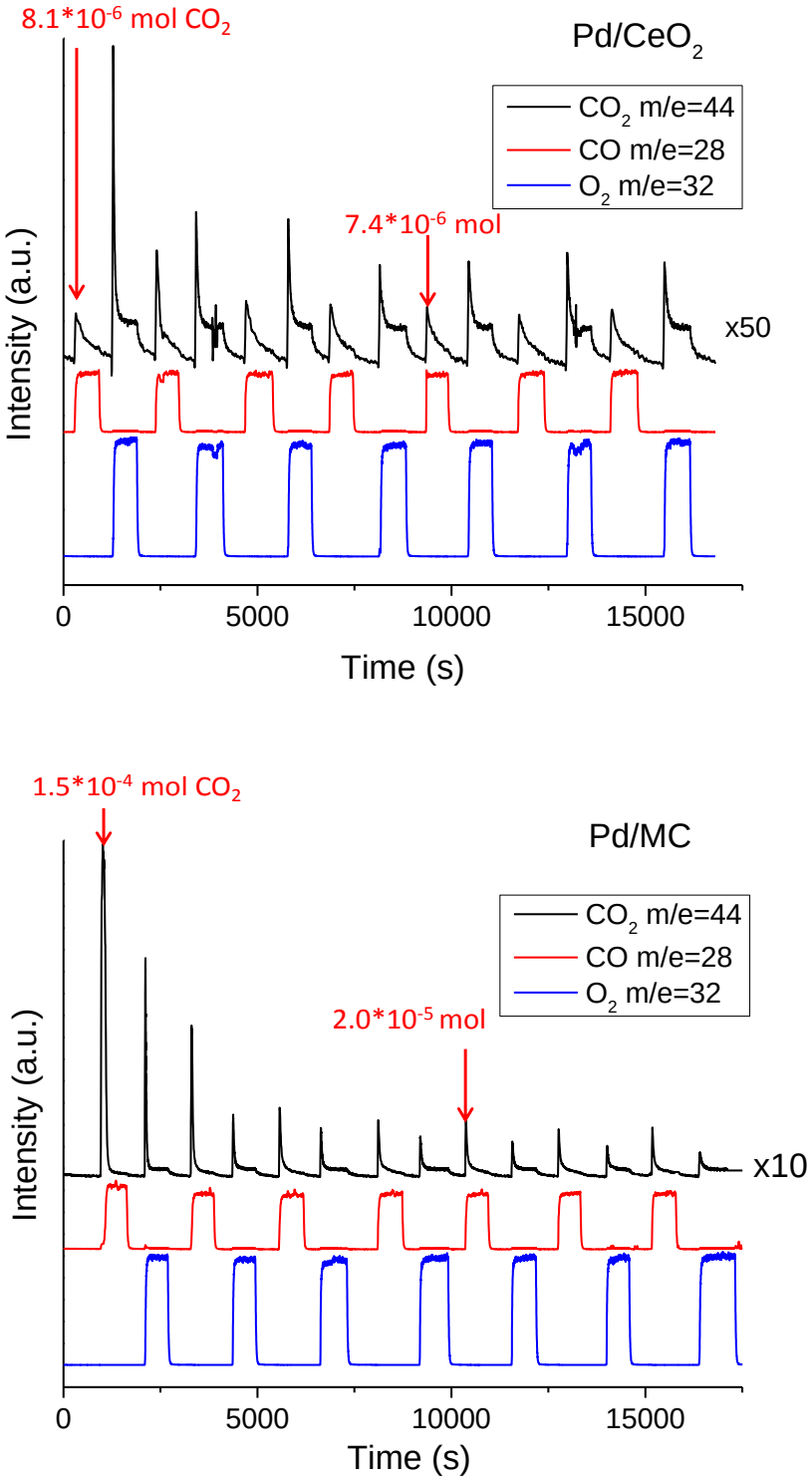

Figure 3.15 CO/O_2 transient reaction profile of 1 wt % Pd/CeO_2 and Pd/MC. Evolution of CO_2, O_2, CO signals were monitored as a function of time.

the support must be involved in the reduction. On the other hand, a much smaller amount of CO_2 ($8.1*10^{-6}$ mol) is produced over Pd/CeO_2, suggesting that the lattice oxygen is less likely to react with CO at low temperatures. Upon exposure to O_2, CO_2 is produced more due to the decomposition of carbonate species on the support and reaction of chemisorbed CO on Pd [131-132]. After four pulse cycles of CO and O_2 injection, CO_2 production stabilizes at around $2.0*10^{-5}$ mol and $7.4*10^{-6}$ mol for Pd/MC and Pd/CeO_2, respectively. The ratio of the steady state CO_2 production (2.7) of Pd/MC and Pd/CeO_2 at 50^oC in the CO/O_2 transient pulse experiments is consistent with one (2.5) in the CO oxidation experiments. This suggests that CO adsorption is not the rate limiting step for CO oxidation. The low CO_2 production on Pd/CeO_2 implies that Pd/MC can release lattice oxygen easier than Pd/CeO_2. The decrease in steady state CO_2 production of Pd/CeO_2 and Pd/MC might be due to the limited oxygen transfer rate or accumulation of different carbonate species on the surface that partially block adsorption of O_2 [133]

Ce^{3+}/Ce_{total} ratio sometimes are used to reflect catalysts redox property. Higher Ce^{3+} amount may lead to higher oxygen storage and release capacity [81-93]. Here Ce 3d XPS spectra of Pd/CeO_2 and Pd/MC are fitted to calculate Ce^{3+} amount in the catalyst surface regime, shown in figure 3.16**.** The Ce^{3+}/Ce_{total} ratio of Pd/CeO_2 is 20.4%, while for Pd/MC, the number is only 7%. The Ce^{3+} amount and actual redox capacity looks contradictory to the trend. Recent study shows that directly compare Ce^{3+} amount of fresh sample is not accurate to relate with OSC of Ce sample. Researchers demonstrated that active Ce^{3+} species in a ceria-supported platinum catalyst during CO oxidation are short-lived and therefore cannot be observed under steady-state conditions[134]. Using time-resolved resonant X-ray emission spectroscopy, they could quantitatively correlate the

initial rate of Ce^{3+} formation under transient conditions to the overall rate of CO oxidation under steady-state conditions and showed that ceria reduction is a kinetically relevant step in CO oxidation, whereas a fraction of Ce^{3+} was present as spectators. In addition, introducing Mn into CeO_2 lattice probably improve the redox activity of surface Ce species and lead to higher reaction rate. Hence, it is not necessary to compare Ce^{3+}amount to determine catalysts redox activity and OSC. More reasonable way is to determine the redox rate during reaction.

3.3.6 Effect of reaction time and Pd loading on CO conversion

Figure 3.17 illustrates the CO conversion as function of time at room temperature over the Pd/MC catalyst. In this experiment, the furnace was kept off and the initial catalyst bed temperature is room temperature (ca. 25^{o}C). Once introduced CO, the catalyst bed temperature increased to ca. 50^{o}C due to exothermal reaction. Clearly, the CO conversion (ca. 95%) over the Pd/MC catalyst remained unchanged even after 8 h time-on-stream. In addition, the catalyst bed temperature maintains the same at 50^{o}C as well. That is, CO in feed gas was completely oxidized into CO_2 over the Pd/MC catalyst. From the previous in-situ XANES, XPS after XAS experiments and CO/O_2 pulse results, it is known that the activity comes from the excellent oxygen transfer interaction between Pd and the MC support, meanwhile without Pd oxidation state change. This long time experiment further suggests that such interaction is sustainable. The redox features of the Pd/MC catalysts are quite stable under the CO oxidation atmosphere at low temperature.

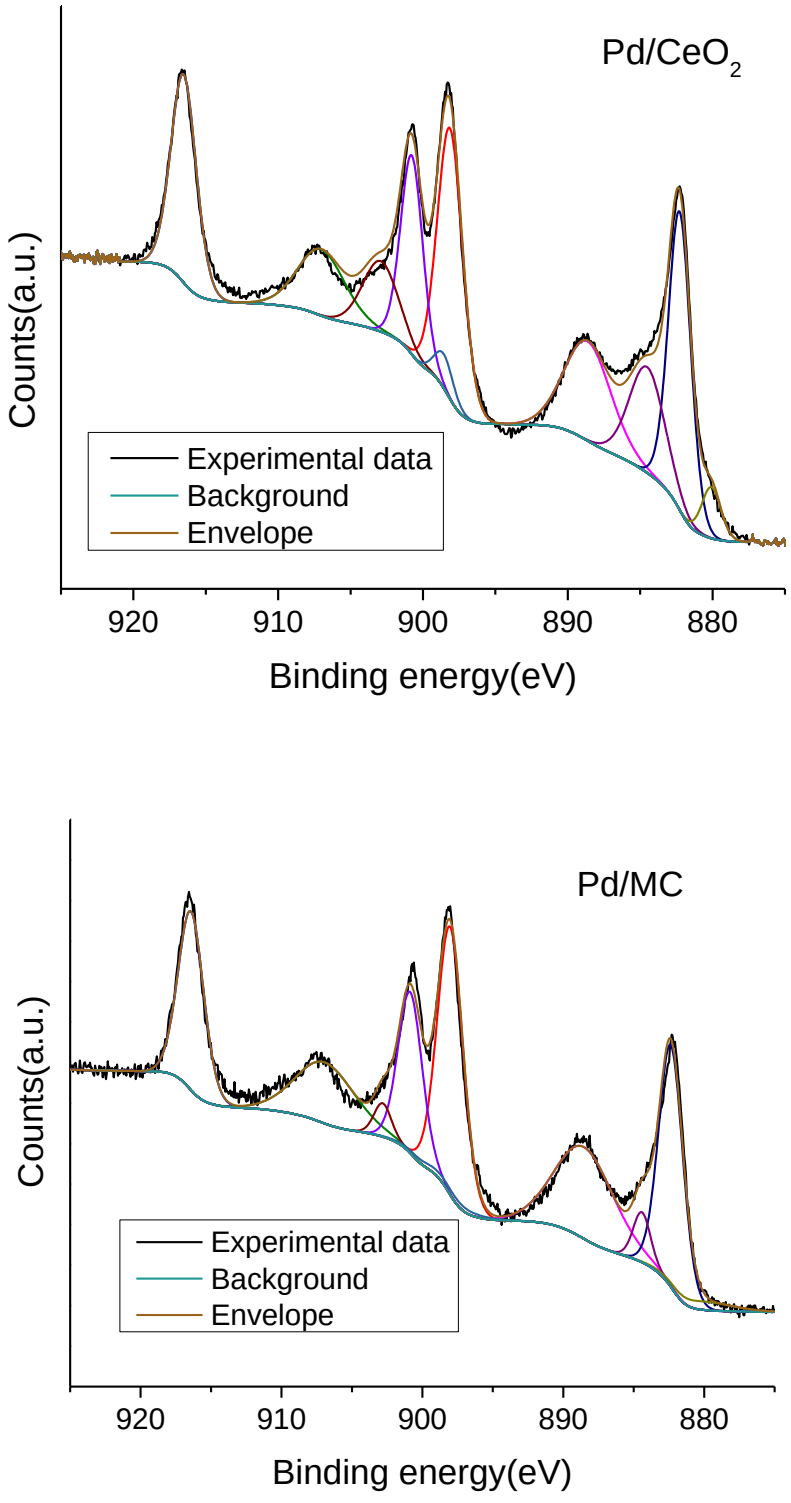

Figure 3.16 Ce 3d core-level XPS of the calcined Pd catalysts

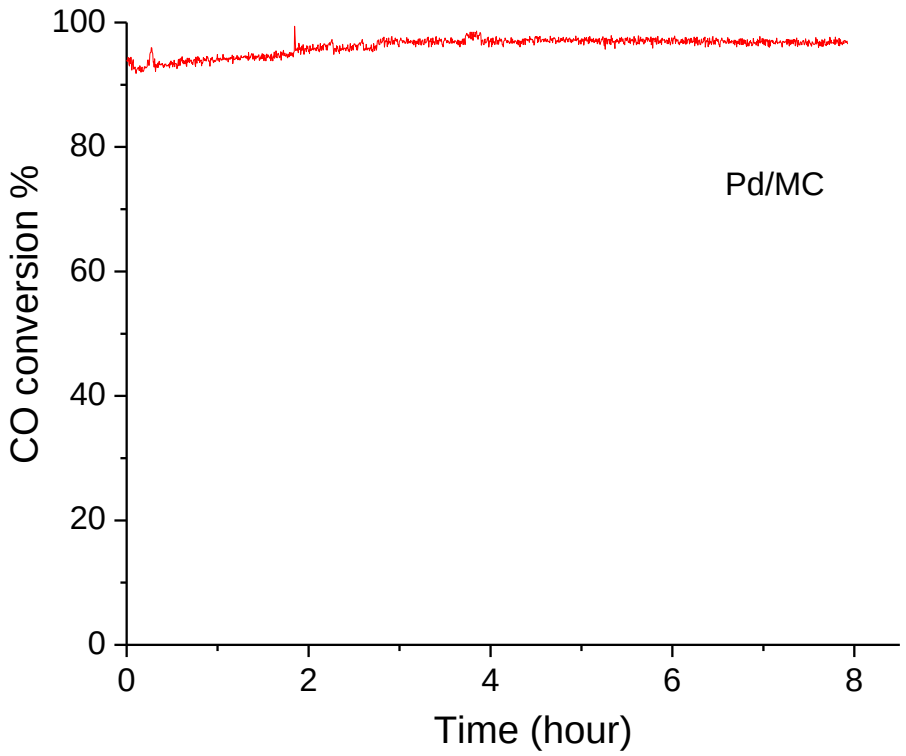

Figure 3.17 Effect of reaction time on CO conversion of Pd/MC without heating by furnace.

From the economical point of view, if catalyst can maintain the same activity with the less Pd loading, it will have much lower price since Pd is an expensive material. To evaluate the Pd loading effect, 0.2 wt% and 0.5 wt% Pd/MC sample were prepared using the same method as 1wt% sample. The effect of Pd loading on activity of 0.2%, 0.5% and 1% Pd/MC catalysts was investigated at a temperature range of 50–450 ℃ (figure 3.18). Decreasing the Pd loading to 0.5% shows similar activity as the 1% sample. Only a slight decrease at 50^{o}C is observed. However, further reducing the Pd loading to 0.2 % can cause significant activity drop from 95% to 70%. The TOF at 50^{o}C of the 0.2% sample is 0.252 s^{-1}, which is 3.5 times higher than the 1% Pd/MC sample. Since not all CO fully

converted to CO_2, this TOF can reflect the maximum activity of each Pd site at certain temperature. TOF of 0.2% Pd/MC is ca.8 times higher than the TOF of 1% Pd/CeO_2. This comparison is more accurate to reflect the activity of Pd site because both catalysts show less than 100% CO conversion and each Pd site is fully used. Such results further indicate that Pd on MC is much more active than the Pd on CeO_2. Comparing with the Pd-Ce catalysts reported in other references, the 0.2% Pd loading on MC still shows higher TOF and CO conversion to those catalysts have even higher Pd loading[94-99]. This indicates that Pd/MC has good potential to lower the cost of CO oxidation catalyst, meanwhile keeps the high activity.

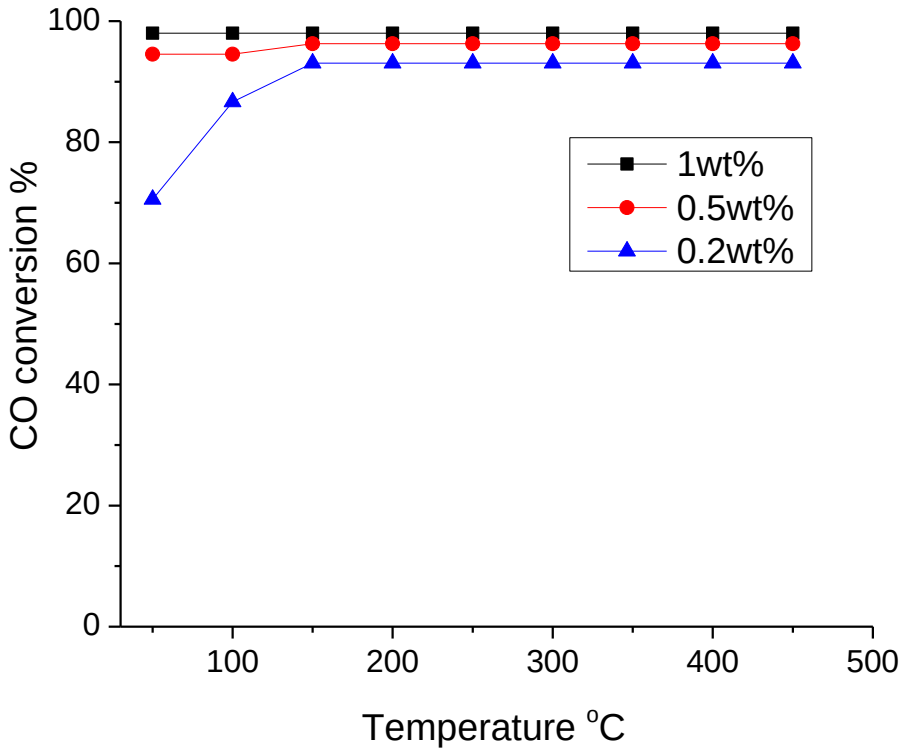

Figure 3.18 Pd loading effect on CO conversion. CO/O_2 ratio of 2:5 and GHSV = 40,000 h^{-1}.

3.4 Conclusion

In this work, the high activity of Pd/MC for low temperature CO oxidation is investigated through a series of characterization experiments. Our results indicate that highly dispersed PdO species can form on freshly calcined CeO_2 and MC supports. In-situ XAS experiments reveal that Pd^{2+} species are reduced to Pd^0 on CeO_2 during CO oxidation, while Pd maintains its initial oxidation state on MC. The presence of stable Pd^{2+} species on MC shows that Pd is re-oxidized by the lattice oxygen of MC.

Participation of lattice oxygen in the low temperature CO oxidation is also supported by the H_2-TPR and CO/O_2 transient pulse experiments. Despite the similar H_2 reduction temperatures observed for both Pd/CeO_2 and Pd/MC, the higher amount of H_2 consumed on Pd/MC indicates that more lattice oxygen of MC can be extracted at lower temperatures. Similarly, CO/O_2 transient pulse experiments imply that Pd/MC shows higher reducibility at 50^oC in the presence of CO compared to one for Pd/CeO_2. Smaller amount of CO_2 produced on Pd/CeO_2 suggests that the lattice oxygen in the CeO_2 support is less likely to react with CO at 50^oC. In the case of Pd/MC, a higher amount of oxygen is replenished and transferred from the gas phase O_2, leading to high CO oxidation activity at low temperatures.

Pd/MC redox ability is stable under long time reaction and shows high activity. Lowering the Pd loading to 0.5wt% does not affect activity, but further deceasing the loading to 0.2wt% reduce the CO conversion to 70% at 50^oC.

Chapter 4

Evaluation of Mn and Sn modified Pd-Ce based catalysts for low-temperature diesel exhaust oxidation

4.1 Introduction

Diesel oxidation catalysts (DOCs) have been widely applied for the remediation of toxic pollutants, i.e., CO, hydrocarbons (HCs) SO_2, and NOx, from diesel-powered vehicles [135-136]. In previous chapter, the incorporation of Mn into the CeO_2 lattice improves the OSC and lattice oxygen reducibility of CeO_2, in which Pd/MnO_x-CeO_x (Pd/MC) catalyst showed high activity for CO oxidation at ambient temperature. It was reported that doping MC solid solution with low amount of Sn (<0.05% atomic) enhanced reducibility of the catalyst and prevented the growth of doped-ceria crystal grains leading to a better OSC and CO oxidation activity in comparison to pure ceria [137]. Another reference suggests that the SnO_2-MnO_x-CeO_x (SMC) catalyst indicated a better SO_2 tolerance in the NH_3-SCR, and while still maintaining high NO conversion at low temperature [137].

For practical implementation of a cold start automobile exhaust catalyst, the catalyst preferably maintain its initial activity against severe operating conditions such as changing exhaust temperature, steam, high and low space velocities, and traces of SO_2 [138-140]. However, the effects of these conditions are rarely reported over the Pd/CeO_2

based catalysts that often synthesized via aforementioned complex procedures [94-99,108]. Hence, catalysts having excellent LTA for CO oxidation at room temperature and stability under severe conditions need to be developed using simpler, scalable and more economical synthesis techniques considering the ultimate practical application.

In this work, a new Pd/SnO_2-MnO_x-CeO_x (Pd/SMC) was synthesized. Then the activity of Pd/CeO_2, Pd/MC and Pd/SMC catalysts were evaluated for CO and hydrocarbon oxidation under simulated diesel exhaust gas conditions. Catalyst performance tests were conducted following the low temperature diesel combustion (LTC-D) protocol [141]. The interaction of CO and C_3H_6 with the surface active sites was investigated using in-situ diffuse reflectance infrared Fourier transform spectroscopy (DRIFTs). The evaluation and characterization results were combined to explain HC deactivation over Pd/Ce based catalysts. At last the CO oxidation activity of Pd/SMC and Pd/MC are compared under SO_2 poisoning condition.

4.2 Experimental

4.2.1 Catalysts preparation

The SMC supports were prepared by an ultrasonic assisted co-precipitation method, where $SnCl_2$, $Mn(NO_3)_2$, and $Ce(NO_3)_3$, with a mole ratio of 1:4:5, were used as the catalyst precursors and $(NH_4)_2CO_3$ (1 mol L^{-1}) as a precipitator. The paste obtained from co-precipitation was treated by ultrasound for 2 h, followed by subsequent filtration, washing with deionized water, drying in air overnight at 105^oC, and calcination in air at 500^oC for 6 h. The Pd/SMC with 1 wt% Pd loading was synthesized by impregnation. The SMC support was immersed into the aqueous $Pd(NO_3)_2$ solution and dried at room temperature while stirring. Subsequently, the solid was calcined at 550^oC for 3 h in air.

Similarly, Pd/CeO_2 and Pd/MC (Mn:Ce ratio = 1:1) were synthesized by the same co-precipitation and Pd impregnation methods. The actual Pd loading over the Pd/SMC, Pd/MC, and Pd/CeO_2 catalysts were measured using atomic absorption spectroscopy and were found to be 1.0 ±0.05 wt%, 1.1 ±0.05 wt% and 1.0 ±0.05 wt %, respectively.

4.2.2 Activity tests under simulated diesel exhaust

The low temperature diesel combustion (LTC-D) evaluation protocol was used as specified in the "After treatment Protocols for Catalyst Characterization and Performance Evaluation: Low-Temperature Oxidation Catalyst Test Protocol" published by the Advanced Combustion and Emission Control (ACEC) Technical Team: Low-Temperature After treatment Group. Unless otherwise specified, catalyst amounts and gas flow rates were normalized to give a space velocity of 200 L g^{-1} hr^{-1}. Typically, this amounted to 100 mg of sample and a flow rate of ~333 sccm. Before activity was measured, catalysts were degreened once at 700 ℃ for 4 h and then pretreated before each evaluation at 600 ℃ for 20 min in $[H_2O]$ = 6%, $[CO_2]$ = 6%, and $[O_2]$ = 12% balanced with Ar. Activity was then measured as a function of temperature at a rate of 2 ℃/min to a maximum temperature of 500 ℃. This consisted of a mixture of $[O_2]$ = 12%, $[H_2O]$ = 6%, $[CO_2]$ = 6%, $[H_2]$ = 400 ppm, [NO] = 100 ppm, [CO] = 2000 ppm, $[C_2H_4]$ = 833.5 ppm, [C3H6] = 333.3 ppm, $[C_3H_8]$ = 111 ppm, and balanced with Ar. Water was introduced into the system by bubbling Ar gas through water heated at 50 ℃ and delivered via heated gas lines maintained at 150 ℃. Oxidation activities were measured using a gas chromatography (Agilent 490 Micro GC). The conversion is calculated using the following expression: (X/Cmax)*100 where X is the ppm obtained from GC

integration of the given reactant peak and Cmax is the calibration ppm obtained from the GC during bypass measurement.

In addition to the LTC-D evaluation, CO and C_3H_6 oxidation were conducted in a plug flow rector under atmospheric pressure and CO conversion was measured by a differentially pumped mass spectrometer (MS, Hiden HAL IV RC). A gas mixture of 2.0% CO (99.999% CO, Airgas), 1000 ppm C_3H_6 (1% C_3H_6 in He, Praxair), 5% O_2 (99.9999% O_2, Airgas) and balance Ar (99.9999% Ar, Airgas) was fed to the reactor via mass flow controllers (Brooks 5850E). 200 mg of catalyst supported with quartz wool was placed in the reactor for each run and no pretreatment was performed before the reaction. The gas hourly space velocity (GHSV) for all experiments was 40,000 h^{-1}. Less than ±5% conversion error is calculated by reparative tests.

The SO_2 poisoning experiments are conducted with a gas mixture of 2.0% CO, 5% O2 200 ppm SO_2 (2% SO_2 in N_2) and balance Ar. 500 mg of catalyst supported with quartz wool was placed in the reactor for each run and no pretreatment was performed before the reaction. The gas hourly space velocity (GHSV) for all experiments was 40,000 h^{-1}.

4.2.3 Catalyst characterization

Powder X-ray diffraction (XRD) data for fresh samples were collected on a RigakuMiniflex II desktop diffractometer using a Cu Kα source with D/teX Ultra 250 silicon strip detector. XRD for degreening comparisons were taken on a Panalytical Empyrean XRD operated at 40kV and 40mA using a Cu Kα source. X-ray photoelectron spectroscopy (XPS) experiments were carried out on a Kratos AxidUltra DLD XPS

system equipped with a hemispherical energy analyzer. A monochromatic Al Kα X-ray source (1486.6 eV) was operated at 15 kV and 120 W. Adventitious carbon at 284.8 eV (C1s) was used as a reference of binding energy. The high-resolution elemental mapping and imaging of particles were collected using a FEI Talos F200X scanning transmission electron microscope (STEM). The surface area of samples were measured on a Micromeritics ASAP 2020 instrument by the N_2 adsorption at 77 K and calculated by the Brunauer−Emmett−Teller (BET) method. The surface area for CeO_2, MC, SMC are 60, 62 and 82 m^2/g, respectively.

DRIFTs experiments were performed using a Bruker Equinox 55 spectrometer equipped with a deuterated triglycine sulfate (DTGS) detector. Oxidation reactions at 100^{o}C over these catalysts were studied with an accumulation of 64 scans at a resolution of 2 cm^{-1}. The catalysts were pretreated at 400^{o}C in the DRIFTS cell for 30 min in 10% O_2/Ar. Subsequently, the system was cooled down to 100^{o}C and a background was recorded. CO and C_3H_6 oxidation studies over the catalysts were carried out in the following sequence: 1) CO+O_2 for 30 min, 2) C_3H_6+CO+O_2 for at least 10 min, 3) CO+O_2 for 10 min. Inlet gas concentrations are 0.6% CO, 10% O_2, 0.1% C_3H_6 (when used) with Ar balance.

4.3 Results and discussion

4.3.1 Catalyst structure

The XRD profiles of the Pd impregnated ceria based catalysts are shown in figure 4.1. The diffraction peaks observed over Pd/CeO_2 and Pd/MC can be attributed to the (111), (200), (220) and (311) lattice planes of the cubic fluorite structure of CeO_2,

indicating that Mn and Ce formed a solid solution without appreciable phase separation [11]. The diffraction peaks corresponding to Pd metal (40.2^o) or PdO (34^o, 42^o) are not observed in any catalysts, which can be attributed to the small Pd loading or formation of highly dispersed Pd species [25,100-101]. In the case of Pd/SMC, two additional diffraction peaks at 38^o and 52^o can be assigned to SnO_2 [142], indicating that SnO_2 segregates from the SMC solid solution. Based on (111) diffraction peak, crystallite size of CeO_2, MC, SMC support are 9.6nm, 3.17nm and 3.29nm, respectively.

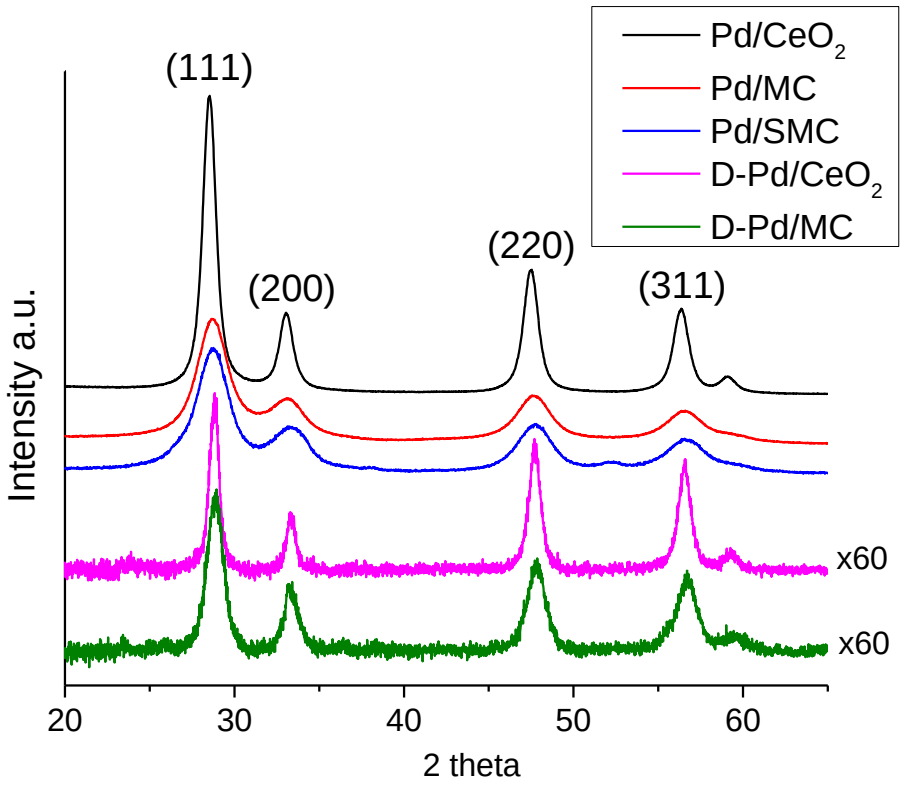

Figure 4.1 Wide-angle XRD profiles of the fresh supported Pd catalysts and degreened Pd/CeO_2 (D-Pd/CeO_2) and Pd/MC (D-Pd/MC).

During the LTC-D evaluation protocol, the catalysts were degreened at 700^{o}C for 4 h, which is higher than the calcination temperature (550^{o}C) of the solid solution

catalysts. Possible phase separation of the degreened Pd/CeO_2 and Pd/MC samples was investigated via XRD. As shown in figure 4.1, the diffraction profiles of the fresh and degreened samples are similar to each other and no additional diffraction peaks for Pd, PdO and MnO_x were observed after degreening.

The morphology and elemental distribution of Ce, Mn, and Pd for the 1wt% Pd/MC catalyst before and after degreening are shown in figure 4.2. The fresh sample comprises nanoparticles with spherical or elliptical shapes and sizes in the range of 20 and 40 nm. The EDX analysis of the fresh Pd/MC sample indicates that both Mn and Ce are uniformly distributed within the sample structure, confirming the formation of a Mn-Ce solid solution. Pd mapping clearly shows that the majority of the Pd is highly dispersed on the MC support. One small area of aggregated Pd can be seen at the center of the mapping. After degreening at 700^{o}C, the sample shows a similar morphology of nanoparticles as the fresh sample. However, Mn and Ce are not uniformly distributed and some areas of Mn separate from the surrounding Ce. Additionally, Pd is not dispersed as well as in the fresh sample and more areas of Pd aggregates can be observed. The STEM-EDX analysis confirms that both Mn segregation from the Mn-Ce solid solution and Pd aggregation occur after degreening. The lack of MnO_x and PdO diffraction peaks for the degreened sample in the XRD might be due the low concentration of Pd and low concentration of separated MnO_x crystals. Higher magnification of fresh Pd/MC STEM-mapping is shown in chapter 3.

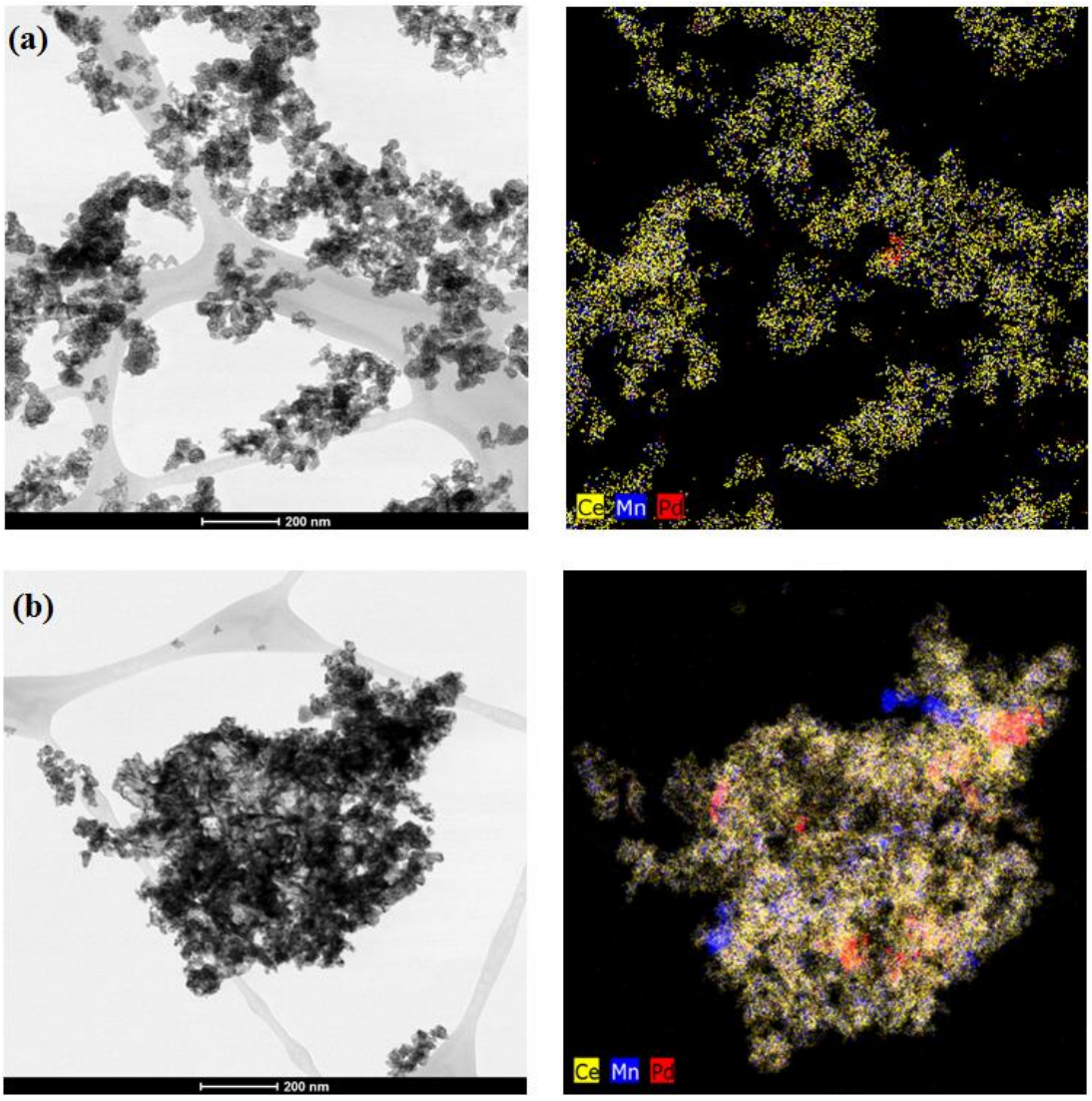

Figure 4.2 STEM images and EDX maps of 1 wt% Pd/MC before (a) and after (b) degreening. The STEM mapping was conducted by Dr. Michael J. Lance.

In the case of Pd/SMC, XPS was conducted to characterize the oxidation state of surface Pd species. As shown in figure 4.3, only one peak at 337.7 eV with a FWHM of 1.46 eV is present, while the lower binding energy peak at 336.5 eV, corresponding to the crystalline PdO phase, is not observed. The formation of high binding energy peak of Pd^{2+} might be due to the SMSI and can be attributed to the formation of small PdO

clusters or palladium ceria interaction phase, $Ce_{1-x}Pd_xO_{2-\delta}$ [86,87, 111-112], which is similar to the Pd/MC sample.

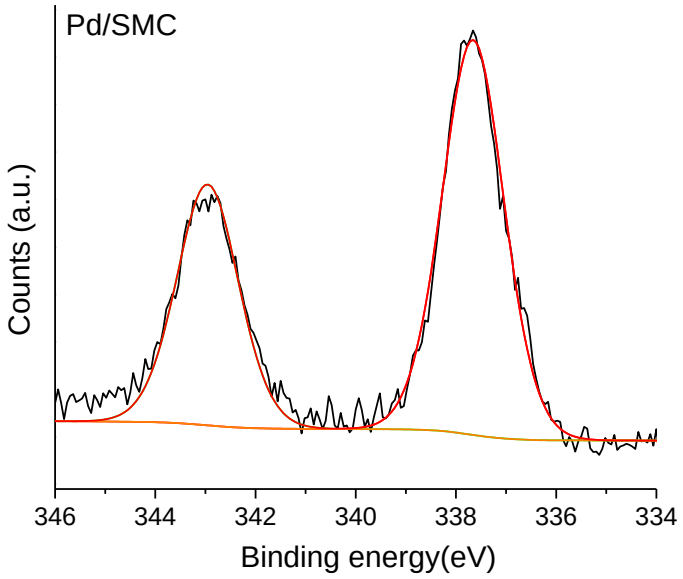

Figure 4.3 Pd 3d core-level XPS spectra of fresh Pd/SMC catalyst.

4.3.2 Activity of Pd catalysts under diesel exhausts condition

The performance of the Pd supported catalysts was evaluated under the LTC-D protocol and conversions for CO and HCs are shown as a function of temperature in figure 4.4. For comparison, the light-off temperatures for CO and HCs at 50% conversion (T_{50}) and 90% conversion (T_{90}) are depicted in figure 4.5. Among the Pd supported catalysts, Pd/MC shows the lowest T_{50} of $173 \pm 4^{o}C$ for CO oxidation. Both Pd/CeO_2 and Pd/SMC indicate a similar T_{50} for CO oxidation at $187 \pm 4^{o}C$ and $191 \pm 4^{o}C$, respectively. The CO light-off curves for Pd/MC and Pd/SMC show a sigmoid shape with higher conversions than Pd/CeO_2 at temperatures below T_{50}, and spread over a wider

temperature range to reach T_{90}. The total hydrocarbon (THC) conversion includes the conversion of the sum of C_2H_4, C_3H_6 and C_3H_8 on a C_1 basis. Unlike the T_{50} of CO, Pd/CeO_2 has the lowest T_{50} (267 ± 7^oC) for THC, which is 20^oC and 70^oC lower than T_{50} of Pd/MC and Pd/SMC, respectively. The shape of the light-off curves for all three hydrocarbons over Pd/MC and Pd/SMC look similar to that of CO. Oxidation of C_2H_4 and C_3H_8 starts at lower temperatures over Pd/MC and Pd/SMC than Pd/CeO_2, yet increases slower with increasing temperature, leading to a higher T_{50} and T_{90}. For C_3H_6 oxidation, the conversion starts at similar temperatures for all three Pd catalysts, and both Pd/MC and Pd/CeO_2 demonstrate a T_{50} of 214^oC, which is lower than that of Pd/SMC of 246^oC. However, the slope of the C_3H_6 light-off curve for Pd/CeO_2 above T_{50} is higher than the other two catalysts leading to the lowest T_{90} of 236^oC.

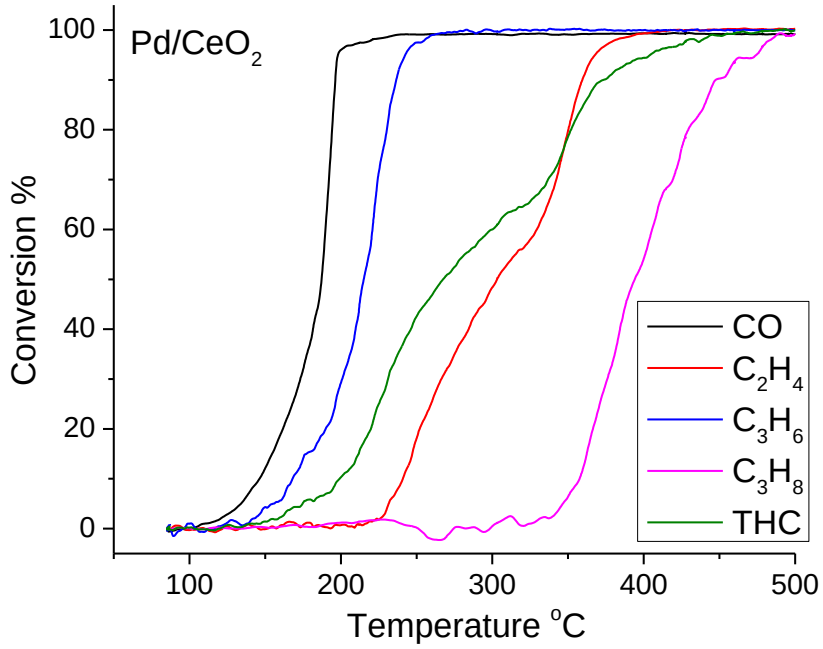

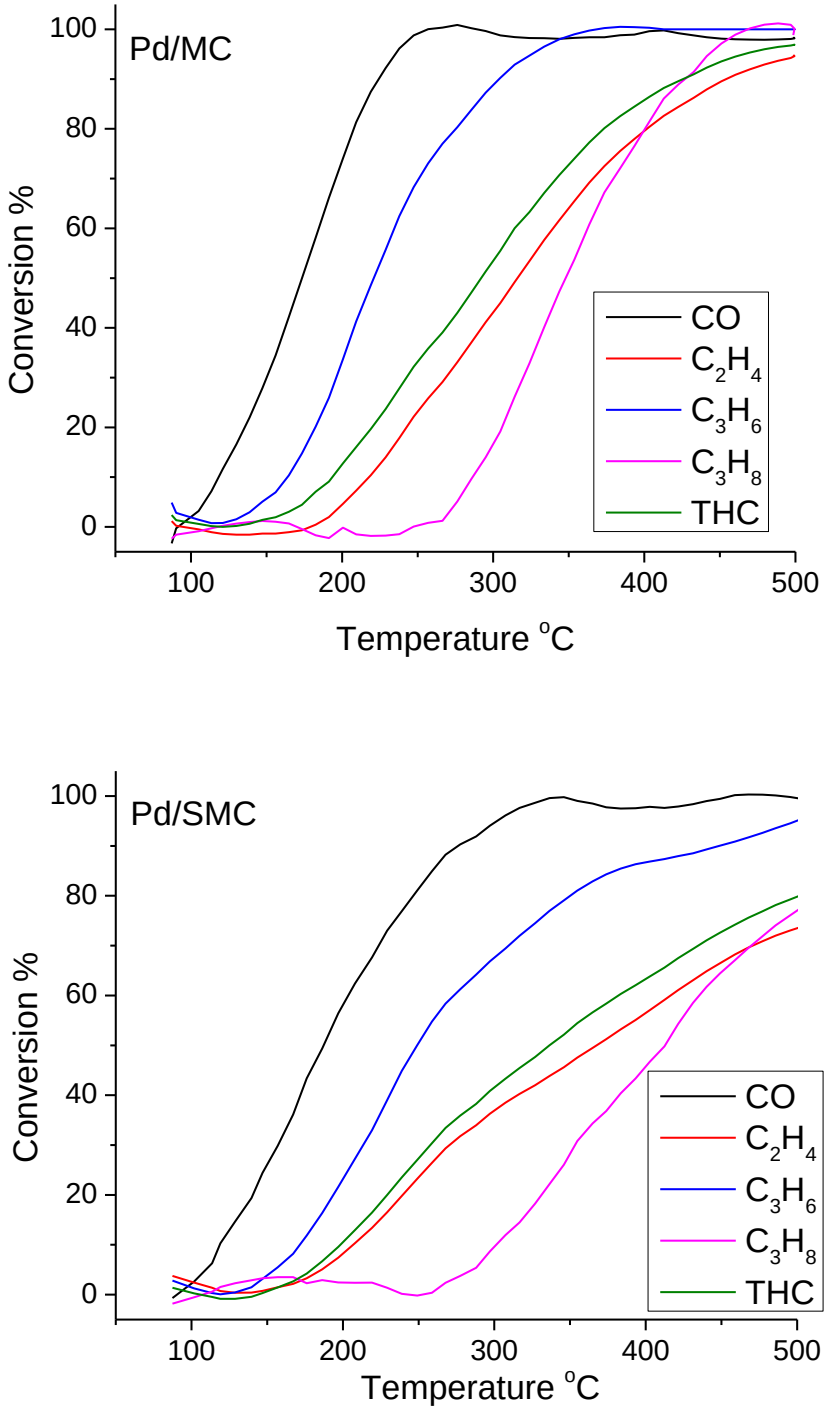

Figure 4.4 Catalytic performance of the degreened Pd/CeO_2, Pd/MC, and Pd/SMC catalysts under simulated diesel exhaust oxidation. The tests were conducted by Dr. Andrew Binder and Dr. Todd Toops.

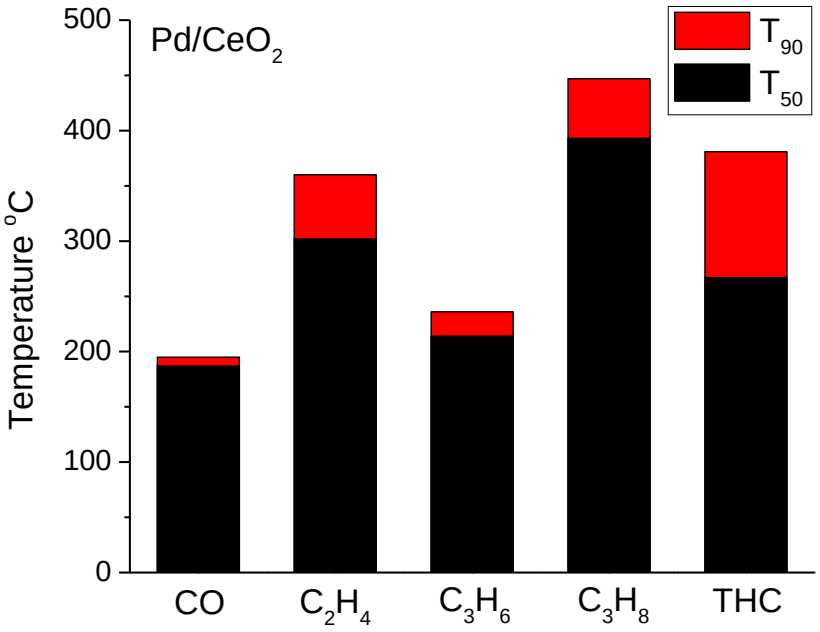

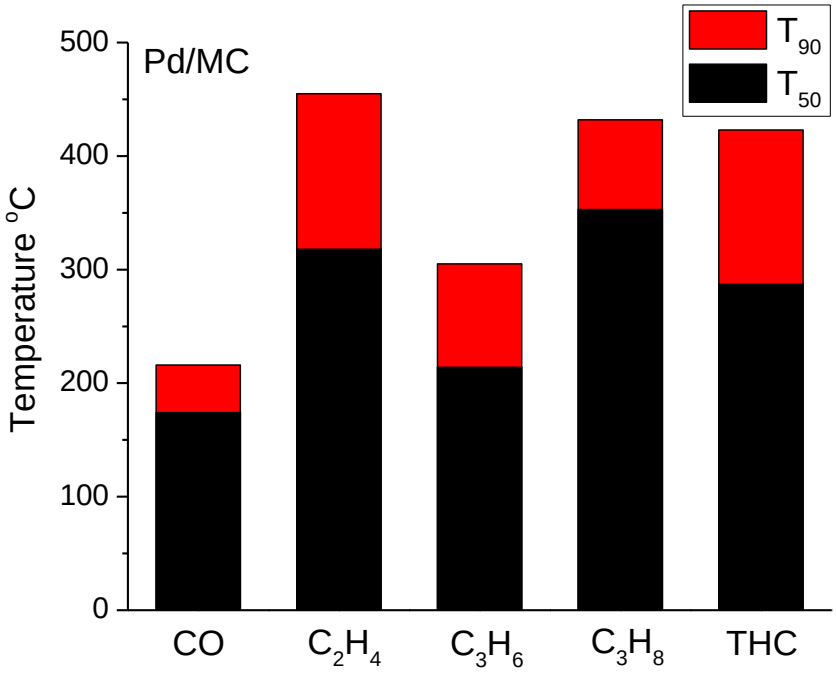

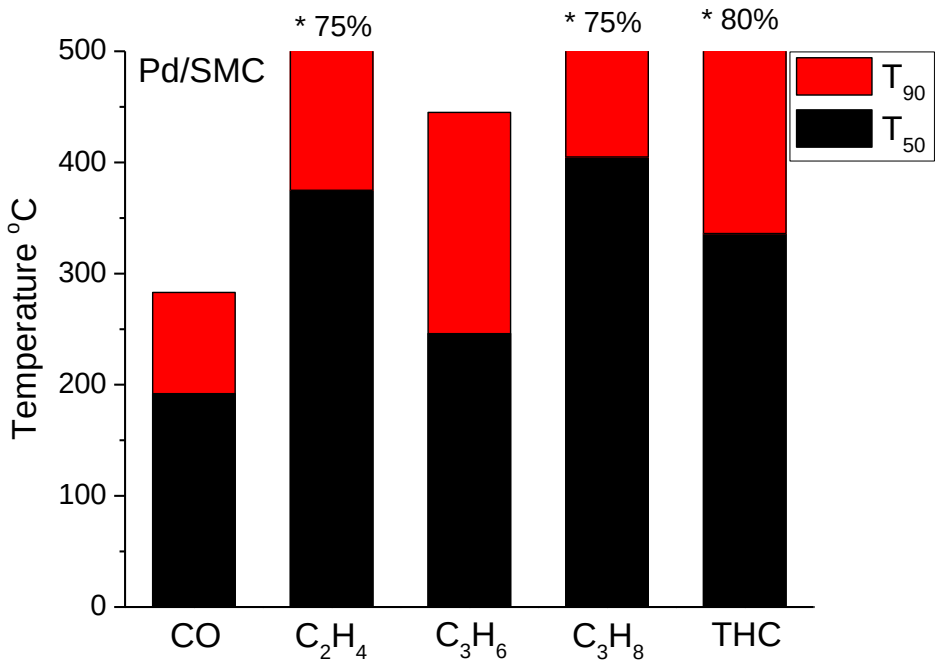

Figure 4.5 T_{50} and T_{90} of Pd catalysts for CO and HC conversion. * represents the maximum conversion if it is under 90%.

The presence of CO, NO, and HCs can inhibit their oxidation at low temperatures [2, 143]. Initially, CO can strongly adsorb onto active sites at low temperatures in the presence of NO and HCs, covering the majority of the catalyst surface. In this case, oxygen access to the catalytic sites is limited, resulting in a low CO oxidation rate [2]. Generally, the presence of HCs can limit CO oxidation, as both CO and HCs compete for the same Pd active sites. Light alkenes (i.e., C_2H_4, C_3H_6) can strongly adsorb onto active Pd sites, due to their double bonds [144]. When the temperature allows CO oxidation to start, CO_2 forms and desorbs from the surface, opening up active sites for CO and alkenes to competitively adsorb [2]. This competition limits CO access to the active sites and thus its subsequent oxidation. At certain temperatures, alkenes also start to react with oxygen

and their oxidation products desorb from the active sites [2,143]. In addition to the alkenes, NO can dissociatively adsorb on the active sites, competing with the adsorption of CO and HCs and inhibiting their oxidation [143, 145].

It was reported recently that crystalline PdO phase has higher activity in hydrocarbon oxidation than highly dispersed Pd^{2+} due to easier decomposition of intermediate, but highly dispersed Pd^{2+} and lattice oxygen mobility of support are important for CO oxidation[146]. Both MC and SMC supports demonstrate higher activity at under 170^{o}C. This is because Pd/MC has more highly dispersed Pd^{2+} and better lattice oxygen reducibility. It is likely that at higher temperatures, competitive adsorption of CO and HCs becomes the limiting factor for CO conversion [42].At higher temperature above 170^{o}C, which reaches onset of C_3H_6 oxidation temperature, since Pd/MC has less crystalline PdO phase, C_3H_6 oxidation activity is lower than Pd/CeO_2 and the slop of light-off curve increase slower. The C_3H_6 inhibition is more severe on Pd/MC and cannot immediately free many sites for CO oxidation, so that at higher temperature the CO conversion increases slower than Pd/CeO_2.

4.3.3. Effect of C_3H_6 to CO oxidation

In order to get further insight into the hydrocarbon inhibition, propylene was chosen as a probe molecule to evaluate the change in the light-off curve of CO and surface active sites. CO oxidation was carried out over Pd/CeO_2 and Pd/MC with and without the presence of C_3H_6 and the light-off curves are shown in figure 4.6. Pd/CeO_2 shows almost 100% CO conversion at 100^{o}C under $CO+O_2$, but drops below 40% CO conversion at 50^{o}C, while Pd/MC still achieves almost 100% CO conversion at 50^{o}C [25]. Upon introduction of 1000 ppm C_3H_6, the CO oxidation activity for both catalysts

drops significantly and both Pd/CeO_2 and Pd/MC show CO conversions below 10% at 50°C. As the catalyst temperature increases to 150°C, both catalysts can achieve over 95% conversion for CO and C_3H_6. The oxidation of C_3H_6 and CO show similar light-off curves, indicating that both molecules are attracted by the same active sites. The similar activity profiles observed over Pd/CeO_2 and Pd/MC indicate that modification of OSC of supports has little effect on CO oxidation in the presence of C_3H_6 [17,146]. In comparison to the light-off curves shown in figure 4.4, both CO and C_3H_6 oxidize at lower temperatures suggesting that competitive adsorption of C_2H_4 and NO has an influence on the oxidation profiles [143]. In addition, segregation of Mn-Ce solid solution or sintering of Pd can also contribute to the low activity at low temperature after degreening [35, 38-40].

To have a straightforward view of C_3H_6 inhibition effect, MS signals of CO, C_3H_6, O_2 and CO_2 are shown in figure 4.7 during temperature ramp from 100°C to 150°C for the Pd/MC sample. This temperature ramp process depicts the transient reaction state of the CO and C_3H_6 oxidation. Conversion for both CO and C_3H_6 is less than 10% at 100°C but over 95% at 150°C. In the MS, both CO and C_3H_6 show high signal intensity at 100°C. Once the temperature ramps up, both signal start to drop down until they reach to near 0 intensity. On the other hand, O_2 and CO_2 signal show a very significant peak during the ramp. This indicates there is extra carbon source that has been accumulated on the catalyst surface at 100°C. Based on previous discussion, this peak can be attributed to oxidation of adsorbed C_3H_6 that accumulated on the active site. There might be has some adsorbed CO exist on the catalyst as well at 100°C, which is shown from later DRIFTs results in figure 4.10.

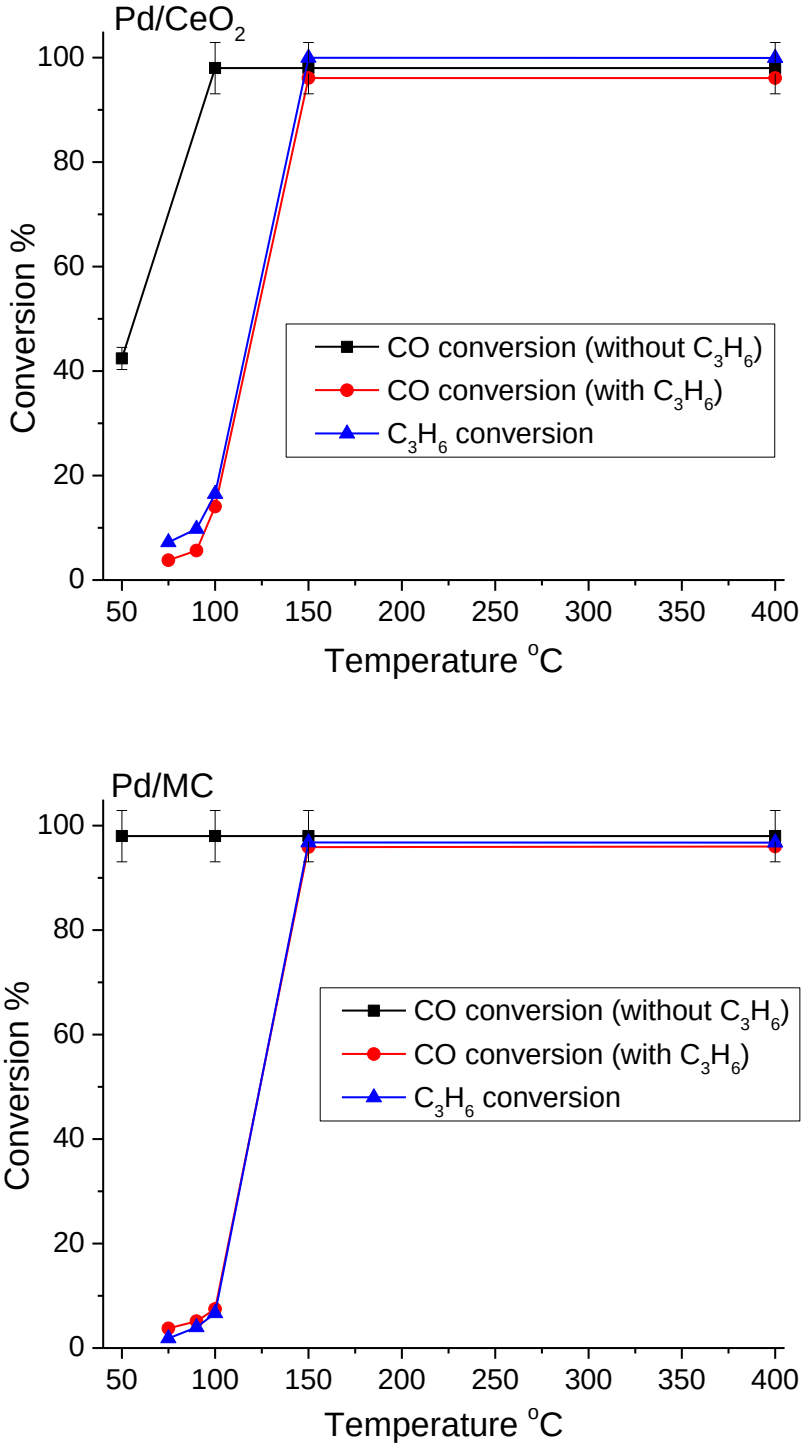

Figure 4.6 CO and C_3H_6 oxidation activity of 1wt% Pd/CeO_2 and Pd/MC catalysts. 2% CO, 1000ppm C_3H_6 (when used), 5% O_2 and GHSV = 40,000 h^{-1}.

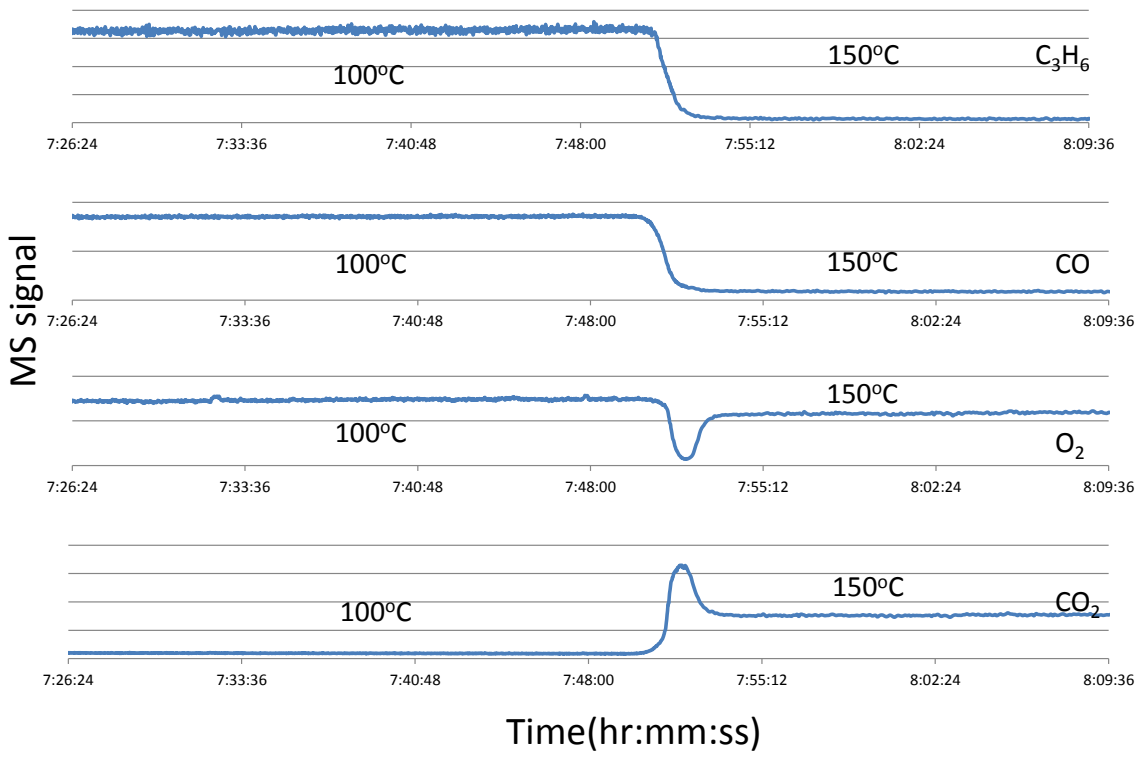

Figure 4.7 Oxidation of accumulated C_3H_6 on Pd/MC surface during temperature ramp from 100°C to 150°C. 2% CO, 1000ppm C_3H_6, 5% O_2 and GHSV = 40,000 h^{-1}.

It was widely reported that the pretreatment has a significant effects on Pd-based oxidation catalyst performance. In order to determine the degreen effect on catalyst activity, Pd/MC was treated under the same LTC-D degreen condition. The XPS of degreened Pd/MC also show the same spectra as fresh sample, shown in figure 4.8.

The catalytic activity of degeened sample was tested in the plug flow reactor again, shown in supporting information figure 4.9. Similar conversion is observed as the fresh Pd/MC under CO oxidation and CO+C_3H_6 oxidation. This suggests that the level of Mn separation and Pd sintering is not severe enough to deactivate the catalyst.

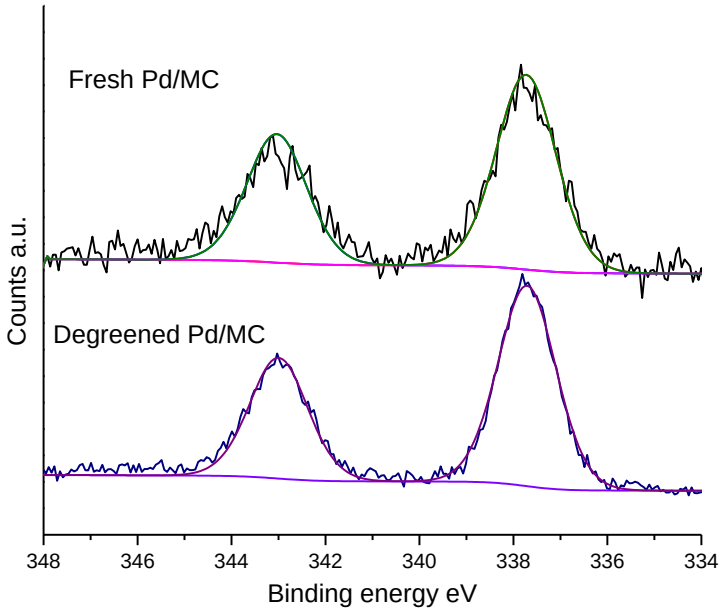

Figure 4.8 Pd 3d core-level XPS spectra of fresh and degreened Pd/MC

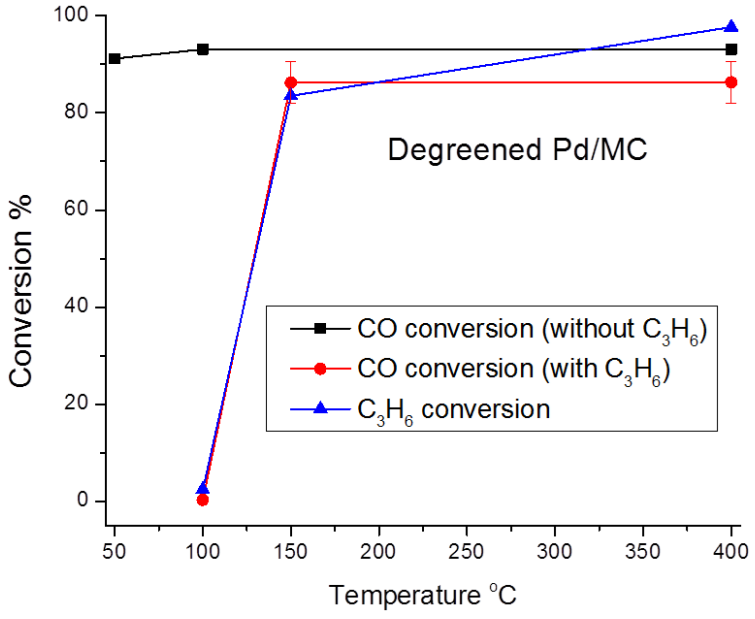

Figure 4.9 CO and C_3H_6 oxidation activity of degreened Pd/MC catalysts. 2% CO, 1000ppm C_3H_6 (when used), 5% O_2 and GHSV = 40,000 h^{-1}.

To determine the adsorption sites of CO and their evaluation in the presence of C_3H_6, in-situ DRIFTs was conducted over the Pd/CeO_2, Pd/MC, and Pd/SMC samples, shown in figure 4.10. The vibrational bands located in the range of 2110–1800 cm^{-1} can be attributed to the adsorbed CO on metallic palladium (Pd^0), while the vibrational bands located at a higher wavenumbers around 2150-2130cm^{-1} correspond to CO adsorbed on ionic Pd^{n+}. The vibrational bands at 2390-2290 cm^{-1} and 2220-2060 cm^{-1} are characteristic for gaseous CO_2 and CO, respectively [42]. The bands at 2943 and 2860 cm^{-1} can be assigned to the adsorption of bidentate formate species on Ce ions [39]. During CO oxidation, all three Pd catalysts show CO vibrational bands for CO-Pd^{n+} sites. Despite the overlap with the gaseous CO band, the vibrational bands for the adsorbed CO adsorbed on atop sites of Pd^0 at 2100-2090cm^{-1} can be detected on Pd/CeO_2 and Pd/SMC. No obvious vibrational bands for the atop CO-Pd^0 sites can be identified on Pd/MC. Chemisorbed CO on the bridge (1980–1860 cm^{-1}) and threefold hollow (1920–1800 cm^{-1}) sites of the Pd^0 are observed over Pd/CeO_2 [25,42]. However, no vibrational bands for bridge or hollow sites are detected on Pd/MC and Pd/SMC.

XPS analysis of the fresh samples indicates that Pd is fully oxidized on the surface with an oxidation state of 2+. During CO oxidation, some of the oxidized Pd species are reduced and Pd exists in a mixture of Pd^{n+}/Pd^0 on Pd/CeO_2 and Pd/SMC. For Pd/CeO_2, the appearance of CO adsorbed on Pd bridge sites might be due to the formation of larger metallic Pd particles with bridge sites or the lower re-oxidation ability of the CeO_2 support [26]. The lack of any adsorbed CO on Pd^0 sites over Pd/MC during CO oxidation can be attributed to superior oxygen storage and mobility of the MC support.

Upon introduction of C_3H_6, the Pd^{n+}–CO band disappears due to the competitive adsorption of C_3H_6 or reduction of Pd^{n+} to Pd^0 by C_3H_6 and its subsequent adsorption [30, 148]. Meanwhile, the gaseous CO_2 band intensity decreases and the C-H band in between 3000 and 2800 cm^{-1} grows. CO oxidation is inhibited by C_3H_6, caused by the competitive adsorption and blocking of the precious metal (Pd, Pt, etc.) active sites by C_3H_6 [143]. Because the oxidation of hydrocarbons occurs at higher temperatures than CO, the sites with adsorbed C_3H_6 block CO adsorption and oxidation until the C_3H_6 is itself oxidized [16].

Upon removal of C_3H_6 from the gas-phase, the Pd^{n+}-CO band recovers on Pd/CeO_2 and Pd/SMC, albeit to a lower intensity, implying that CO coverage decreases. The band also shifts from its initial position of 2143 cm^{-1} to 2136 cm^{-1}, which could indicate less weakly adsorbed CO. Meanwhile, the gaseous CO_2 band returns, also with a lower intensity compared to the spectra taken at initial $CO+O_2$. These results indicate that the activity for CO oxidation is not fully recovered over Pd/CeO_2 and Pd/SMC upon C_3H_6 removal, which is probably due to residual hydrocarbon species adsorbed on Pd^{n+} sites. In the case of Pd/MC, the Pd^{n+}-CO band does not reappear after C_3H_6 removal. The differences observed in recovery of Pd actives sites on MC at 100^oC might be attributed to the different Pd formations and their interaction with the support.

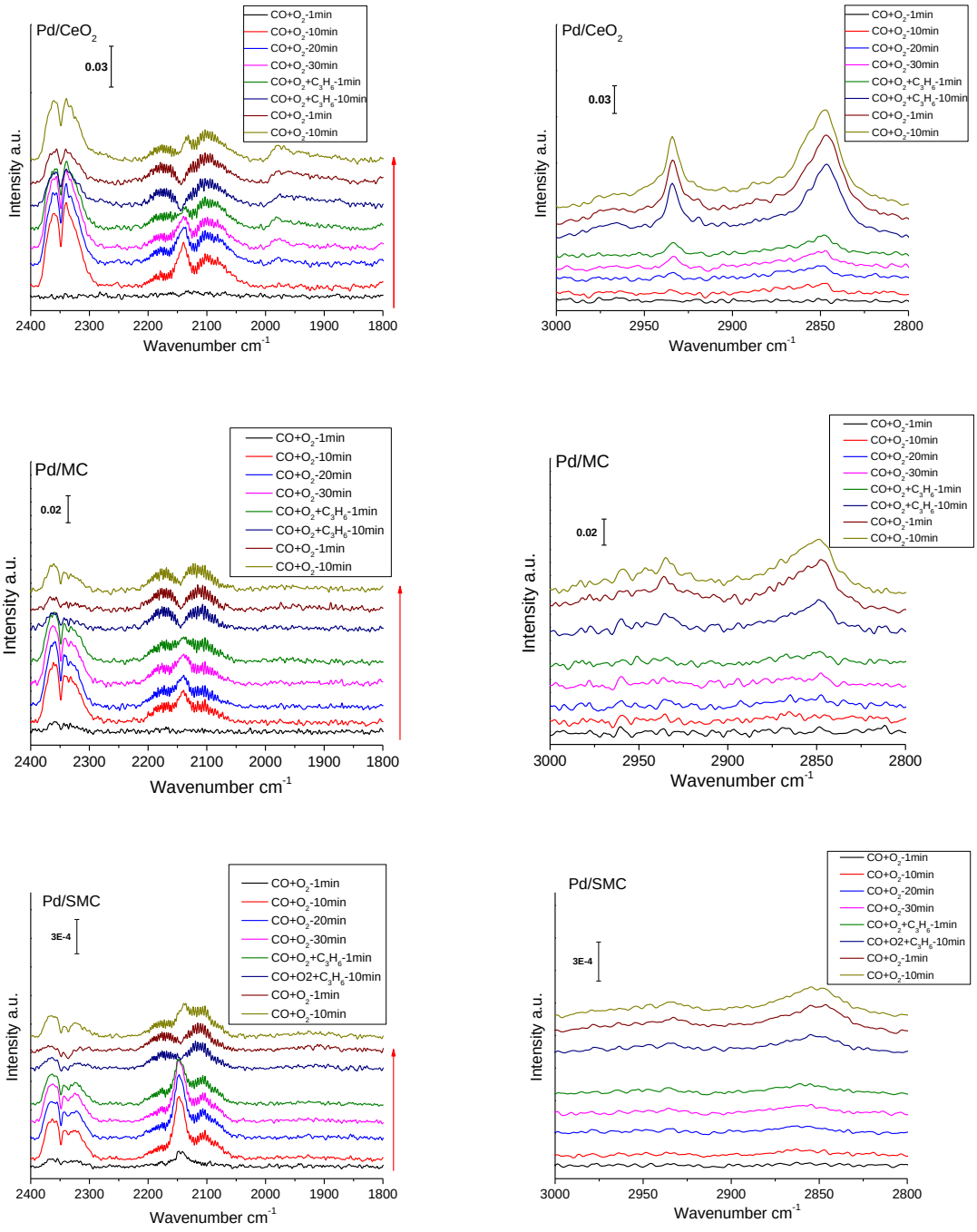

Figure 4.10 Baseline corrected in-situ DRIFT spectra of oxidation reactions over Pd catalysts.

4.3.4 Effect of SO_2 poisoning, steam and GHSV

Figure 4.11 shows the conversion of CO oxidation over the Pd/SMC. Similar to Pd/MC, addition of Mn and Sn to Pd/CeO_2 can improve the activity, and the CO conversion reached to more than 90% from room temperature to 450°C, which is above some recently reported supported Pd catalysts [94-107]. For example, Pd/MnO_x-CeO_2 prepared by a surfactant-assisted co-precipitation followed by a hydrothermal method showed a T_{90} of 60°C [108]. Ramping up and down tests shows overlapped CO conversion curves, indicating the activity is consistent and repetitive.

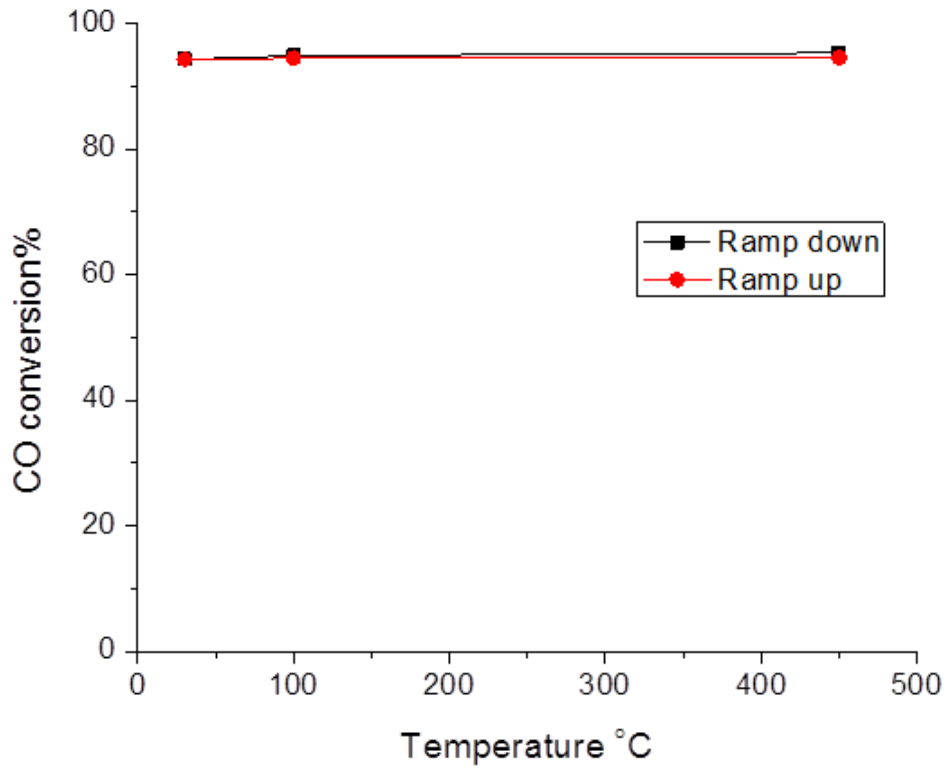

Figure 4.11 CO oxidation activity of Pd/SMC. CO/O2 ratio of 2:5 and GHSV = 40,000 h^{-1}.

To be a potential catalyst for low temperature automobile emission control application, not only the catalyst requires high activity, but also its stability under severe exhaust condition is necessary to be evaluated. For instance, SO_2 present in an automobile exhaust gas could deactivate the catalyst by forming sulfate species that can block the active sites of the catalyst [149]. Furthermore, H_2O present in the range of 5 to 10 vol% in the automobile exhaust gas [150,151]has been reported to deactivate and increase the CO oxidation light-off temperature of Pd/Al_2O_3 catalysts by the growth of Pd particle[152].

Here, the catalytic activity of the best performed catalysts, i.e. Pd/MC and Pd/SMC, was evaluated as a function of time under 200 ppm SO_2 at room temperature. As shown in figure 4.12, both catalysts kept more than 90% CO conversion in the first ca.40min. However, after 40 min, the CO conversion over Pd/MC started to decrease and finally reached to 0% CO conversion at ca.90 min. On the other hand, the Pd/SMC showed better SO_2 poisoning resistance with a slower deactivation rate than Pd/MC. Even though the CO conversion over Pd/SMC started to decrease at the same time with Pd/MC, the total deactivation occurred at ca.130 min over Pd/SMC rather than 90 min over Pd/MC. This could be explained with the preferential formation of sulfate species on Mn rather than Ce over the MC catalyst. Once the Mn sites are occupied, sulfate species might form on the Ce sites. However, with the addition of Sn, sulfate species formed preferentially on Ce rather than Mn [137]. Such selective formation of sulfate species could affect the oxygen release and storage ability of the ceria based catalysts at low temperatures. Further tests revealed that SO_2 poisoning was reversible over the Pd/MC and Pd/SMC catalysts. As shown in figure 4.13, the catalyst temperature was ramped up

from room temperature to 450°C in the presence of SO_2. Oxidation of CO was completely recovered over both catalysts at temperatures above 250°C. This is attributed to the decrease of the poisoning effect of sulfation at temperatures higher than 200°C [153].

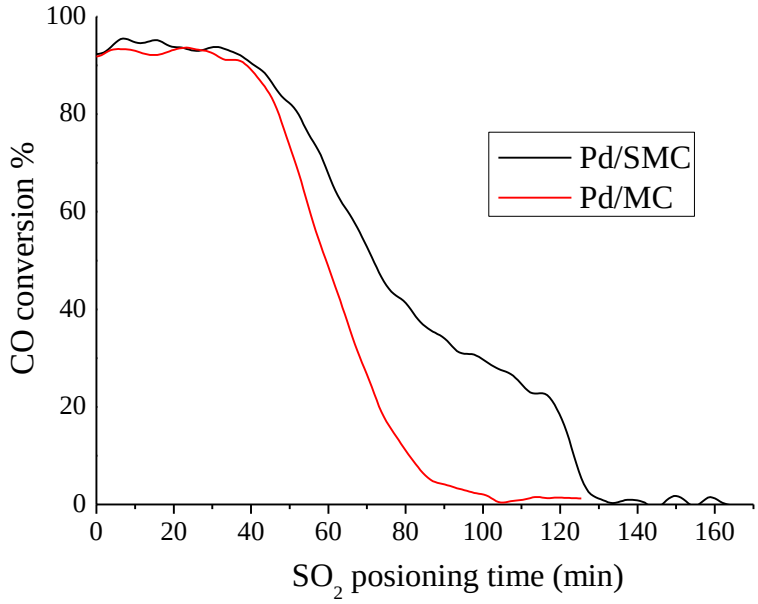

Figure 4.12 CO oxidation activity of Pd-MC and Pd-SMC catalysts at room temperature with additional 200 ppm SO_2.

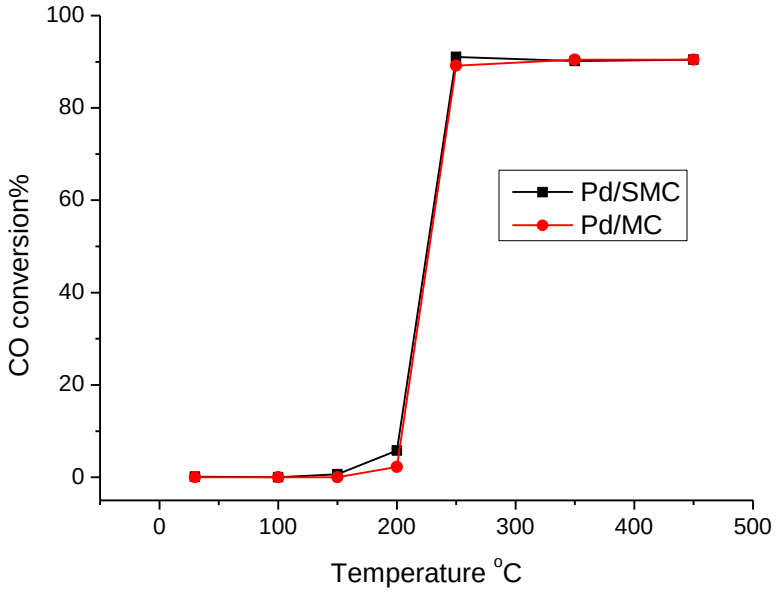

Figure 4.13 CO conversion in the prence of 200ppm SO_2 with temperature ramp from room temperature to 450°C. $CO:O_2$=2:5, GHSV=40,000h^{-1}

Due to the better SO_2 tolerance of Pd/SMC at room temperature, the catalyst has further been exposed to 8% H_2O during CO oxidation. Figure 4.14 shows the CO conversion of Pd/SMC in a temperature range of 150°C-450°C. The activity of Pd/SMC did not change compared to the results tested in dry condition indicating that H_2O does not have any effect to CO oxidation over Pd/SMC. Moreover, hydrothermal treatments (5% O_2, 8% H_2O, Ar balance, 12 hours) at 500°C and 750°C for the Pd/SMC catalyst were conducted to test the stability of Pd/SMC. It also shows that the Pd/SMC after steam aging for 12 hours at 500°C keeps the same activity as the fresh catalyst. Even if the aging temperature increases to 750°C, the Pd/SMC still keeps a good CO conversion with only slight deactivation under 150°C.

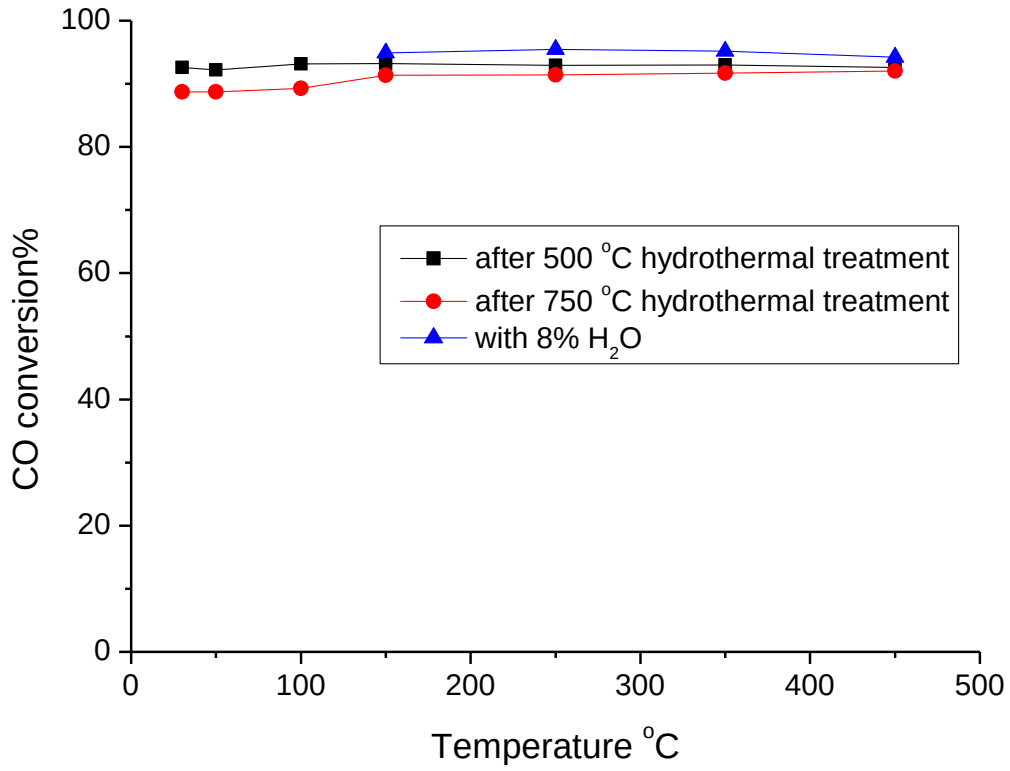

Figure 4.14 Effect of H_2O and hydrothermal aging on Pd/SMC for CO conversion. CO: O2=2:5, 8% H_2O (when used), Ar balance.

In addition to the hydrothermal aging, the Pd/SMC catalyst was exposed to higher GHSV=120,000 h^{-1} and its CO oxidation activity was evaluated as a function of temperature, as shown in figure 4.15. Increasing space velocity did not change the performance of the catalyst from room temperature to 450°C. The Pd/SMC catalyst appears promising for low temperature CO oxidation in the presence of SO_2 and H_2O.

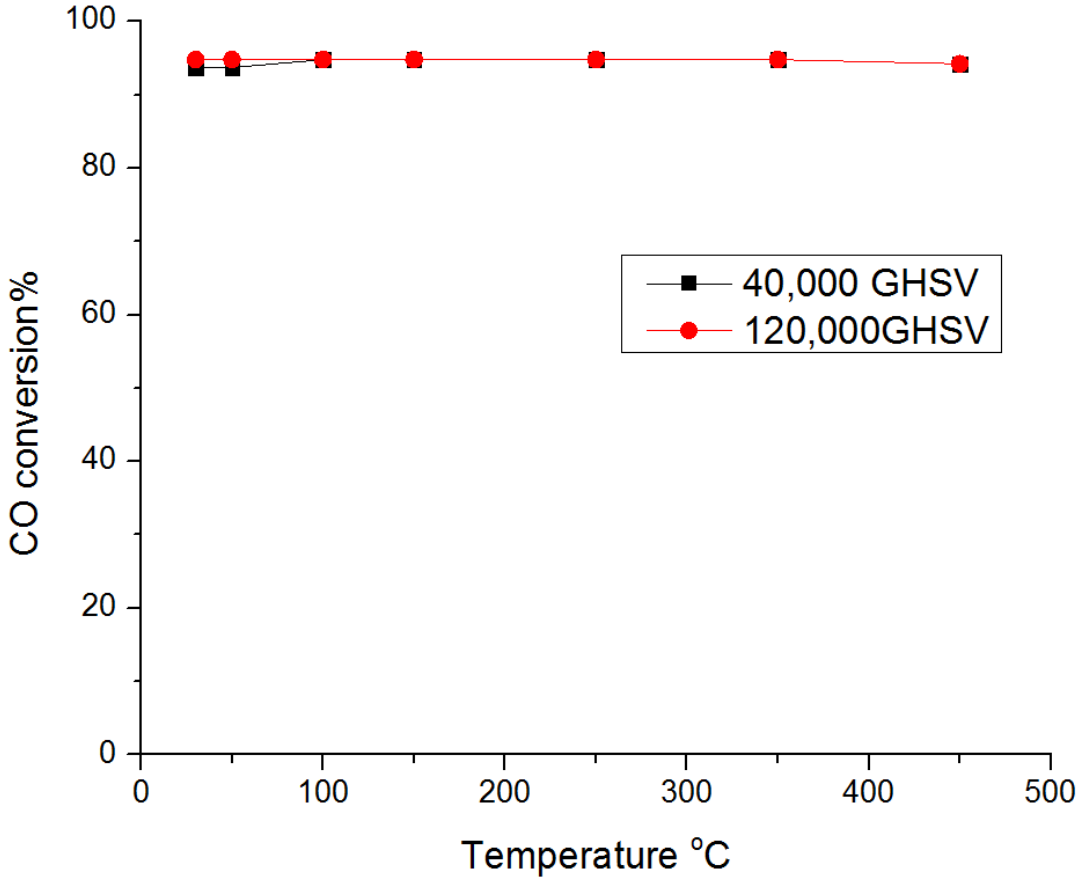

Figure 4.15 Effect of GHSV on Pd/SMC for CO conversion. CO: O_2=2:5, Ar balance.

4.4 Conclusion

Here, we evaluated the performance of the Pd impregnated Ce based catalysts for CO and HC oxidation under the LTC-D protocol. Both Pd/MC and Pd/SMC showed excellent CO oxidation activity at ambient temperature. Upon introduction of C_3H_6, the

CO light-off curve shifts to higher temperatures, indicating a competitive adsorption between CO and C_3H_6. Simultaneous oxidation of CO and C_3H_6 shows a similar light-off profile on both Pd/CeO_2 and Pd/MC, indicating that the OSC and lattice oxygen reducibility do not affect CO conversion in the presence of C_3H_6.

In the case of the simulated diesel exhaust gas, all catalysts show a CO oxidation T_{50} below 200^{o}C. Pd/MC achieves the lowest T_{50} for CO at 173^{o}C, whereas Pd/CeO_2 shows the lowest T_{50} for THC at 267^{o}C. The competitive adsorption of CO, NO and alkenes affects the light off curves of CO at both low and high temperatures. Degreening samples at 700 ^{o}C can cause segregation of Mn from the solid solution and sintering of Pd nanoparticles. In-situ DRIFTs studies reveal that C_3H_6 could immediately inhibit CO adsorption, and thereby its oxidation at 100^{o}C. Upon introduction of C_3H_6, CO adsorbed on Pd^{n+} sites disappears over all catalysts and can be partially recovered over Pd/CeO_2 and Pd/SMC after C_3H_6 is removed from the gas phase. However, Pd^{n+} sites over Pd/MC are completely blocked by C_3H_6 and are not recovered for CO oxidation.

Pd/SMC showed better SO_2 resistance at room temperature than Pd/MC. Further experiments revealed that SO_2 poisoning was reversible at reaction temperatures above 200◦C. The catalytic activity of the Pd/SMC did not change after hydrothermal aging indicating that Pd/SMC could be a promising catalyst for low temperature CO oxidation.

Chapter 5

Investigation of the Pd structure and reactivity on Mn doped α-Fe_2O_3 nanorod with controlled facet

5.1 Introduction

One of the classic strong metal–support interactions (SMSI) is the alteration of the charge state of the metal by electron transfer from or to a support which leads to an improvement of reactants activation and thus promotes the catalytic properties [154]. Recently, it was elucidated that d-band electronic perturbation of late-transition-metal catalysts that is induced by a subtle change in the structure of the support has a strong influence on the intrinsic reactivity [155-156]. Iron oxide supported Pd catalysts have been studied as model systems for the effect of SMSI in CO oxidation [157]. Electron transfer from Pd to FeO_x coupled with oxygen transfer from FeO_x to Pd during reaction is the current mechanistic understanding for the Pd-Fe system. However, the effect of d-band electronic perturbation has not yet been studied to get a complete understanding on further promoting the reactivity of Pd-Fe system.

Doping a secondary metal into a metal oxide support can change the support electronic structure; meanwhile maintaining the original crystal structure [158]. One the other hand, different exposed facets in the same metal oxide support can change the electronic structure of surface and greatly influence the Pd structure and reactivity as

well[146]. A feasible way to investigate the unsolved question above is to homogeneously dope a secondary metal into iron oxide support with structurally fixed and spatially uniform surface, to rule out the facets effect.

Herein, we designed Pd supported on α-Fe_2O_3 and Mn doped α-$Fe_{2-x}Mn_xO_3$ nanorods with the same hematite structure and exposed facets to study in more detail how SMSI depends on the electronic structure change of support. CO oxidation was used as a probe reaction to evaluate structure-activity relationships.

5.2 Experimental

Preparation of the Mn-doped α-FeOOH nanorods: All of the chemical reagents used here were of analytical grade without further purification. In a typical procedure, 0.256g polyvinyl pyrrolidone (PVP: MWz 58,000) was dissolved into 20 mL of deionized water, while 1.8g NaOH was dissolved in 10 mL of deionized water. Then $FeCl_3$ (7×10^{-3} M) and $MnCl_2\cdot4H_2O$ (3.5×10^{-3} M) were dissolved in deionized water (50 mL) and stirred to form a homogenous solution. The transparent solution of PVP and NaOH were slowly dropped into the above solution in turn. The whole mixture was stirred for another 20 min to obtain a homogeneous solution and then transferred into a 100 mL Teflon-lined stainless-steel autoclave. The autoclave was put into an oven at 120 ℃ for 12 h. After the autoclave was cooled to room temperature naturally, the resulting product was first washed with 15 wt% HCl solution twice(2 hours each time) and then rinsed with deionized water and absolute ethanol several times. The obtained sample was dried at 60 ℃ in vacuum for 12 h. In a contrast experiment, α-FeOOH nanorods were prepared through the same procedure but in the absence of $MnCl_2\cdot4H_2O$.

Preparation of the Mn-doped α-Fe_2O_3 nanorods: The Mn-doped α-FeOOH nanorods were annealed in air at 300 ℃ for 4 h with a slow ramp rate of 1 ℃ min^{-1}. 1wt% Pd was loaded onto the iron-oxide based supports via an impregnation method and calcined at 300°C to produce Pd/α-Fe_2O_3 and Pd/α-$Fe_{2-x}Mn_xO_3$.

Similar to Pd-Ce based catalysts tests; CO oxidation was conducted in a plug flow rector, where CO conversion was measured by a mass spectrometer. 200 mg of catalyst was placed in the reactor for each run. The gas mixture of 2.0% CO, 5% O_2 and balanced Ar was fed to the reactor at a GHSV of 40,000 h^{-1}.

Scanning electron microscopy (SEM) images and EDX of the ZSM-5 catlaysts were obtained using a Zeiss Ultraplus Thermal Field Emission Scanning Electron Microscope with an acceleration voltage of 15 kV. STEM were conducted by a JEOL 2100F 200 kV FEG–STEM. XRD, XPS, and TPR characterization were used the same instrument and methods as previous described.

5.3 Results and discussion

The XRD patterns of the as-obtained Mn-doped α-FeOOH and α-FeOOH are displayed in figure 5.1. The diffraction peaks of the two kinds of products are in agreement with orthogonal α-FeOOH (JCPDF Card No. 29-0713, space group Pbnm), and no impurities were found in these XRD patterns. Crystallographic structure of α-FeOOH shows the Fe octahedron is linked with other four Fe octahedral through edge sharing and four others are linked through double corner sharing. It appears that the 1D structure of Mn-doped α-FeOOH might be reinforced by chemical linkages to maintain the stability of the structure. [159] Comparing the patterns of Mn-doped α-FeOOH with

that of pure α-FeOOH, no crystalline manganese or manganese oxides were observed in the Mn-doped α-FeOOH XRD pattern.

After calcination, α-Fe_2O_3 nanorods with and without Mn doping were obtained. Their patterns can be indexed to pure α-Fe_2O_3 phase (JCPDS No. 33-0664). While an additional peak at 22^o shows up in the Mn doped sample, which is corresponding to formation of impure $MnFe_2O_4$ particle [159]. Since the peak intensity is very low, the amount of impurity is very small compare to the α-Fe_2O_3 phase. With similar α-Fe_2O_3 phase peaks, the Mn-doped α-FeOOH precursor is almost completely transformed into Mn-doped α-Fe_2O_3. The XRD pattern of Pd catalysts shows the hematite Fe_2O_3 structure is still the dominant structure. For Mn doped sample, a small amount of impure phase still exists. No PdO diffraction peak at 42^o appears in both Pd catalysts. The lack of Pd peak could be attributed to the high dispersion or small amount of Pd loading.

SEM images justify the nanorod morphology of Fe, Fe-Mn supports and Pd loaded catalysts, shown in figure 5.2. More detailed Pd structure and surface structure identification is characterized by STEM. Figure 5.3 shows the Pd/Fe_2O_3 structure STEM image with different resolution. The nanorod support with rectangular shape and 40nm width can be clearly distinguished. The bright spots on the nanorods are Pd particles that exhibit good Z contrast with the Fe. The majority of Pd particle sizes are in the range of 2-5nm. Several bigger aggregated Pd also appears. The Fe_2O_3 exposed (104) lattice plane with 0.27 nm distance[160]. The Pd particle lattice plane is 0.22 nm, which is corresponding to PdO (110) plane[161].

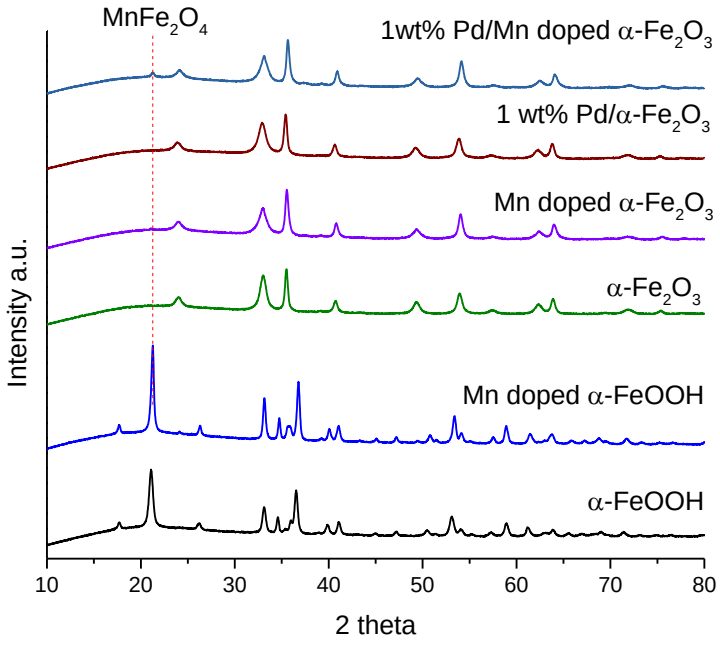

Figure 5.1 XRD of XRD patterns of α-FeOOH, Mn-doped α-FeOOH, α- Fe_2O_3, Mn doped α- Fe_2O_3, and 1 wt% Pd catalysts.

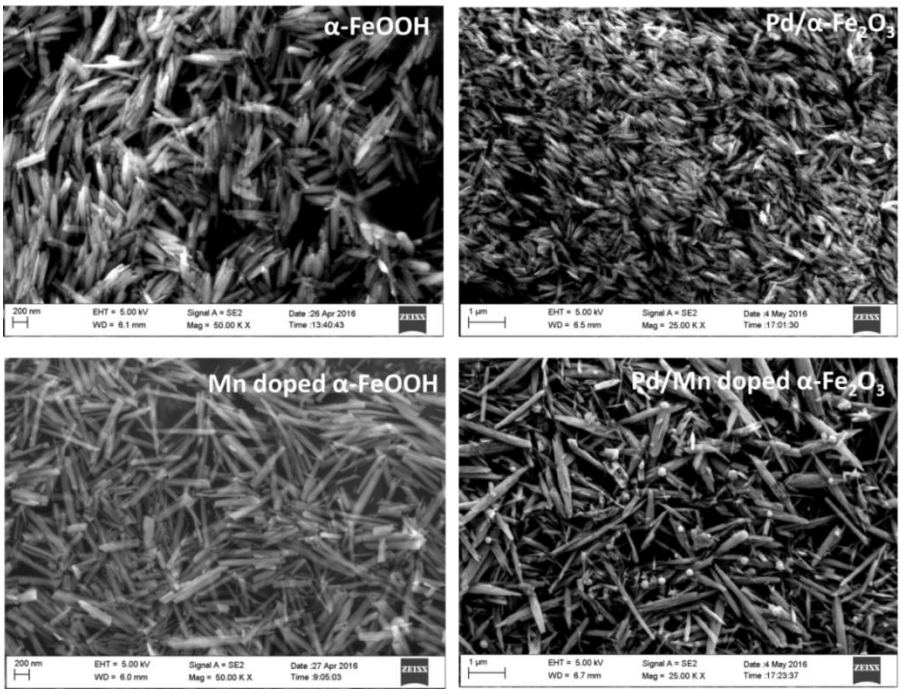

Figure 5.2 SEM image of Fe based nanorod supports and Pd loaded nanorods after calcination.

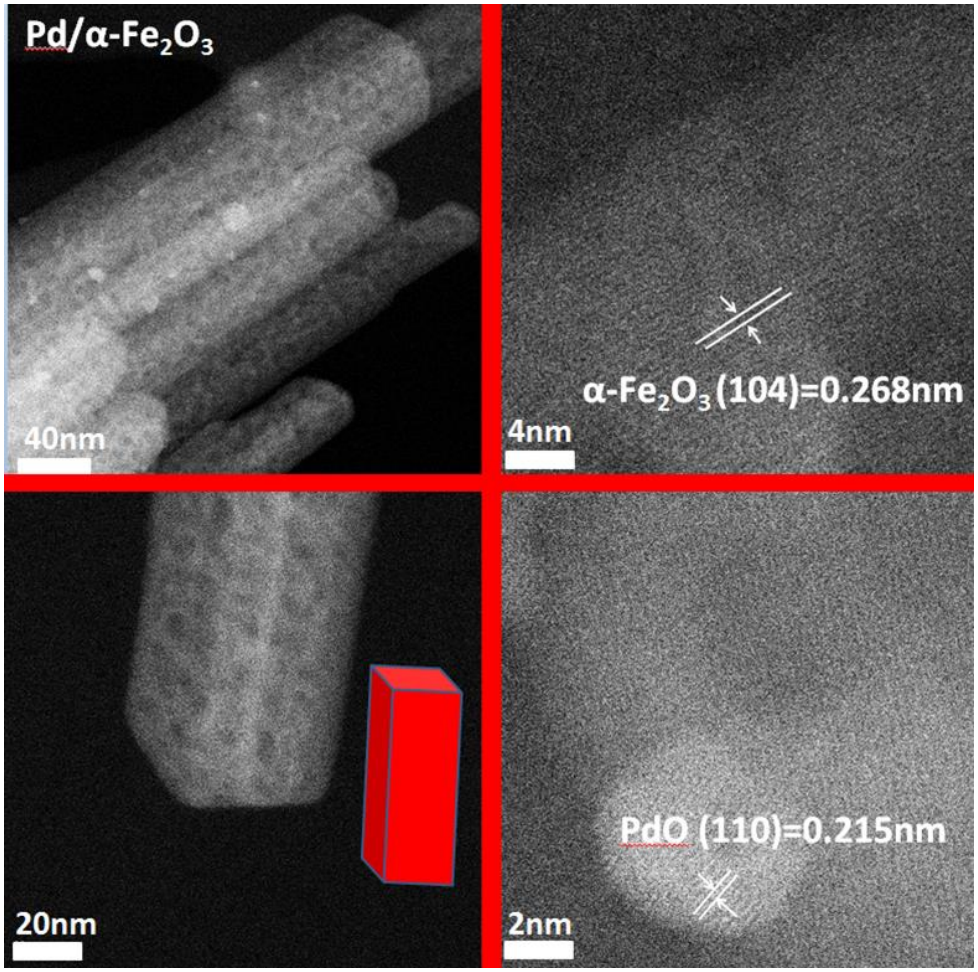

Figure 5.3 STEM image of Pd/Fe_2O_3 catalyst.

In figure 5.4, $Pd/\alpha\text{-}Fe_2O_3$ nanorod shows almost 100% CO conversion at 150°C, but zero conversion at 75°C. With Mn doping into $\alpha\text{-}Fe_2O_3$, $Pd/\alpha\text{-}Fe_{2-x}Mn_xO_3$ nanorod shows much higher activity at lower temperature and achieves almost 100% CO conversion at 75°C. Electronic structure and oxidation state of Pd are characterized by X-ray photoelectron spectroscopy (XPS), shown in figure 5.5. The $3d_{5/2}$ peak of the PdO reference sample locates at 336.6±0.2 eV. The Pd $3d_{5/2}$ peak of 1 wt% Pd/ $\alpha\text{-}Fe_2O_3$ can be deconvoluted into two peaks at 337.7±0.2 and 336.5±0.2 eV. The lower binding energy peak at 336.5±0.2 eV is similar to the PdO reference sample and can be attributed to the

crystalline PdO phase, while the higher binding energy peak is due to the formation of highly dispersed Pd^{2+}, possibly forming single atom sites [158]. In the case of 1 wt% Pd/α-$Fe_{2-x}Mn_xO_3$, only a high binding energy peak is detected at 337.3 eV, which is different from both peaks of Pd/α-Fe_2O_3. This suggests different Pd species can form on pure and doped iron oxide surfaces and the support electronic structure change do affect the Pd d-band electronic structure.

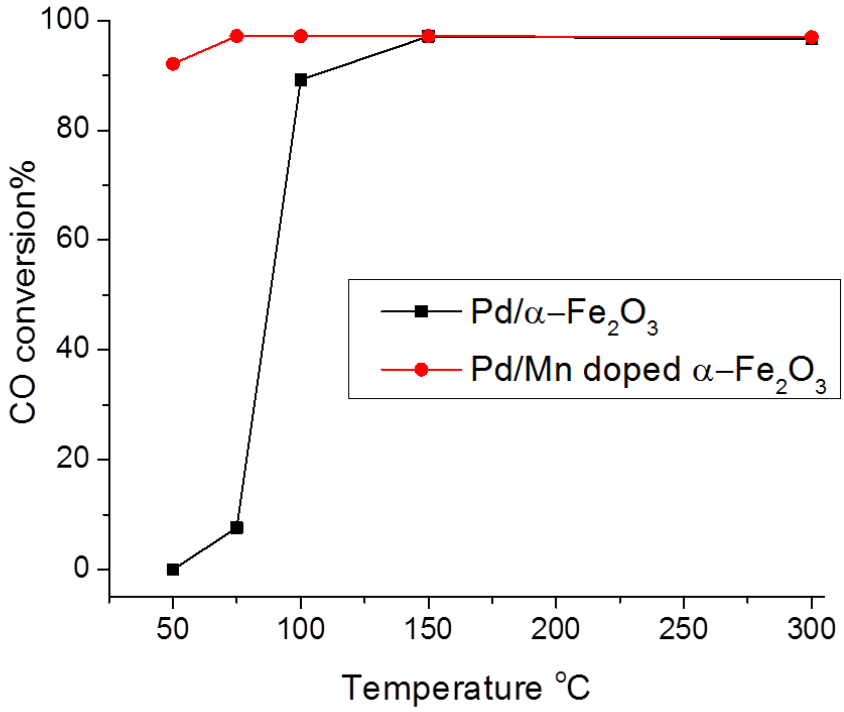

Figure 5.4 CO oxidation activity of Pd catalysts. CO/O_2 ratio of 2:5 and GHSV = 40,000 h^{-1}.

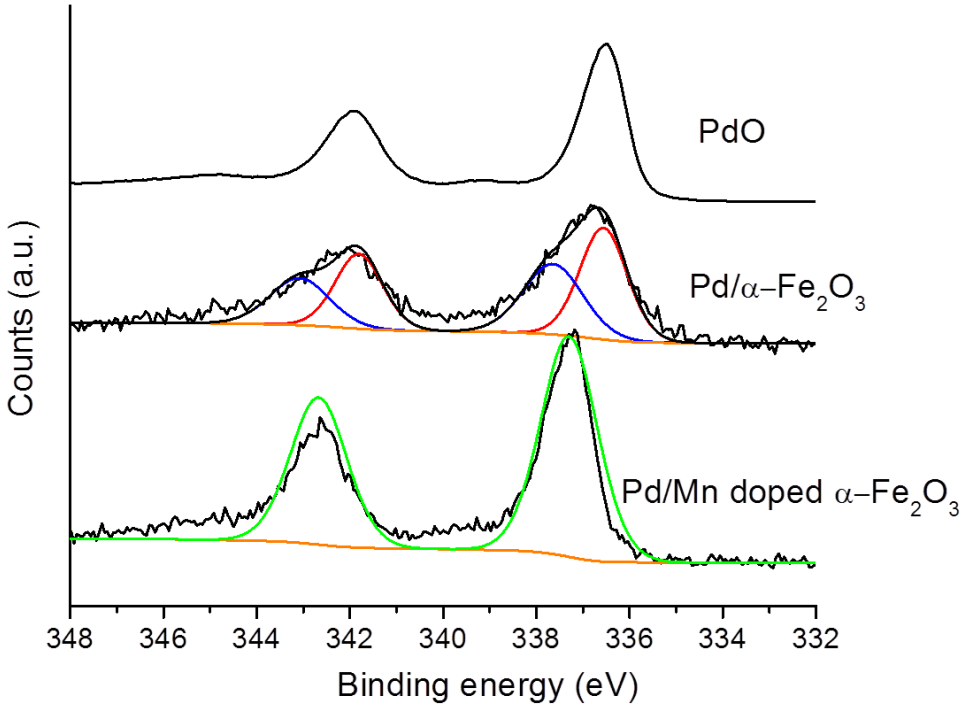

Figure 5.5 Pd 3d core-level XPS of Pd-Fe based catalysts and PdO reference.

Reducibility of the lattice oxygen is investigated through H_2-TPR. As shown in figure 5.6, the Fe_2O_3 support presents a broad reduction peak above 400°C. With Mn doping, additional reduction peaks shows up from 230°C to 450°C, which is corresponding to Mn reduction steps. The details have been explained in the Pd/MC case. The Pd/α-Fe_2O_3 catalyst exhibits two reduction regions at around 230°C and 400-800°C, which can be attributed to the reduction of PdO and Fe_2O_3 support, respectively [162]. The reduction profile of Pd/α-$Fe_{2-x}Mn_xO_3$ also shows similar reduction at 210° and 400-800°C. Interestingly, there is an additional peak at 75°. The two peaks at low temperature may both correspond to the reduction of Pd^{2+} to Pd^0 due to the similar total peak area of

the PdO reduction peak of Pd/α-Fe_2O_3 sample. Based on XPS, there should be only one Pd species, but two reduction peaks shows up. This might be because Mn doping changes the surface PdO electronic structure or the chemical interaction with the Mn-Fe support, which lead to the reduction of PdO in two steps.

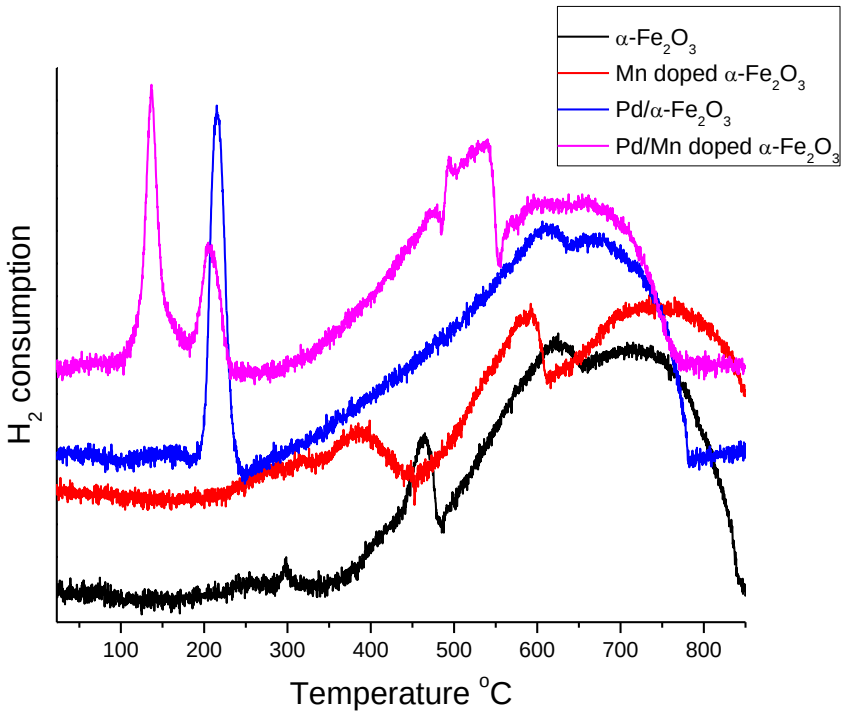

Figure 5.6 H_2-TPR profiles of Pd catalysts and supports.

In the future CO-O_2 pulse reaction and in-situ diffuse reflectance infrared Fourier transform spectroscopy (DRIFTs) will be carried out to give a more comprehensive understanding on metal-support interaction. Density function theory (DFT) calculation will be employed to study the electronic property of Fe-based support surface and the electronic interaction with Pd.

5.4 Conclusion

Pd supported on Fe_2O_3 and Mn doped α-Fe_2O_3 nanorods were successfully prepared. XRD and SEM images justify the catalysts structure, nanorod morphology and size. STEM images of Pd/Fe_2O_3 further distinguished the PdO particle size and exposed facet of α-Fe_2O_3 and PdO. The Pd/Mn doped α-Fe_2O_3 shows over 90% CO conversion at 50^{o}C, at which Pd/α-Fe_2O_3 shows almost no activity. XPS of Pd indicate PdO with different electronic structure form on the Mn doped surface. The H_2-TPR comparison indicates the Mn doping results in the lower temperature shift of PdO reduction peak. This may attribute to enhanced metal-support interaction that creates the unique more reducible PdO structure on the Mn doped Fe_2O_3 surface. To elucidate the Pd structure and reactivity change on doped oxide surface with controlled facet, more investigation techniques will be used to provide new fundamental insight on metal-support interaction and active sites design approach.

Chapter 6

Evaluation of sulfur effect on SSZ-13 zeolite catalysts for NO_x reduction

6.1 Introduction

In NH_3-SCR reaction, there has been a great deal of attention paid to copper-exchanged molecular sieve Cu-SSZ3-13 as it showed excellent hydrothermal stability [67]. The reason is that its narrow pore structure makes it difficult for aluminium moieties, which are the products of dealumination, to leave. As the Cu/Al ratio became higher due to the fact that the Cu^{2+} in a SSZ-13 cage might form CuO_x species, the thermal deactivation of Cu-SSZ-13 became more severe. These CuO_x species might grow and then destroy the cage and channel of the zeolite.

The commercial SCR catalysts for coal power plants contain V_2O_5, which is a toxic metal for the environment and human beings. The more environmentally friendly composition of zeolite with excellent hydrothermal stability and wide operation temperature window may be a good candidate to replace current commercial catalysts in power plants NO_x control.

While hydrothermal stability has been extensively discussed, the stability towards sulfur is another issue that should also be taken into account. The sulfur content in fuels is legislated to be less than 10 ppm. However, in coal power plants, the SO_2 concentration can be up to 500ppm and causing severe catalysts poisoning and deactivation issues. Such high amount of SO_2 effect on the SSZ-13 catalysts have not yet been considered or

tested in the reaction system. In this work, SSZ-13 catalysts loaded with Cu, Fe, Ce are synthesized and tested under SO_2 and H_2O feed conditions for NH_3-SCR activity comparison.

6.2 Experimental

6.2.1 SSZ-13 zeolite catalysts

SSZ-13 was prepared by the following steps: Tetraethyl orthosilicate (TEOS, sigma 98%), N,N,N-trimethyl-1-adamantanamine hydroxide (TMAdaOH, 25 wt %, Sachem Inc.), and DI water were mixed for 2 h, and then $Al(OEt)_3$ (Strem Chemical, 99%) was added to the solution to obtain a final gel composition of $SiO_2/H_2O/TMAdaOH/Al_2O_3$ of 1:20:0.5:0.14 and stirred for another 12 h. The resulting solution was then transferred into Teflon-lined autoclaves and heated at a temperature of 423 K under static conditions for 6 days. After that, the sample was washed with DI water and dried at 353K overnight. The as-made product was then calcined in air at 823 K for 8 h, heating at a ramping rate of 5 K/ min to prepare the starting form of H-SSZ-13.

After calcination, all zeolite samples were ion-exchanged in a 0.1M solution (2 g of zeolite/L of solution) of NH_4NO_3 (Fisher Scientific) at 80 ◦C for 8 h and dried in air at room temperature. 1 g of NH_4-zeolite was then added to the 0.1M $CuSO_4$, 0.1M $Fe(NO)_3$, 0.1 M $Ce(NO)_3$ solution and 0.5M $Fe(NO_3)_3$+0.5M $Ce(NO_3)_3$, respectively. These solutions were stirred in an oil bath at 80 ◦C for 1 h. Solutions were then vacuum filtered with deionized water, and the resulting Cu-SSZ-13, Ce-SSZ-13, Fe-SSZ-13 and Ce/Fe-SSZ-13 were dried at room temperature and calcined at 823K for 3 h.

6.2.2 Reaction test and catalysts characterization

The experiments were run in a fixed bed continuous-flow reactor, where the NO conversion was measured by the quadruple mass spectrometer. All catalytic reactions were performed using a feed stream containing 500ppm NO, 500ppm NH_3, 5% O_2, 5% CO_2, 8% H_2O(when used), 500ppm SO_2(when used), and balance N_2. The gas hourly space velocity was 40,000 h^{-1}. The NH_3-SCR activity of all samples was tested from 150 to 450 ℃, with 100 ℃ increments. XRD, SEM, and XPS characterizations were carried out using similar instruments and methods as described in previous chapters.

6.3 Results and discussion

All XRD patterns in figure 6.1 match the standard SSZ-13 pattern and show that no additional peaks appear after ion-exchange, which suggest there is little aggregated metal particle or metal oxide in the catalysts. The (101) peaks shift to a lower angle when the exchanged ion size becomes bigger (Ce>Fe), which suggests lattice cell shrinkage happens after ion-exchange. The peak shift and d spacing calculation based on (101) peak is shown in table 6.1.

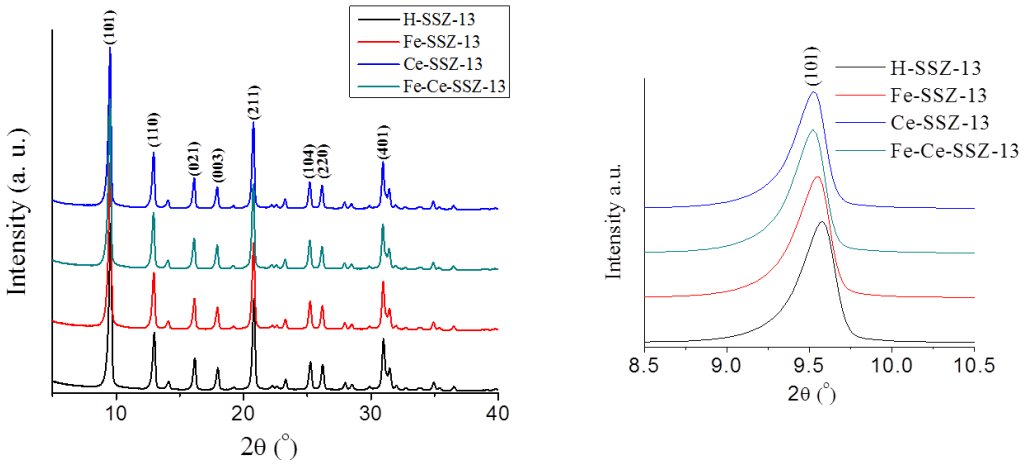

Figure 6.1 XRD patterns of SSZ-13 based catalysts.

Table 6.1 Peak shift and d spacing calculation of SSZ-13 samples

Sample	2-Theta	d
H-SSZ-13	9.585 (0.004)	9.2199 (0.0072)
Fe-SSZ-13	9.553 (0.004)	9.2503 (0.0084)
Fe-Ce-SSZ-13	9.529 (0.004)	9.2735 (0.0084)
Ce-SSZ-13	9.518 (0.003)	9.2849 (0.0066)

In figure 6.2, the particle agglomerates are made up of individual jellybeans and a small amount of cube shaped crystals measuring approximately 1μm in size. EDX results indicate that the Si/Al ratio is around 6-7, shown in figure 6.3. After ion exchange, the SSZ-13 crystals maintain their previous morphology, and ICP analysis reveals a total of 1.8 wt % Cu and 0.53 wt % Fe. Ce related ICP results have not yet been performed.

NH_3-SCR reaction experiments were performed using a feed stream containing 500ppm NO, 500ppm NH_3, 5% O_2, 5% CO_2, 8% H_2O (when used), 500ppm SO_2 (when used), and the balance was N_2. The gas hourly space velocity was 40,000 h^{-1}. The NH_3-SCR activity of all samples was tested from 150 to 450 ℃, with 100 ℃ increments.

Figure 6.4 shows the NO conversion for catalysts under simulated flue gas conditions. Without metal loading, H-SSZ-13 is found to have no catalytic activity. After ion-exchanging with Cu, Fe and Ce, the NO conversion of SSZ-13 catalysts jump to more than 80% in a high temperature window (350-450 ℃). Moreover, Cu-SSZ-13 show more

than 80% NO conversion in a low temperature window between 150-250 ℃, while the NO conversion on other catalysts gradually drops down to less than 30%. Interestingly, the bi-metal exchanged Ce-Fe-SSZ-13 catalyst shows higher catalytic activity than either single metal catalyst, which is probably due to a synergy effect between Fe and Ce in the NH_3-SCR reaction system [54]. The commercial catalyst shows over 90% NO conversion above 300^{o}C, but has almost zero activity at 150^{o}C.

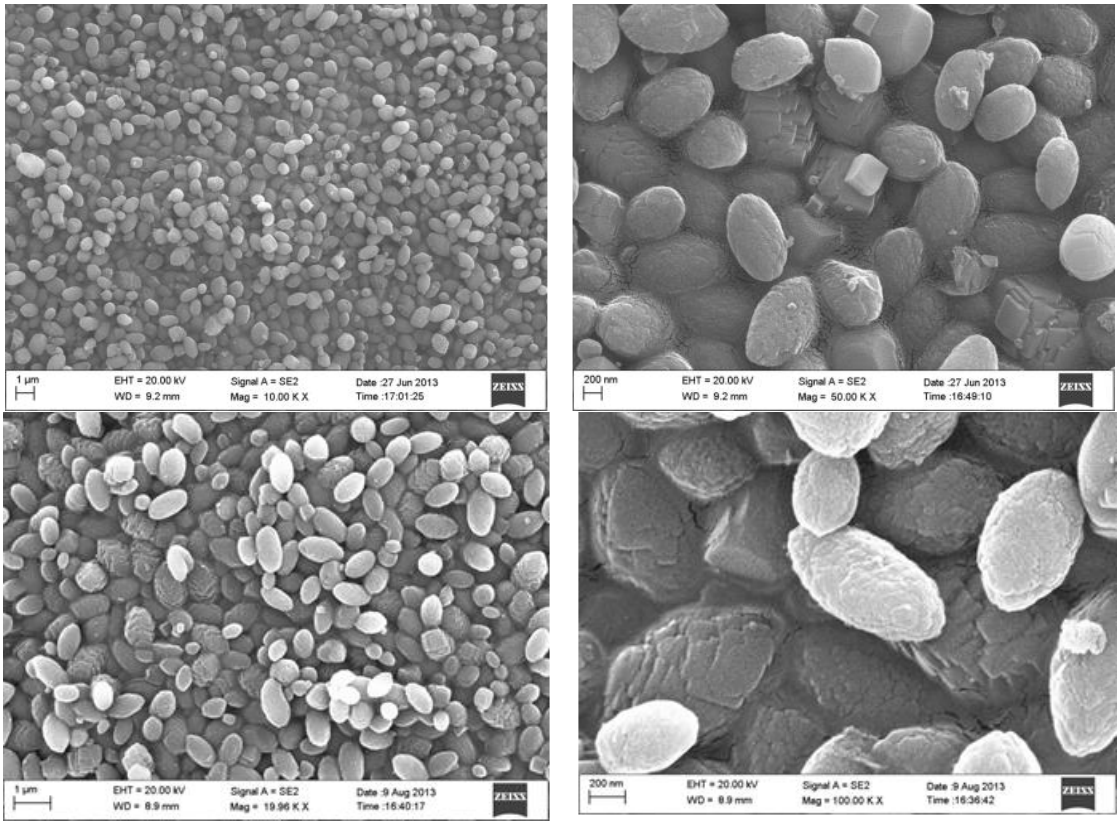

Figure 6.2 SEM images of SSZ-13 before (top) and after (bottom) SCR reaction with SO_2 and H_2O.

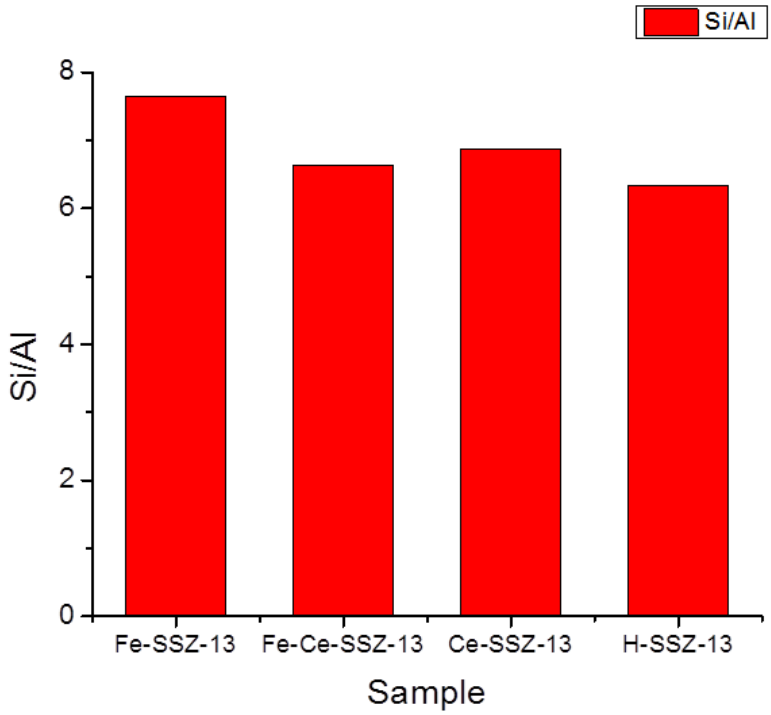

Figure 6.3 Si/Al ratio of SSZ-13 based catalysts.

The NH_3-SCR reaction results with SO_2 and H_2O in the feed are shown in Fig. 6b. All catalysts are found to deactivate at low reaction temperatures with the addition of SO_2 and H_2O vapor. Among them, Cu-SSZ-13 shows the best poisoning resistance and keeps more than 90% NO conversion at high temperatures, which is comparable to commercial catalyst. At low temperatures, catalysts deactivate more than at high temperatures, which might be due to the formation of $(NH_4)_2SO_4$ on the catalyst [163-165]. The morphology of SSZ-13 keeps the same as fresh catalyst, shown in figure 6.2, suggesting that the catalysts structure is stable after reaction with SO_2. In figure 6.5 XPS results support the possible formation of $(NH_4)_2SO_4$, indicating that both NH_4^+ and SO_4^{2-} are present on the surface of the catalysts.

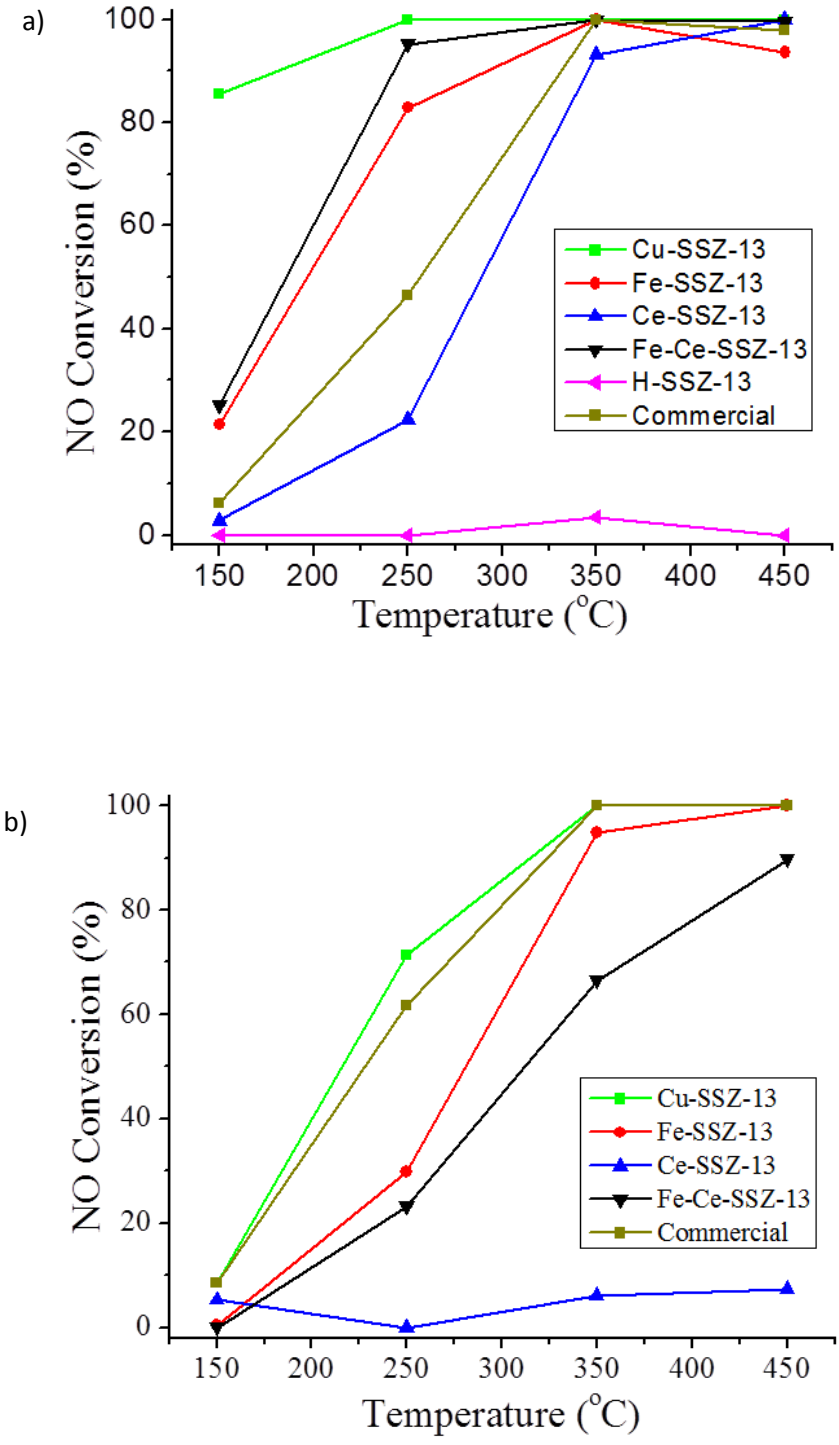

Figure 6.4 NH_3-SCR activity a) without H_2O or SO_2, b) with H_2O and SO_2. NO: 500 ppm, NH_3: 500 ppm, O_2:5%, CO_2: 5%, SO_2 (when used): 500ppm, H_2O(when used): 8%, N_2 balance, GHSV: 40,000 h^{-1}.

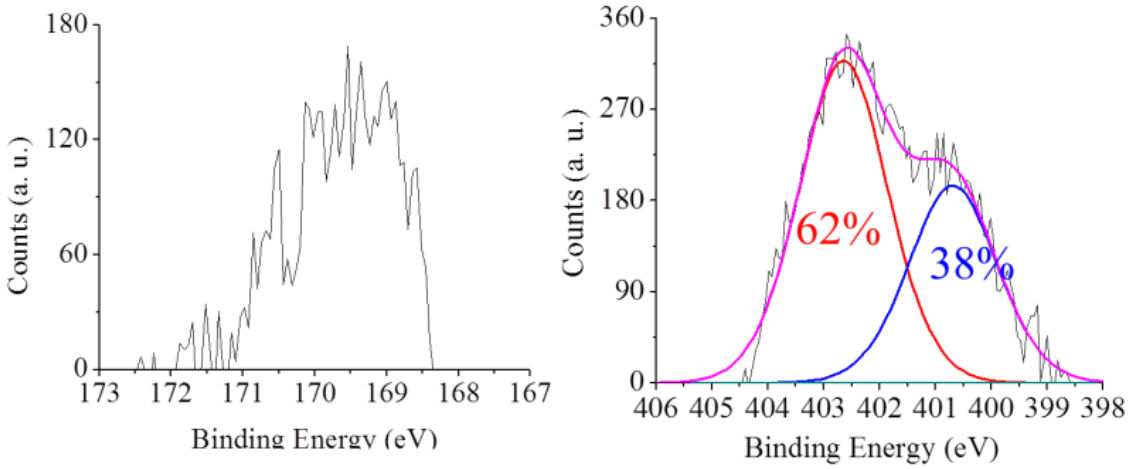

Figure 6.5 XPS of a)S 2*p* on Cu-SSZ-13, b) N 1*s* on Cu-SSZ-13

6.4 Conclusion

In the ammonia selective catalytic reduction (NH_3-SCR) of NO_x, Cu-SSZ-13 zeolite catalysts show the best NO conversion (over 95%) from 150-450^oC when compared with Fe and Ce based SSZ-13. Moreover, in the presence of SO_2 and H_2O, Cu-SSZ-13 still keeps a relatively high sulfur resistance at temperatures between 250-450^oC.

Chapter 7

Conclusions and future work

7.1 Conclusions

This work developed and studied the Pd based catalysts in a relatively comprehensive way from catalysts design to evaluation, fundamental structure-activity relationship characterization to practical application simulation, scalable/industrial synthesis to facet controlled model catalysts preparation. The goal was to improve the current stage of catalysts activity for air pollution elimination. The fundamentals were also carefully investigated to guide the future novel catalysts design.

Pd supported on MnO_x-CeO_2 and SnO_2-MnO_x-CeO_2 solid solution show excellent room temperature CO oxidation activity. The additional Sn doping can improve the catalyst SO_2 resistance and maintain higher CO conversion compare to Sn free sample in a short period of time. The Pd/MC and Pd/CeO_2 catalysts were selected to compare doping effect on the Pd structure change and reactivity. The high activity of Pd/MC is attributed to superior lattice oxygen transfer interaction between Pd and support, founded by multiple in situ and ex situ characterizations. This results shows that not only the spillover effect can happen on metal support interface, but also the lattice oxygen reverse spillover.

The practical application of Pd-Ce based catalysts were tested under simulated diesel exhaust condition. The CO light-off temperature of Pd/MC increased to 170^{o}C due to competitive adsorption of CH_x and NO_x, while it is still lower than the commercial DOC catalysts (200^{o}C). The comparison of structure characterizations before and after hydrothermal aging shows that the Pd is attempting to aggregate and solid solution support is tending to segregate. However, such minor change is not significant enough to change catalysts activity. It is predictable that extensively increasing the aging or reaction time may finally cause the total phase separation of MC support and formation of much larger PdO particle, which will deactivate the catalysts. So far, the improvement of catalysts stability is a still a challenging topic in industry. The typical method is incorporating stabilizer into the active phase. In the future, self-healing concept may be employed to the catalysts design, which focuses on the reversible transformation of structure under different reaction conditions.

The results of the Pd/Fe-Mn nanorod project shows similar trend as Pd-Ce project. Solid solution structure greatly improves the low temperature CO oxidation activity. The similar well-controlled facet on both Fe and Mn-Fe nanorods provide a good model platform to study the doping effect, meanwhile ruled out many factors that may contribute to activity. The regular nanorod structure is also easier to be modeled by DFT calculation, which is convenient to incorporate theatrical calculation into experimental data.

The Cu-SSZ-13 zeolite was a game changing catalyst for automobile NO_x emission control. We were interested in transfer such technology into coal power plant application. The high SO_2 condition reaction tests shows that Cu-SSZ-13 has slightly

better NO_x conversion than commercial V-W-Ti catalyst, which is toxic to environment. However, the cost of zeolite catalysts is much higher than the metal oxide catalyst due to the use of expensive organic template in the synthesis process. The development of low cost zeolite preparation method and recipe will facilitate and open more market for zeolite application. More and more researchers are developing novel synthesis pathways without templates.

7.2 Future work

In the Pd/Ce based catalytic system, the Mn-O and Ce-O bond characterization during CO oxidation reaction will be studied by time resolved XAS. This could provide more straightforward evidence for the oxygen transfer interaction with Pd. With high resolution in situ XAS, the transient oxidation state change of Mn and Ce could be characterized in XANES spectra. The EXAFS spectra can be used to analyze Mn-O and Ce-O coordination number and bond distance, which can provide information about oxygen transfer effect on dynamic catalysts structure change.

For more active oxidation catalysts design, two pathways may be used. The first is modifying noble metal structure with affinity for the oxygen that is transferred from the support and lower transfer energy barrier. Particle size, shape, facets or bimetallic alloy can be used as design factors to adjust such property. The second path is looking for new support structure that has higher oxygen storage and release ability than Ce^{4+}/Ce^{3+} and $Mn^{4+}/Mn^{3+}/Mn^{2+}$ redox couples in fluorite structure. Such structure development may not limit to solid solution concept, but also new and unique multi-metal oxide structure that is developing rapidly in inorganic chemistry research field.

In the Pd/Fe based catalytic system, in situ DRIFTs, STEM, XAS and DFT calculation will be conducted. The DRIFTs can provide details on surface reaction and the Pd sites structure, which is helpful to understand catalysts activity. STEM for Pd/Fe system is crucial important, because it can provide clear images of Pd size and structure. By analyzing size distribution, we may able to further explain whether the assignment of the high and low binding energy in XPS is attributed to size effect or electronic interaction between Pd and support. The regular nanorod morphology of Fe based supports make it easier to model the catalysts structure by DFT, which is convenient to incorporate theatrical calculation with XAS results. Combining DFT and EXAFS could make the catalyst structure model more valid and realistic, which is able to elucidate the Pd structure and reactivity change on the doped oxide surface with controlled facet, and further understand the SMSI.

References

[1] G. Centi, P. Ciambelli, S. Perathoner, P. Russo, Catal. Today 75 (2002) 3–15

[2] I. Lefort, J.M. Herreros, A. Tsolakis, Environ. Sci. Technol. 48 (2014) 2361−2367

[3] P.Iodice, A. Senatore, G. Langella, A. Amoresano, Appl. Energy, 179 (2016)182-190.

[4] G. Lenaers, Sci. Total Environ. 190 (1996)139-147

[5] R. C. Rijkeboer, Catal. Today 11 (1991) 141-150

[6] P. Thormählen, M. Skoglundh, E. Fridell, B. Andersson, J. Catal. 188 (1999) 300-310

[7] D. Cunningham, T. Kobayashi, N. Kamijo, M. Haruta, Catal. Lett. 25 (1994) 257-264

[8] L. Simonot, F. Garin, G. Maire, Appl. Catal. B 11 (1997) 167-179

[9] M. Meng, P. Lin, Y. Fu, Catal. Lett. 48 (1997) 213-222

[10] Y. F.Y. Yao, J. Catal. 33 (1974) 108-122

[11] M. Haruta, N. Yamada, T. Kobayashi, S. Iijima, J. Catal., 115 (1989) 301-309.

[12] M. Haruta, T. Kobayashi, H. Sano, N. Yamada, Chem. Lett., (1987) 405-408

[13] M. Haruta, S. Tsubota, T. Kobayashi, H. Kageyama, M.J. Genet, B. Delmon, J. Catal. 144 (1993) 175-192 [14] N. Lopez, T. Janssens, B. Clausen, Y. Xu, M. Mavrikakis, T. Bligaard, J.K. Nørskov, J. Catal. 223 (2004) 232-2

[15] P. Konova, A. Naydenov, C. Venkov, D. Mehandjiev, D. Andreeva, T. Tabakova, J. Mol. Catal. A 213 (2004) 235-240

[16] X. Zou, S. Qi, Z. Suo, L. An, F. Li, Catal.Commun. 8 (2007) 784-788

[17] A. Russell, WS. Epling, Catal. Rev. Sci. Eng. 53 (2011) 337–423[18] J.C. Summers, L.L. Hegedus, J. Catal. 51(1978) 185–192

[19] R.M. Heck, R.J. Farrauto, Appl. Catal. A 221 (2001) 443–457

[20] H.S. Gandhi, G.W. Graham, R.W. McCabe, J. Catal. 216 (2003) 433–442

[21] J.C. Summers, J.F. Skowron, M. Miller , SAE Paper (1993) 930386

[22] D. Lindner, E.X. Lox, R. van Yperen, , K. Ostgathe, SAE Paper(1996) 960802

[23] C.F. Cullis, B.M. Willatt, J. Catal. 83(1983) 267–285

[24] Y.-F. Yu Yao, J. Catal. 87 (1984)152 –162.

[25] C. Wang, E. Sasmaz, C. Wen, J. Lauterbach, Catal. Today 258 (2015) 481–486

[26] H.S. Gandhi, M. Shelef, Appl. Catal. 77(1991) 175–186

[27] G. T. Drozd, Y. Zhao, G. Saliba, B. Frodin, C. Maddox, R. J. Weber, A. H. Goldstein, Environ. Sci. Technol. 50 (2016) 13592-13599.

[28] J. C. Summers, J. E. Sawyer, A. C. Frost, ACS Symp. Pap. 495 (1992) 98-114

[29] M. Kim, E. Kyriakidou, J. Choi, T. Toops, A. Binder, C. Thomas, J. Parks II, V. Schwartz, J. Chen, D. Hensley, Appl. Catal. B 187 (2016) 181–194

[30] A. Binder, T. Toops, R. Unocic, J. Parks II, S. Dai, Angew. Chem. Int. Ed. 54 (2015) 13263 –13267

[31] H. Muraki, H. Shinjoh, Y.Fujitani, Appl. Catal. 22 (1986) 325–335

[32] H.S. Gandhi, A.G. Piken , M. Shelef, R.G. Delosh, SAE Paper (1976) 760201

[33] J. Wu, L. Zeng, D. Cheng, F. Chen, X. Zhan, J. Gong, Chinese J. Catal. 37 (2016) 83-90

[34] X. Liu, P. Ning, L. Xu, Q. Liu, Z. Song, Q. Zhang, RSC Adv. 6 (2016) 41181-41188

[35] C. Du, G.Lu, Y. Guo, Y. Guo, X. Q. Gong, ACS Omega, 1(2016)118-126

[36] H.C. Yao, Appl. Surf. Sci. 19(1984) 398-406

[37] J. Wang, M. Shen, J. Wang, W. Wang, J. Rare Earth 29 (2011) 217–224

[38] Z. Han, J. Wang, H. Yan, M. Shen, J. Wang, W. Wang, M. Yang, Catal. Today 158, (2010) 481–489

[39] M. Ozawa, J. Alloy. Comp. 275–277 (1998) 886–890

[40] G.R. Rao, P. Fornasiero, R. Di Monte, J. Kašpar, G. Vlaic, G. Balducci, S. Meriani, G. Gubitosa, A. Cremona, M. Graziani, J. Catal. 162(1996) 1–9

[41] M. Ozawa, K. Matuda, S. Suzuki, J. Alloy. Compd. 303 (2000) 56–59

[42] S. Royer, D. Duprez, ChemCatChem 3 (2011) 24–65

[43] J. Singh, M. Nachtegaal, E. Alayon, J. St ̧tzel, J. A.Bokhoven, ChemCatChem 2 (2010) 653 –657

[44] H. C. Yao, Y. F. Yu Yao, J. Catal. 86(1984) 254 –265.

[45] G. Ercolino, P. Stelmachowski, G. Grzybek, A. Kotarba, S. Specchia, Appl. Catal. B 206 (2017) 712-725

[46] L.J. Alemany, F. Berti, G. Busca, G. Ramis, D. Robba, G. P. Toledo, M. Trombetta, Appl. Catal. B 10(1996) 299-311

[47] N. Topsoe, H. Topsoe, J.A. Dumesic, J.Catal. 151(1995)226-240

[48] B. Ramachandran, R. G. Herman, S. Choi, H. G. Stenger, C. E. Lyman, J. W. Sale, , Catal. Today 55(2000) 281-290

[49] A. Grossale, I. Nova, E. Tronconi, D. Chatterjee, M. Weibel, J. Catal. 256 (2008) 312-322

[50] H. Sjovall, L. Olsson, E. Fridell, R. J. Blint, Appl. Catal. B 64 (2006) 180-188

[51] G. Busca, L. Lietti, G. Ramis, F. Berti, Appl. Catal. B 18 (1998) 1-36

[52] J.P. Dunn, P. R. Koppula, H. G. Stenger, I. E. Wachs, , Appl. Catal. B 19 (1998) 103-117

[53] K. Rahkamaa-Tolonen, T. Maunula, M. Lomma, M. Huuhtanen, R. L. Keiski, Catal. Today 100 (2005) 217-222

[54] R.Q. Long, R.T. Yang, J. Am. Chem. Soc. 121 (1999) 5595

[55] A.Z. Ma, W. Grunert, Chem. Commun. (1999) 71

[56] G. Centi, C. Nigro, S. Perathoner, G. Stella, Catal. Today 17 (1993) 159-166

[57] J.H. Baik, S. D. Yim, I. S. Nam, Y. S. Mok, J. H. Lee, B. K. Cho, S. H. Oh, Top. Catal. 30 (2004) 37-41

[58] M. Richter, A. Trunschke, U. Bentrup, K. W. Brzezinka, E. Schreier, M. Schneider, R. Fricke, J. Catal. 206 (2002) 98-113

[59] G. Carja, Y. Kameshima, K.Okada, C. D. Madhusoodana, Appl. Catal. B 73 (2007) 60-64

[60] E. Ito, R. J. Hultermans, P. M. Lugt, M. H. W. Burgers, M. S. Rigutto, H. Van Bekkum, C. M. Van den Bleek, Appl. Catal. B 4 (1994) 95-104

[61] R.A. Grinsted, H. W. Jen, C. N. Montreuil, M. J. Rokosz, M. Shelef, Zeolites 13 (1993) 602–606.

[62] K.C.C. Kharas, Appl. Catal. B 2 (1993) 207-224

[63] S. Matsumoto, K. Yokota, H. Doi, M. Kimura, K. Sekizawa, S. Kasahara, Catal. Today 22 (1994) 127–146.

[64] T. Tanabe, T. Iijima, A. Koiwai, J. Mizuno, K. Yokota, A. Isogai, Appl. Catal. B 6 (1995) 145-153

[65] J.Y. Yan, W.M.H. Sachtler, H.H. Kung, Catal. Today 33 (1997) 279-290

[66] M. Berggrund, H. H. Ingelsten, M. Skoglundh, A. E. Palmqvist, Catal. Lett. 130 (2009) 79-85

[67] D. W. Fickel, E. D'Addio, J. A. Lauterbach, R. F. Lobo, Appl. Catal. B 102 (2011) 441-448

[68] J. Kwak, R. G. Tonkyn, D. H. Kim, J. Szanyi, C. H. Peden, J. Catal. 275 (2010) 187-190

[69] X. Yang, Z. Wu, M. Moses-Debusk, D. R. Mullins, S. M. Mahurin, R. A. Geiger, C. K. Narula, J. Phys. Chem. C 116 (2012) 23322-23331

[70] U. Deka, A. Juhin, E. A. Eilertsen, H. Emerich, M. A. Green, S. T. Korhonen, A. M. Beale, J. Phys. Chem. C 116 (2012) 4809-4818

[71] H. Praliaud, S. Mikhailenko, Z. Chajar, M. Primet, Appl. Catal., B 16 (1998) 359-374

[72] K. Mathisen, M. Stockenhuber, D. G. Nicholson, Phys. Chem. Chem. Phys. 11 (2009) 5476-5488

[73] V. F. Kispersky, A. J. Kropf, F. H. Ribeiro, J. T. Miller, Phys. Chem. Chem. Phys. 14 (2012) 2229-2238

[74] P. Vanelderen, J. Vancauwenbergh, B. F. Sels, R. A. Schoonheydt, Coord. Chem. Rev. 257 (2013) 483-494

[75] S.M. Seo, W.T. Lim, K. Seff, J. Phys. Chem. C 116 (2012) 13985-13996

[76] F. Gao, Y. Wang, N. Washton, M. Kollár, J. Szanyi, C. Peden, ACS Catal. 5 (2015) 6780-6791

[77] M. Shelef, R.W. McCabe, Catal. Today 62 (2000) 35–50

[78] EPA, https://www3.epa.gov/airquality/carbonmonoxide/

[79] E. J. Peterson, A. T. DeLaRiva, S. Lin, R. S. Johnson, H. Guo, J. T. Miller, J. Kwak, C, Peden, B. Kiefer, L.F. Allard, F, H. Ribeiro, A. K. Datye, Nature Commun. 5 (2014) 4885-4896

[80]C. Dardiotis, G. Martini, A. Marotta, U. Manfredi, Appl. Energy, 111 (2013) 468-478

[81] J.C. Summers, S.A. Ausen, J. Catal. 58 (1979) 131-143.

[82] G. B. Balazs, R. S. Glass, Solid State Ionics, 76 (1995) 155-162.

[83] M.S. Hegde, P. Bera, Catal. Today 253 (2015) 40–50.

[84] D.O. Scanlon, B. J. Morganw, G. W. Watson, Phys. Chem. Chem. Phys. 13 (2011) 4279–4284.

[85] S. Colussi, A. Gayen, M. F. Camellone, M. Boaro, J. Llorca, S. Fabris, A. Trovarelli, Angew. Chem. Int. Ed. 48 (2009) 8481–8484.

[86] S. Hinokuma, H. Fujii, M. Okamoto, K. Ikeue, M. Machida, Chem. Mater. 22 (2010) 6183–6190.

[87] R. V. Gulyaev, T. Kardash, S. E. Malykhin, O. A. Stonkus, A. S. Ivanova, A. I. Boronin, Phys. Chem. Chem. Phys. 16 (2014) 13523- 13539.

[88] J. A. Kurzman, L. M. Misch, R. Seshadri, Dalton Trans. 42 (2013) 14653-14667.

[89] A. Neitzel, A. Figueroba, Y. Lykhach, T. Skála, M. Vorokhta, N. Tsud, S. Mehl, K. Ševčíková, K. C. Prince, K. M. Neyman, V. Matolín, J. Libuda, J. Phys. Chem. C 120 (2016) 9852−9862.

[90] Y. Lykhach, A. Figueroba, M. Camellone, A. Neitzel, T. Skála, F. R. Negreiros, M. Vorokhta, N. Tsud, K. C. Prince, S. Fabris, K. M. Neyman, V. Matolín, J. Libuda, Phys. Chem. Chem. Phys. 18 (2016) 7672-7679.

[91] L. Meng, A.P. Jia, J.Q. Lu, L.F. Luo, W.X. Huang, M.F. Luo, J. Phys. Chem. C 115 (2011) 19789–19796.

[92] Y.Zhou, , N. J. Lawrence, , T. S. Wu, , J. Liu, , P. Kent, , Y. L. Soo, , & C. L. Cheung, . ChemCatChem, 6(2014) 2937-2946.

[93] H.S. Gandhi, G.W. Graham, R.W. McCabe, J. Catal. 216 (2003) 433–442.

[94] R.V. Gulyaev A.I. Stadnichenko, E.M. Slavinskaya, A.S. Ivanova, S.V. Koscheev, A.I. Boronin, Appl. Catal. A 439 (2012) 41-50.

[95] L. Meng, J.J. Lin, Z.Y. Pu, L.F. Luo, A.P. Jia, W.X. Huang, M.F. Luo, J.Q. Lu, Appl. Catal. B 119 (2012) 117-122.

[96] R.V. Gulyaev, E.M. Slavinskaya, S.A. Novopashin, D.V. Smovzh, A.V. Zaikovskii, D.Yu. Osadchii, O.A. Bulavchenko, S.V. Korenev, A.I. Boronin, Appl. Catal. B 147 (2014) 132-143.

[97] M.S. Jin, J.N. Park, J.K. Shon, J.H. Kim, Z.H. Li, Y.K. Park, J. M. Kim Catal. Today 185 (2012) 183-190.

[98] J.Y. Luo, M. Meng, X. Li, X.G. Lia, Y.Q. Zha, T.D. Hub, Y.N. Xie, J. Zhang J. Catal. 254 (2008) 310-324.

[99] H.Q. Zhu, Z.F. Qin, W.J Shan, W.J. Shen, J.G Wang, J. Catal. 233 (2005) 41–50

[100] M.F. Luo, Z.Y. Hou, X.X.Yuan, X.M. Zheng, Catal. Lett. 50 (1998)205-209.

[101] D. B. Vasilchenko, R. V. Gulyaev, E. M. Slavinskaya, O. A. Stonkus, Y. V. Shubin, S. V. Korenev, A. I. Boronin, Catal. Commun. 73 (2016) 34-38.

[102] K. Krishna, A. Bueno-López, M. Makkee, J.A. Moulijn, Appl. Catal. B 75 (2007) 201–209.

[103] P. Fornasieroa, G. Balduccia, R. Di Montea, J. Kašpara, 1, V. Sergob, G. Gubitosac, A. Ferreroc, M. Graziania, J. Catal. 164 (1996) 173-183.

[104] H. He,H. X. Dai, L. H. Ng, K.W.Wong, C. T. Au, J. Catal. 206 (2002) 1-13

[105] X.F. Tang, Y.G. Li, X.M. Huang, Y.D. Xu, H.D. Zhu, J.G. Wang, W.J. Shen, Appl. Catal. B 62 (2006) 265-273.

[106] H.Z. Chang, J.H. Li, X.Y. Chen , L. Ma, S.J. Yang , J.W. Schwank, J.M. Hao, Catal. Commun. 27 (2012) 54–57.

[107] J.L. Ayastuy, A. Iglesias-González, M.A. Gutiérrez-Ortiz, Chem. Eng. J. 244 (2014) 372-381.

[108] J.Y. Luo, M. Meng, J.S. Yao, X.G. Li, Y.Q. Zha, X. Wang, T.Y. Zhang, Appl. Catal. B 87 (2009) 92-103.

[109] R. E. Jentoft, S. E. Deutsch, B. C. Gates, Rev. Sci. Instrum. 67 (1996) 2111−2112.

[110] B. Ravel, M. Newville, J. Synchrotron. Radiat. 12 (2005) 537–541.

[111] K. R. Priolkar, P. Bera, P. R. Sarode, M. S. Hegde, S. Emura, R. Kumashiro, N. P. Lalla, Chem. Mater. 14 (2002) 2120-2128.

[112] A.I. Boronin, E.M. Slavinskaya, I.G. Danilova, R.V. Gulyaev, Y.I. Amosov, P.A. Kuznetsov, I.A. Polukhina, S.V. Koscheev, V.I. Zaikovskii, A.S. Noskov, Catal. Today 144 (2009) 201–211.

[113] B. Corain, G. Schmid, Metal Nanoclusters in Catalysis and Materials Science: The Issue of Size Control, Elsevier, 2008.

[114] S. Penner, P. Bera, S. Pedersen, L. T. Ngo, J. Harris, C.T. Campbell, J. Phys. Chem. B 110 (2006) 24577-24584.

[115] W. F. Engelhoff, Surf. Sci. Rep. 6 (1987) 253-415

[116] C. I. Hiley, J. M. Fisher, D. Thompsett, R. J. Kashtiban, J. Sloan, R. I. Walton, J. Mater. Chem. A, 3 (2015) 13072-13079.

[117] S. Imamura, M. Shono, N. Okamoto, A. Hamada, S. Ishida, Appl. Catal. A 142 (1996) 279-288.

[118] W. Cen, Y. Liu, Z. Wu, H. Wang, X. Weng, Phys. Chem. Chem. Phys. 14 (2012) 5769–5777.

[119] A. Satsuma, K. Osaki, M. Yanagihara, J. Ohyama, K. Shimizu, Appl. Catal. B 132 (2013) 511–518.

[120] T. Ressler, J. Wong, J. Roos, I. L. Smith, Environ. Sci. Technol. 34 (2000) 950–958.

[121] C. Li, Y. Sakata, T. Arai, K. Domen, K. Maruya, T. Onishi, J. Chem. Soc., Faraday Trans. I, 85 (1989) 929-943.

[122] W. Lin, A. A. Herzing, C. J. Kiely, I. E. Wachs, J. Phys. Chem. C 112 (2008) 5942-5951.

[123] A. Bruix, J.A. Rodriguez, P. J. Ramírez, S. D. Senanayake, J. Evans, J. B. Park, D. Stacchiola, P. Liu, J. Hrbek, F. Illas, J. Am. Chem. Soc. 134 (2012) 8968−8974.

[124]Y. Choi, M. Scott, T. Söhnel, H. Idriss, Phys. Chem. Chem. Phys. 16 (2014) 22588-22599.

[125] J. A. Farmer, C. T. Campbell, Science 329 (2010) 933–936

[126] J. Y. Luo, M. Meng, J. S. Yao, X. G. Li, Y. Q. Zha, X. Wang, T.Y. Zhang, Appl. Catal. B 87 (2009) 92–103.

[127] X.F. Tang, J.L. Chen, X.M. Huang, Y.D. Xu, W.J. Shen. Appl. Catal. B 81 (2008) 115–121.

[128] P. Zhang, H. Lu, Y. Zhou, L. Zhang, Z. Wu, S. Yang, H. Shi, Q. Zhu, Y. Chen, S. Dai, Nature Commun. 6 (2015) 8446-8455.

[129] Y. Su, Z. Tang, W. Han, P. Zhang, Y. Song, G. Lu, Cryst. Eng. Comm., 16 (2014) 5189-5197.

[130] L. Lan, S. Chen, M. Zhao, M. Gong, Y. Chen, J. Mol. Catal. A 394 (2014) 10–21.

[131] S. Sharma, S. Hilaire, J.M. Vohs, R.J. Gorte, H. W. Jen, J. Catal. 90 (2000) 199-204.

[132] C. Chen, J.J. Cao, M. Cargnello, P. Fornasiero, R. J. Gorte, J. Catal. 306 (2013) 109–115.

[133] P. Konova, A. Naydenov, C. Venkov, D. Mehandjiev, D. Andreeva, T. Tabakova, J. Mol. Catal. A: Chemical 213 (2004) 235–240.

[134] R. Kopelent, J. Bokhoven, J. Szlachetko, J. Edebeli, C. Paun, M. Nachtegaal, O. V. Safonova, Angew. Chem.127 (2015) 8852-8855.

[135] M.V. Twigg, Appl. Catal. B 70 (2007) 2–15

[136] A. Papavasiliou, A. Tsetsekou, V. Matsouka, M. Konsolakis, I.V. Yentekakis, N. Boukos, Appl. Catal. B 90 (2009) 162–174

[137]H.Z. Chang, J.H. Li, X.Y. Chen , L. Ma, S.J. Yang , J.W. Schwank, J.M. Hao, Catal. Commun. 27 (2012) 54–57.

[138] T.J. Toops, K. Nguyen, A.L. Foster, B.G. Bunting, N.A. Ottinger, J.A. Pihl, E.W. Hagaman, J. Jiao, Catal. Today 151 (2010) 257-265

[139] Y. Cheng, C. Lambert, D.H. Kim, J.H. Kwak, S.J. Cho, C. Peden, Catal.Today 151 (2010) 266-270

[140] C. He, Y. Wang, Y. Cheng, C.K. Lambert, R.T. Yang, Appl. Catal. A 368 (2009) 121-126

[141] The Advanced Combustion and Emission Control (ACEC) Technical Team, "Low Temperature Oxidation Catalyst Test Protocol" 2015

[142] R. Caporali, S. Chansai, R. Burch, J. J. Delgado, A. Goguet, C. Hardacre, L. Mantarosie, D. Thompsett, Appl. Catal. B 147 (2014) 764–769

[143] Al Harbi, M., Hayes, R., Votsmeier, M., Epling, W. S., Can. J. Chem. Eng. 90, 1527–1538 (2012)

[144] F. Diehl, J. Barbier, D. Duprez, I. Guibard, G. Mabilon, Appl. Catal. B 95 (2010) 217−227

[145] S. E. Voltz, C. R. Morgan, D. Liederman, S. M. Jacob, Ind. Eng. Chem. Prod. Res. Develop. 12 (1973) 294−301

[146] Z. Hu, X. Liu, D. Meng, Y. Guo, Y. Guo, G. Lu, ACS Catal. 6 (2016) 2265−2279

[147] W. Lin, A. A. Herzing, C. J. Kiely, I. E. Wachs, J. Phys. Chem. C 112 (2008) 5942-5951

[148] A. Martnez-Arias, M. Fernndez-Garca, A. Inglesias-Juez, A.B. Hungra, J. A. Anderson, J. C. Conesa, J. Soria, Appl. Catal. B 31(2001) 51–60

[149] H. Yang G.X. Wei, X.Q. Wang, F. Lin, J. Wang, M.Q. Shen, Catal.Commun. 36 (2013) 5–9

[150] R. Caporali, S. Chansai, R. Burch, J. J. Delgado, A. Goguet, C. Hardacre, L. Mantarosie, D. Thompsett, Appl. Catal. B 147 (2014) 764–769

[151] Q. Xu, K. C. Kharas, B. J. Croley, A. K. Datye, Top. Catal 55 (2012) 8–83

[152] X.Y. Chen, Y.S. Cheng, C. Y. Seo, J. W. Schwank,R. W. McCabe Appl. Catal. B 163 (2015) 499–509

[153] H. Chang, X.Y. Chen, J.H. Li, L. Ma, C.Z. Wang, C.X. Liu, J.W. Schwank, J.M. Hao, Environ. Sci. Technol. 47 (2013) 5294−5301

[154] V. E. Herinch, P. A. Cox, The Surface Science of Metal, Cambridge University Press, Cambridge, 1996.

[155] P. Hu, Z. Huang, Z. Amghouz, M. Makkee, F. Xu, F. Kapteijn, A. Dikhtiarenko, Y. Chen, X. Gu, X.Tang, Angew. Chem. Int. Ed. 53 (2014) 3418

[156] N. Acerbi, S. C. E. Tsang, G. Jones, S. Golunski, P. Collier, Angew. Chem. 2013, 125, 7891

[157] T. Schalow, M. Laurin, B. Brandt, S. Schauermann, S. Guimond, H. Kuhlenbeck, D. E.Starr , S.K.Shaikhutdinov , J. Libuda, H. Freund, Angew. Chem. Int. Ed. 44 (2005) 7601-7605

[158] C. Wang, E. Sasmaz, C. Wen, J. Lauterbach, Appl. Catal. B 206 (2017) 1–8

[159] Y Zhai, X Ma, H Mao, W Shao, L Xu, Y.He, Y.Qian, Adv. Electron. Mater. 6 (2015) 1

[160] X. Mou, X. Wei, Y. Li, W. Shen, CrystEngComm, 14 (2012) 5107–5120

[161] L. Li, G. Li, Y. Yuan, RSC Adv. 5 (2015) 4586-4591

[162] K.Patrick, M. Friedrich, D. Teschner, F. Girgsdies, T. Lunkenbein, R.N. d'Alnoncourt, M. Behrens, R. Schlögl. Appl. Catal. A 502 (2015) 8-17

[163] G.Qi, R.T. Yang, J. Catal. 217 (2003) 434-441

[164] J. Li, H. Chang, L. Ma, J. Hao, R.T. Yang, Catal. Today. 175 (2011) 147-156

[165] G. Qi, R.T. Yang, R. Chang, Appl. Catal. B 51 (2004) 93-106

Appendix A – List of publication

Chao Wang, Erdem Sasmaz, Cun Wen, Jochen Lauterbach, "Superior oxygen transfer ability of Pd/MnO_x-CeO_2 for enhanced low temperature CO oxidation activity", ***Applied Catalysis B: Environmental***, 2017 (206) 1–8

Chao Wang, Andrew J. Binder, Todd J. Toops, Jochen Lauterbach, Erdem Sasmaz, "Evaluation of Mn and Sn modified Pd-Ce based catalysts for low-temperature diesel exhaust oxidation", ***Emission Control Science and Technology***, 2017 (3) 37–46

Chao Wang, Erdem Sasmaz, Cun Wen, Jochen Lauterbach, "Pd supported on SnO_2-MnO_x-CeO_2 catalysts for low temperature CO oxidation", ***Catalysis Today***, 2015 (258) 481–486

Erdem Sasmaz, **Chao Wang**, Jochen Lauterbach, "In-situ spectroscopic investigation of Pd local structure over Pd/CeO_2 and Pd/MnO_x-CeO_2 during CO oxidation" ***Journal of Materials Chemistry A***, under review, 2017

Appendix B – Permission to reprint

ELSEVIER LICENSE
TERMS AND CONDITIONS

Mar 29, 2017

This Agreement between Chao Wang ("You") and Elsevier ("Elsevier") consists of your license details and the terms and conditions provided by Elsevier and Copyright Clearance Center.

License Number	4078391317701
License date	Mar 29, 2017
Licensed Content Publisher	Elsevier
Licensed Content Publication	Applied Catalysis B: Environmental
Licensed Content Title	Superior oxygen transfer ability of Pd/MnOx-CeO2 for enhanced low temperature CO oxidation activity
Licensed Content Author	Chao Wang,Cun Wen,Jochen Lauterbach,Erdem Sasmaz
Licensed Content Date	5 June 2017
Licensed Content Volume	206
Licensed Content Issue	n/a
Licensed Content Pages	8
Start Page	1
End Page	8
Type of Use	reuse in a thesis/dissertation
Portion	full article
Format	both print and electronic
Are you the author of this Elsevier article?	Yes
Will you be translating?	No
Order reference number	
Title of your thesis/dissertation	Development of novel catalysts for air pollution control
Expected completion date	Apr 2017
Estimated size (number of pages)	150
Elsevier VAT number	GB 494 6272 12
Requestor Location	Chao Wang 541 Main St Room 136 COLUMBIA, SC 29201 United States Attn: Chao Wang
Publisher Tax ID	98-0397604
Total	0.00 USD
Terms and Conditions	

INTRODUCTION

1. The publisher for this copyrighted material is Elsevier. By clicking "accept" in connection with completing this licensing transaction, you agree that the following terms and conditions apply to this transaction (along with the Billing and Payment terms and conditions established by Copyright Clearance Center, Inc. ("CCC"), at the time that you opened your Rightslink account and that are available at any time at http://myaccount.copyright.com).

GENERAL TERMS

2. Elsevier hereby grants you permission to reproduce the aforementioned material subject to the terms and conditions indicated.

3. Acknowledgement: If any part of the material to be used (for example, figures) has appeared in our publication with credit or acknowledgement to another source, permission must also be sought from that source. If such permission is not obtained then that material may not be included in your publication/copies. Suitable acknowledgement to the source must be made, either as a footnote or in a reference list at the end of your publication, as follows:

"Reprinted from Publication title, Vol /edition number, Author(s), Title of article / title of chapter, Pages No., Copyright (Year), with permission from Elsevier [OR APPLICABLE SOCIETY COPYRIGHT OWNER]." Also Lancet special credit - "Reprinted from The Lancet, Vol. number, Author(s), Title of article, Pages No., Copyright (Year), with permission from Elsevier."

4. Reproduction of this material is confined to the purpose and/or media for which permission is hereby given.

5. Altering/Modifying Material: Not Permitted. However figures and illustrations may be altered/adapted minimally to serve your work. Any other abbreviations, additions, deletions and/or any other alterations shall be made only with prior written authorization of Elsevier Ltd. (Please contact Elsevier at permissions@elsevier.com). No modifications can be made to any Lancet figures/tables and they must be reproduced in full.

6. If the permission fee for the requested use of our material is waived in this instance, please be advised that your future requests for Elsevier materials may attract a fee.

7. Reservation of Rights: Publisher reserves all rights not specifically granted in the combination of (i) the license details provided by you and accepted in the course of this licensing transaction, (ii) these terms and conditions and (iii) CCC's Billing and Payment terms and conditions.

8. License Contingent Upon Payment: While you may exercise the rights licensed immediately upon issuance of the license at the end of the licensing process for the transaction, provided that you have disclosed complete and accurate details of your proposed use, no license is finally effective unless and until full payment is received from you (either by publisher or by CCC) as provided in CCC's Billing and Payment terms and conditions. If full payment is not received on a timely basis, then any license preliminarily granted shall be deemed automatically revoked and shall be void as if never granted. Further, in the event that you breach any of these terms and conditions or any of CCC's Billing and Payment terms and conditions, the license is automatically revoked and shall be void as if never granted. Use of materials as described in a revoked license, as well as any use of the materials beyond the scope of an unrevoked license, may constitute copyright infringement and publisher reserves the right to take any and all action to protect its copyright in the materials.

9. Warranties: Publisher makes no representations or warranties with respect to the licensed material.

10. Indemnity: You hereby indemnify and agree to hold harmless publisher and CCC, and their respective officers, directors, employees and agents, from and against any and all claims arising out of your use of the licensed material other than as specifically authorized pursuant to this license.

11. No Transfer of License: This license is personal to you and may not be sublicensed, assigned, or transferred by you to any other person without publisher's written permission.

12. No Amendment Except in Writing: This license may not be amended except in a writing signed by both parties (or, in the case of publisher, by CCC on publisher's behalf).
13. Objection to Contrary Terms: Publisher hereby objects to any terms contained in any purchase order, acknowledgment, check endorsement or other writing prepared by you, which terms are inconsistent with these terms and conditions or CCC's Billing and Payment terms and conditions. These terms and conditions, together with CCC's Billing and Payment terms and conditions (which are incorporated herein), comprise the entire agreement between you and publisher (and CCC) concerning this licensing transaction. In the event of any conflict between your obligations established by these terms and conditions and those established by CCC's Billing and Payment terms and conditions, these terms and conditions shall control.
14. Revocation: Elsevier or Copyright Clearance Center may deny the permissions described in this License at their sole discretion, for any reason or no reason, with a full refund payable to you. Notice of such denial will be made using the contact information provided by you. Failure to receive such notice will not alter or invalidate the denial. In no event will Elsevier or Copyright Clearance Center be responsible or liable for any costs, expenses or damage incurred by you as a result of a denial of your permission request, other than a refund of the amount(s) paid by you to Elsevier and/or Copyright Clearance Center for denied permissions.

LIMITED LICENSE

The following terms and conditions apply only to specific license types:
15. **Translation**: This permission is granted for non-exclusive world **English** rights only unless your license was granted for translation rights. If you licensed translation rights you may only translate this content into the languages you requested. A professional translator must perform all translations and reproduce the content word for word preserving the integrity of the article.
16. **Posting licensed content on any Website**: The following terms and conditions apply as follows: Licensing material from an Elsevier journal: All content posted to the web site must maintain the copyright information line on the bottom of each image; A hyper-text must be included to the Homepage of the journal from which you are licensing at http://www.sciencedirect.com/science/journal/xxxxx or the Elsevier homepage for books at http://www.elsevier.com: Central Storage: This license does not include permission for a scanned version of the material to be stored in a central repository such as that provided by Heron/XanEdu.
Licensing material from an Elsevier book: A hyper-text link must be included to the Elsevier homepage at http://www.elsevier.com . All content posted to the web site must maintain the copyright information line on the bottom of each image.

Posting licensed content on Electronic reserve: In addition to the above the following clauses are applicable: The web site must be password-protected and made available only to bona fide students registered on a relevant course. This permission is granted for 1 year only. You may obtain a new license for future website posting.
17. **For journal authors:** the following clauses are applicable in addition to the above:
Preprints:
A preprint is an author's own write-up of research results and analysis, it has not been peer-reviewed, nor has it had any other value added to it by a publisher (such as formatting, copyright, technical enhancement etc.).
Authors can share their preprints anywhere at any time. Preprints should not be added to or enhanced in any way in order to appear more like, or to substitute for, the final versions of articles however authors can update their preprints on arXiv or RePEc with their Accepted Author Manuscript (see below).
If accepted for publication, we encourage authors to link from the preprint to their formal publication via its DOI. Millions of researchers have access to the formal publications on ScienceDirect, and so links will help users to find, access, cite and use the best available

version. Please note that Cell Press, The Lancet and some society-owned have different preprint policies. Information on these policies is available on the journal homepage.
Accepted Author Manuscripts: An accepted author manuscript is the manuscript of an article that has been accepted for publication and which typically includes author-incorporated changes suggested during submission, peer review and editor-author communications.
Authors can share their accepted author manuscript:

- immediately
  - via their non-commercial person homepage or blog
  - by updating a preprint in arXiv or RePEc with the accepted manuscript
  - via their research institute or institutional repository for internal institutional uses or as part of an invitation-only research collaboration work-group
  - directly by providing copies to their students or to research collaborators for their personal use
  - for private scholarly sharing as part of an invitation-only work group on commercial sites with which Elsevier has an agreement
- After the embargo period
  - via non-commercial hosting platforms such as their institutional repository
  - via commercial sites with which Elsevier has an agreement

In all cases accepted manuscripts should:

- link to the formal publication via its DOI
- bear a CC-BY-NC-ND license - this is easy to do
- if aggregated with other manuscripts, for example in a repository or other site, be shared in alignment with our hosting policy not be added to or enhanced in any way to appear more like, or to substitute for, the published journal article.

Published journal article (JPA): A published journal article (PJA) is the definitive final record of published research that appears or will appear in the journal and embodies all value-adding publishing activities including peer review co-ordination, copy-editing, formatting, (if relevant) pagination and online enrichment.
Policies for sharing publishing journal articles differ for subscription and gold open access articles:
Subscription Articles: If you are an author, please share a link to your article rather than the full-text. Millions of researchers have access to the formal publications on ScienceDirect, and so links will help your users to find, access, cite, and use the best available version.
Theses and dissertations which contain embedded PJAs as part of the formal submission can be posted publicly by the awarding institution with DOI links back to the formal publications on ScienceDirect.
If you are affiliated with a library that subscribes to ScienceDirect you have additional private sharing rights for others' research accessed under that agreement. This includes use for classroom teaching and internal training at the institution (including use in course packs and courseware programs), and inclusion of the article for grant funding purposes.
Gold Open Access Articles: May be shared according to the author-selected end-user license and should contain a CrossMark logo, the end user license, and a DOI link to the formal publication on ScienceDirect.
Please refer to Elsevier's posting policy for further information.
18. **For book authors** the following clauses are applicable in addition to the above:
Authors are permitted to place a brief summary of their work online only. You are not allowed to download and post the published electronic version of your chapter, nor may you scan the printed edition to create an electronic version. **Posting to a repository:** Authors are permitted to post a summary of their chapter only in their institution's repository.

19. **Thesis/Dissertation**: If your license is for use in a thesis/dissertation your thesis may be submitted to your institution in either print or electronic form. Should your thesis be published commercially, please reapply for permission. These requirements include permission for the Library and Archives of Canada to supply single copies, on demand, of the complete thesis and include permission for Proquest/UMI to supply single copies, on demand, of the complete thesis. Should your thesis be published commercially, please reapply for permission. Theses and dissertations which contain embedded PJAs as part of the formal submission can be posted publicly by the awarding institution with DOI links back to the formal publications on ScienceDirect.

Elsevier Open Access Terms and Conditions

You can publish open access with Elsevier in hundreds of open access journals or in nearly 2000 established subscription journals that support open access publishing. Permitted third party re-use of these open access articles is defined by the author's choice of Creative Commons user license. See our open access license policy for more information.

Terms & Conditions applicable to all Open Access articles published with Elsevier:

Any reuse of the article must not represent the author as endorsing the adaptation of the article nor should the article be modified in such a way as to damage the author's honour or reputation. If any changes have been made, such changes must be clearly indicated.

The author(s) must be appropriately credited and we ask that you include the end user license and a DOI link to the formal publication on ScienceDirect.

If any part of the material to be used (for example, figures) has appeared in our publication with credit or acknowledgement to another source it is the responsibility of the user to ensure their reuse complies with the terms and conditions determined by the rights holder.

Additional Terms & Conditions applicable to each Creative Commons user license:

CC BY: The CC-BY license allows users to copy, to create extracts, abstracts and new works from the Article, to alter and revise the Article and to make commercial use of the Article (including reuse and/or resale of the Article by commercial entities), provided the user gives appropriate credit (with a link to the formal publication through the relevant DOI), provides a link to the license, indicates if changes were made and the licensor is not represented as endorsing the use made of the work. The full details of the license are available at http://creativecommons.org/licenses/by/4.0.

CC BY NC SA: The CC BY-NC-SA license allows users to copy, to create extracts, abstracts and new works from the Article, to alter and revise the Article, provided this is not done for commercial purposes, and that the user gives appropriate credit (with a link to the formal publication through the relevant DOI), provides a link to the license, indicates if changes were made and the licensor is not represented as endorsing the use made of the work. Further, any new works must be made available on the same conditions. The full details of the license are available at http://creativecommons.org/licenses/by-nc-sa/4.0.

CC BY NC ND: The CC BY-NC-ND license allows users to copy and distribute the Article, provided this is not done for commercial purposes and further does not permit distribution of the Article if it is changed or edited in any way, and provided the user gives appropriate credit (with a link to the formal publication through the relevant DOI), provides a link to the license, and that the licensor is not represented as endorsing the use made of the work. The full details of the license are available at http://creativecommons.org/licenses/by-nc-nd/4.0.

Any commercial reuse of Open Access articles published with a CC BY NC SA or CC BY NC ND license requires permission from Elsevier and will be subject to a fee.

Commercial reuse includes:

- Associating advertising with the full text of the Article
- Charging fees for document delivery or access
- Article aggregation
- Systematic distribution via e-mail lists or share buttons

Posting or linking by commercial companies for use by customers of those companies.

20. **Other Conditions**:

v1.9

Questions? customercare@copyright.com or +1-855-239-3415 (toll free in the US) or +1-978-646-2777.

ELSEVIER LICENSE
TERMS AND CONDITIONS

Mar 29, 2017

This Agreement between Chao Wang ("You") and Elsevier ("Elsevier") consists of your license details and the terms and conditions provided by Elsevier and Copyright Clearance Center.

License Number	4078400074193
License date	Mar 29, 2017
Licensed Content Publisher	Elsevier
Licensed Content Publication	Catalysis Today
Licensed Content Title	Pd supported on SnO2–MnOx–CeO2 catalysts for low temperature CO oxidation
Licensed Content Author	Chao Wang,Erdem Sasmaz,Cun Wen,Jochen Lauterbach
Licensed Content Date	1 December 2015
Licensed Content Volume	258
Licensed Content Issue	n/a
Licensed Content Pages	6
Start Page	481
End Page	486
Type of Use	reuse in a thesis/dissertation
Intended publisher of new work	other
Portion	full article
Format	both print and electronic
Are you the author of this Elsevier article?	Yes
Will you be translating?	No
Order reference number	
Title of your thesis/dissertation	Development of novel catalysts for air pollution control
Expected completion date	Apr 2017
Estimated size (number of pages)	150
Elsevier VAT number	GB 494 6272 12
Requestor Location	Chao Wang 541 Main St Room 136 COLUMBIA, SC 29201 United States Attn: Chao Wang
Publisher Tax ID	98-0397604
Total	0.00 USD

Terms and Conditions

INTRODUCTION

1. The publisher for this copyrighted material is Elsevier. By clicking "accept" in connection with completing this licensing transaction, you agree that the following terms and conditions apply to this transaction (along with the Billing and Payment terms and conditions established by Copyright Clearance Center, Inc. ("CCC"), at the time that you opened your Rightslink account and that are available at any time at http://myaccount.copyright.com).

GENERAL TERMS

2. Elsevier hereby grants you permission to reproduce the aforementioned material subject to the terms and conditions indicated.

3. Acknowledgement: If any part of the material to be used (for example, figures) has appeared in our publication with credit or acknowledgement to another source, permission must also be sought from that source. If such permission is not obtained then that material may not be included in your publication/copies. Suitable acknowledgement to the source must be made, either as a footnote or in a reference list at the end of your publication, as follows:

"Reprinted from Publication title, Vol /edition number, Author(s), Title of article / title of chapter, Pages No., Copyright (Year), with permission from Elsevier [OR APPLICABLE SOCIETY COPYRIGHT OWNER]." Also Lancet special credit - "Reprinted from The Lancet, Vol. number, Author(s), Title of article, Pages No., Copyright (Year), with permission from Elsevier."

4. Reproduction of this material is confined to the purpose and/or media for which permission is hereby given.

5. Altering/Modifying Material: Not Permitted. However figures and illustrations may be altered/adapted minimally to serve your work. Any other abbreviations, additions, deletions and/or any other alterations shall be made only with prior written authorization of Elsevier Ltd. (Please contact Elsevier at permissions@elsevier.com). No modifications can be made to any Lancet figures/tables and they must be reproduced in full.

6. If the permission fee for the requested use of our material is waived in this instance, please be advised that your future requests for Elsevier materials may attract a fee.

7. Reservation of Rights: Publisher reserves all rights not specifically granted in the combination of (i) the license details provided by you and accepted in the course of this licensing transaction, (ii) these terms and conditions and (iii) CCC's Billing and Payment terms and conditions.

8. License Contingent Upon Payment: While you may exercise the rights licensed immediately upon issuance of the license at the end of the licensing process for the transaction, provided that you have disclosed complete and accurate details of your proposed use, no license is finally effective unless and until full payment is received from you (either by publisher or by CCC) as provided in CCC's Billing and Payment terms and conditions. If full payment is not received on a timely basis, then any license preliminarily granted shall be deemed automatically revoked and shall be void as if never granted. Further, in the event that you breach any of these terms and conditions or any of CCC's Billing and Payment terms and conditions, the license is automatically revoked and shall be void as if never granted. Use of materials as described in a revoked license, as well as any use of the materials beyond the scope of an unrevoked license, may constitute copyright infringement and publisher reserves the right to take any and all action to protect its copyright in the materials.

9. Warranties: Publisher makes no representations or warranties with respect to the licensed material.

10. Indemnity: You hereby indemnify and agree to hold harmless publisher and CCC, and their respective officers, directors, employees and agents, from and against any and all claims arising out of your use of the licensed material other than as specifically authorized pursuant to this license.

11. No Transfer of License: This license is personal to you and may not be sublicensed, assigned, or transferred by you to any other person without publisher's written permission.
12. No Amendment Except in Writing: This license may not be amended except in a writing signed by both parties (or, in the case of publisher, by CCC on publisher's behalf).
13. Objection to Contrary Terms: Publisher hereby objects to any terms contained in any purchase order, acknowledgment, check endorsement or other writing prepared by you, which terms are inconsistent with these terms and conditions or CCC's Billing and Payment terms and conditions. These terms and conditions, together with CCC's Billing and Payment terms and conditions (which are incorporated herein), comprise the entire agreement between you and publisher (and CCC) concerning this licensing transaction. In the event of any conflict between your obligations established by these terms and conditions and those established by CCC's Billing and Payment terms and conditions, these terms and conditions shall control.
14. Revocation: Elsevier or Copyright Clearance Center may deny the permissions described in this License at their sole discretion, for any reason or no reason, with a full refund payable to you. Notice of such denial will be made using the contact information provided by you. Failure to receive such notice will not alter or invalidate the denial. In no event will Elsevier or Copyright Clearance Center be responsible or liable for any costs, expenses or damage incurred by you as a result of a denial of your permission request, other than a refund of the amount(s) paid by you to Elsevier and/or Copyright Clearance Center for denied permissions.

LIMITED LICENSE

The following terms and conditions apply only to specific license types:
15. **Translation**: This permission is granted for non-exclusive world **English** rights only unless your license was granted for translation rights. If you licensed translation rights you may only translate this content into the languages you requested. A professional translator must perform all translations and reproduce the content word for word preserving the integrity of the article.
16. **Posting licensed content on any Website**: The following terms and conditions apply as follows: Licensing material from an Elsevier journal: All content posted to the web site must maintain the copyright information line on the bottom of each image; A hyper-text must be included to the Homepage of the journal from which you are licensing at http://www.sciencedirect.com/science/journal/xxxxx or the Elsevier homepage for books at http://www.elsevier.com; Central Storage: This license does not include permission for a scanned version of the material to be stored in a central repository such as that provided by Heron/XanEdu.
Licensing material from an Elsevier book: A hyper-text link must be included to the Elsevier homepage at http://www.elsevier.com . All content posted to the web site must maintain the copyright information line on the bottom of each image.

Posting licensed content on Electronic reserve: In addition to the above the following clauses are applicable: The web site must be password-protected and made available only to bona fide students registered on a relevant course. This permission is granted for 1 year only. You may obtain a new license for future website posting.
17. **For journal authors:** the following clauses are applicable in addition to the above:
Preprints:
A preprint is an author's own write-up of research results and analysis, it has not been peer-reviewed, nor has it had any other value added to it by a publisher (such as formatting, copyright, technical enhancement etc.).
Authors can share their preprints anywhere at any time. Preprints should not be added to or enhanced in any way in order to appear more like, or to substitute for, the final versions of articles however authors can update their preprints on arXiv or RePEc with their Accepted Author Manuscript (see below).

If accepted for publication, we encourage authors to link from the preprint to their formal publication via its DOI. Millions of researchers have access to the formal publications on ScienceDirect, and so links will help users to find, access, cite and use the best available version. Please note that Cell Press, The Lancet and some society-owned have different preprint policies. Information on these policies is available on the journal homepage.
Accepted Author Manuscripts: An accepted author manuscript is the manuscript of an article that has been accepted for publication and which typically includes author-incorporated changes suggested during submission, peer review and editor-author communications.
Authors can share their accepted author manuscript:

- immediately
  - via their non-commercial person homepage or blog
  - by updating a preprint in arXiv or RePEc with the accepted manuscript
  - via their research institute or institutional repository for internal institutional uses or as part of an invitation-only research collaboration work-group
  - directly by providing copies to their students or to research collaborators for their personal use
  - for private scholarly sharing as part of an invitation-only work group on commercial sites with which Elsevier has an agreement
- After the embargo period
  - via non-commercial hosting platforms such as their institutional repository
  - via commercial sites with which Elsevier has an agreement

In all cases accepted manuscripts should:

- link to the formal publication via its DOI
- bear a CC-BY-NC-ND license - this is easy to do
- if aggregated with other manuscripts, for example in a repository or other site, be shared in alignment with our hosting policy not be added to or enhanced in any way to appear more like, or to substitute for, the published journal article.

Published journal article (JPA): A published journal article (PJA) is the definitive final record of published research that appears or will appear in the journal and embodies all value-adding publishing activities including peer review co-ordination, copy-editing, formatting, (if relevant) pagination and online enrichment.
Policies for sharing publishing journal articles differ for subscription and gold open access articles:
Subscription Articles: If you are an author, please share a link to your article rather than the full-text. Millions of researchers have access to the formal publications on ScienceDirect, and so links will help your users to find, access, cite, and use the best available version.
Theses and dissertations which contain embedded PJAs as part of the formal submission can be posted publicly by the awarding institution with DOI links back to the formal publications on ScienceDirect.
If you are affiliated with a library that subscribes to ScienceDirect you have additional private sharing rights for others' research accessed under that agreement. This includes use for classroom teaching and internal training at the institution (including use in course packs and courseware programs), and inclusion of the article for grant funding purposes.
Gold Open Access Articles: May be shared according to the author-selected end-user license and should contain a CrossMark logo, the end user license, and a DOI link to the formal publication on ScienceDirect.
Please refer to Elsevier's posting policy for further information.
18. **For book authors** the following clauses are applicable in addition to the above:
Authors are permitted to place a brief summary of their work online only. You are not

allowed to download and post the published electronic version of your chapter, nor may you scan the printed edition to create an electronic version. **Posting to a repository:** Authors are permitted to post a summary of their chapter only in their institution's repository.
19. **Thesis/Dissertation**: If your license is for use in a thesis/dissertation your thesis may be submitted to your institution in either print or electronic form. Should your thesis be published commercially, please reapply for permission. These requirements include permission for the Library and Archives of Canada to supply single copies, on demand, of the complete thesis and include permission for Proquest/UMI to supply single copies, on demand, of the complete thesis. Should your thesis be published commercially, please reapply for permission. Theses and dissertations which contain embedded PJAs as part of the formal submission can be posted publicly by the awarding institution with DOI links back to the formal publications on ScienceDirect.

Elsevier Open Access Terms and Conditions
You can publish open access with Elsevier in hundreds of open access journals or in nearly 2000 established subscription journals that support open access publishing. Permitted third party re-use of these open access articles is defined by the author's choice of Creative Commons user license. See our open access license policy for more information.
Terms & Conditions applicable to all Open Access articles published with Elsevier:
Any reuse of the article must not represent the author as endorsing the adaptation of the article nor should the article be modified in such a way as to damage the author's honour or reputation. If any changes have been made, such changes must be clearly indicated.
The author(s) must be appropriately credited and we ask that you include the end user license and a DOI link to the formal publication on ScienceDirect.
If any part of the material to be used (for example, figures) has appeared in our publication with credit or acknowledgement to another source it is the responsibility of the user to ensure their reuse complies with the terms and conditions determined by the rights holder.
Additional Terms & Conditions applicable to each Creative Commons user license:
CC BY: The CC-BY license allows users to copy, to create extracts, abstracts and new works from the Article, to alter and revise the Article and to make commercial use of the Article (including reuse and/or resale of the Article by commercial entities), provided the user gives appropriate credit (with a link to the formal publication through the relevant DOI), provides a link to the license, indicates if changes were made and the licensor is not represented as endorsing the use made of the work. The full details of the license are available at http://creativecommons.org/licenses/by/4.0.
CC BY NC SA: The CC BY-NC-SA license allows users to copy, to create extracts, abstracts and new works from the Article, to alter and revise the Article, provided this is not done for commercial purposes, and that the user gives appropriate credit (with a link to the formal publication through the relevant DOI), provides a link to the license, indicates if changes were made and the licensor is not represented as endorsing the use made of the work. Further, any new works must be made available on the same conditions. The full details of the license are available at http://creativecommons.org/licenses/by-nc-sa/4.0.
CC BY NC ND: The CC BY-NC-ND license allows users to copy and distribute the Article, provided this is not done for commercial purposes and further does not permit distribution of the Article if it is changed or edited in any way, and provided the user gives appropriate credit (with a link to the formal publication through the relevant DOI), provides a link to the license, and that the licensor is not represented as endorsing the use made of the work. The full details of the license are available at http://creativecommons.org/licenses/by-nc-nd/4.0.
Any commercial reuse of Open Access articles published with a CC BY NC SA or CC BY NC ND license requires permission from Elsevier and will be subject to a fee.
Commercial reuse includes:

- Associating advertising with the full text of the Article
- Charging fees for document delivery or access

- Article aggregation
- Systematic distribution via e-mail lists or share buttons

Posting or linking by commercial companies for use by customers of those companies.

20. **Other Conditions**:

v1.9